Structures and properties of ThCr$_2$Si$_2$-type superconductors and related materials

Veronika Brigitte Zinth

aus

München, Deutschland

2012

Dissertation zur Erlangung des Doktorgrades

der Fakultät für Chemie und Pharmazie

der Ludwig-Maximilians-Universität München

Structures and properties of ThCr$_2$Si$_2$-type superconductors and related materials

Veronika Brigitte Zinth

aus

München, Deutschland

2012

Danksagung

Zuallererst möchte ich mich herzlich bei allen bedanken, die mich bei dieser Arbeit unterstützt haben. Ohne Ihre/ Eure Hilfe wäre diese Arbeit nicht möglich gewesen.

Mein besonderer Dank gilt:

- Prof. Dr. D. Johrendt für die Aufnahme in seinen Arbeitskreis, die Möglichkeit dieses Thema unter hervorragenden Bedingungen zu bearbeiten, seine Ermutigung, Unterstützung und Diskussionsbereitschaft bei allen auftretenden Problemen und für die Möglichkeit, eigene Ideen auszuprobieren.

- Prof. Dr. O. Oeckler für die Übernahme des Zweitgutachtens dieser Arbeit, seine Beratung bei Einkristall-Problemfällen und zahlreiche interessante Diskussionen (nicht nur) auf dem Gebiet der Strukturanalyse.

- PD Dr. H.-C. Böttcher, Prof. Dr. P. Gille, Prof. Dr. K. Karaghiosoff und Prof. Dr. W. Schnick für ihre Bereitschaft, als weitere Prüfer zur Verfügung zu stehen.

- Dr. V. Petříček und Dr. M. Dušek für ihre Hilfe bei inkommensurablen Kristallstrukturen.

- G. Oehlinger und Prof. a.D. J. Evers für die Messung von Hochtemperatur-Pulverdiffraktogrammen.

- D. Durach, F. Fahrnbauer und M. Tegel für ihre Mithilfe bei den Synchrotron-Einkristall-Messungen: Danke, das ihr euch mit mir die Nächte um die

Contents

1. Introduction

The development of instrumental analytical methods during the 20th century greatly influenced modern chemistry and sped up scientific progress. A detailed knowledge of composition and structure of compounds participating in a reaction enables an understanding of the processes involved and permits systematic planning of syntheses. A detailed understanding of the structure of a compound is also the key to understand its properties. Today, one of the most significant techniques in structure analyis is X-ray diffraction. This method is important for a wide range of scientific disciplines, e. g. chemistry, pharmaceutics, biology and biochemistry, mineralogy and geology, material sciences and physics. In solid state sciences, the accurate knowledge of structure obtained by X-ray diffraction helped to understand many phenomena like magnetism, electrical and thermal conductivity, phase transitions and thermal expansion, ferro-electricity and piezo-electricity.

One of the most interesting scientific problems, where a solution is required, is high temperature superconductivity. In 1986, Bednorz and Müller first reported "possible high-T_c superconductivity in the Ba-La-Cu-O system"[1]. The discovery of $YBa_2Cu_3O_7$ with a critical superconducting transition temperature (T_c) of 93 K[2] in 1987 broke all records and exeeded all expectations. Today, the compound with the highest confirmed critical temperature (133 K) is the copper oxide $HgBa_2CaCu_2O_{6+x}$[3] and first technical applications of the cuprate superconductors are on their way. However, while superconductivity in most low temperature superconductors is explained by the Bardeen-Cooper-Schrieffer (BCS) theory and therefore fairly well understood, the mechanism of supercon-

ductivity in the copper oxides remains unclear even after a quater of a century of intense research. Recently, the discovery of a new class of unconventional superconductors with T_c's up to 56 K – the iron based superconductors – opened new possibilities; investigation of these materials and comparison with the cuprates may help to gain an improved understanding of high temperature superconductivity. Here again, detailed X-ray analysis is necessary to provide the fundamental information required for an understanding of the structure and properties of these exceptional materials.

First reports on superconductivity in an iron pnictide oxide – the material LaFePO with $T_c = 5$ K – had already been published in 2006[4], but it was the discovery of LaFeAsO$_{1-x}$F$_x$ with a critical temperature of 26 K in February 2008[5], that caught worldwide attention. The non-superconducting parent compound LaFeAsO was reported to undergo a structural phase transition at 150 K, associated with antiferromagnetic ordering below 134 K and a peculiar anomaly in the electrical resistance[5–7].

Shortly after these findings, similar properties as in LaFeAsO were reported for BaFe$_2$As$_2$[8], followed by the discovery of superconductivity in Ba$_{1-x}$K$_x$Fe$_2$As$_2$ a few days later[9]. BaFe$_2$As$_2$ crystallizes in the well-known ThCr$_2$Si$_2$-type structure and consists of layers of edge sharing FeAs$_{4/4}$ tetrahedra alternating with barium atoms[10]. The compound undergoes a phase transition from tetragonal $I4/mmm$ to orthorhombic $Fmmm$ at $\sim$ 140 K, a translationengleiche transition with index 2. The distortion is rather small; at 20 K the orthorhombic lattice parameters differ by only 5 pm (0.9 %). The phase transition is connected with a spin density wave (SDW) causing an anomaly in the electrical resitivity of BaFe$_2$As$_2$ around 140 K[9]. Below the temperature
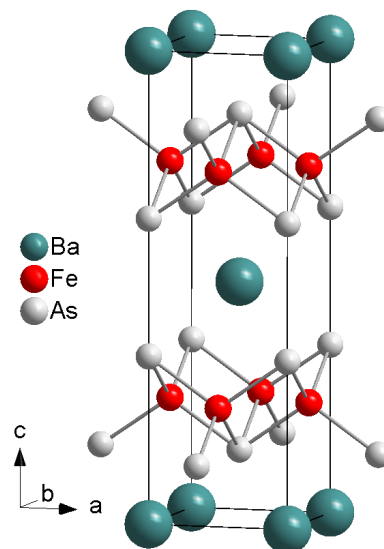
Fig. 1.1.: Crystal structure of BaFe$_2$As$_2$.

of the phase transition, stripe type antiferromagnetic order with the wave vector q = $(101)_O$ is reported[11]. The magnetic moments are oriented along the longer orthorhombic axis a and aligned antiferromagnetically along a and c and ferromagnetically along b.

Partial substitution of barium by potassium leads not only to considerable structural changes[12], but also introduces holes, as potassium carries one electron less than barium within its valence shell. In response to this hole doping, the SDW-transition in $Ba_{1-x}K_xFe_2As_2$ is shifted to lower temperatures and the orthorhombic distortion becomes weaker, until for $x \approx 0.3$ the phase transition and antiferromagnetism are suppressed. Additionally, superconductivity is found for x > 0.1, and a maximum T_c of 38 K is achieved for $x = 0.4$, as the phase diagram in Figure 1.2 illustrates. The maximum T_c of 38 K coincidences with an As-Fe-As angle close to the ideal tetrahedral value[12].

After the discovery of superconductivity in doped $BaFe_2As_2$, the so-called 122-phases with the parent compounds $BaFe_2As_2$, $SrFe_2As_2$[10] and $CaFe_2As_2$ (the latter discovered only in 2008[13,14]) quickly shifted to the focus of researchers worldwide. Every kind of substitution in the parent compounds that seemed possible was checked for its ability to induce superconductivity. While superconductivity induced by hole doping was likewise found in $Ba_{1-x}Rb_xFe_2As_2$[15,16] and $Ba_{1-x}Na_xFe_2As_2$[17], hole doping within the $FeAs_{4/4}$ tetrahedra layer by exchanging iron by manganese or chromium did not yield superconductivity[18,19]. Instead, surprisingly the substition of a few percent of iron by cobalt, introducing additional electrons into the $FeAs_{4/4}$-layer, was found to cause superconductivity with a maximum T_c of 22 K[20]. Figure 1.3 shows the phase diagram of electron-doped $Ba(Fe_{1-y}Co_y)_2As_2$. Contrary to $Ba_{1-x}K_xFe_2As_2$, the superconducting dome of $Ba(Fe_{1-y}Co_y)_2As_2$ spans only a Co doping range of approx. 10 %. With increasing Co content, the temperatures of the structural transition T_s and the temperature of the magnetic phase transition T_N separate, with T_s (dashed line in Figure 1.3) preceding T_N (solid line)[21]. Preparation of $Ba(Fe_{1-y}Co_y)_2As_2$

single crystals in a FeAs/CoAs flux soon gave good results, one reason the 122-compounds became quickly the most intensivly studied class of iron arsenide superconductors. Superconductivity in $Ba(Fe_{1-y}TM_y)_2As_2$ is also stabilized by substitution of Fe with any element of the Co and Ni colums (TM = Co, Rh, Ir, Ni, Pd, Pt)[21–24] and for these doping series the superconducting dome scales rather well (on the overdoped side) with the number of electrons added by the charge doping[25].

Another possibility of suppressing the SDW-type transition and inducing superconductivity turned out to be isoelectronic doping in $BaFe_2(As_{1-x}P_x)_2$[26] or $Ba(Fe_{1-y}Ru_y)_2As_2$[27]. The isoelectronic substitution of As by P gives rise to superconductivity for $x > 0.2$ with a maximum $T_c = 30$ K reached for $x = 0.32$[26]. Because of the smaller ionic radius of phosphorus compared to arsenic, the substitution leads to a shrinking of the unit cell and is often referred to as "chemical pressure". At first, the occurrence of superconductivity was attributed to the shrinking unit cell volume, since $BaFe_2As_2$ also shows superconductivity under physical pressure. However it seems that tiny structural details play an important role in this case: Detailed single crystal studies of $BaFe_2(As_{1-x}P_x)_2$ showed that although As and P are statistically distributed, different z coordinates are found for both atoms due to larger Fe-As than Fe-P bond lengths[28]. The detailed structural data reveals a reduction of the Fe-As bonds by 1.4 % for $x < 0.25$, followed by convergence to a value of ~ 236 pm. Phosphorus doping also seems to increase the width of the d-bands. Both parameters – reduction of the Fe-As bond length and increasing band width – are coupled with the magnetic moment and the suppression of the SDW state[28]. This shows how closely structural details can be correlated to the magnetic and superconducting properties.

The phase diagrams of $Ba_{1-x}K_xFe_2As_2$, $Ba(Fe_{1-y}Co_y)_2As_2$ and $BaFe_2(As_{1-x}P_x)_2$ presented above have a few features in common; irrespective of hole, electron or isoelectronic doping. The doping increasingly suppresses the spin density wave anomaly, which seems to be an important precondition for the occurrence of
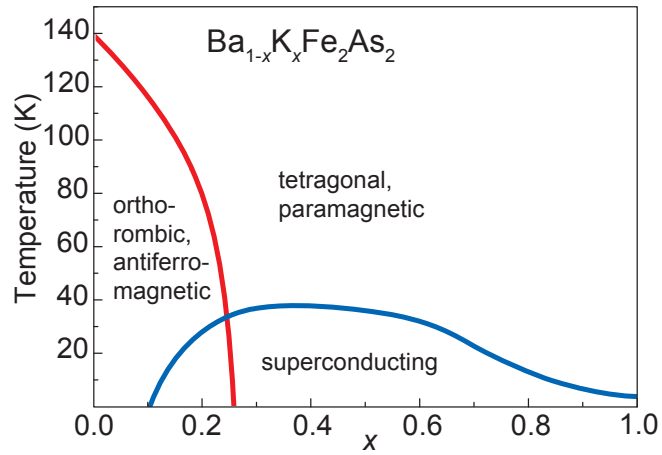
Fig. 1.2.: Phase diagram of $Ba_{1-x}K_xFe_2As_2$, Data from [12].
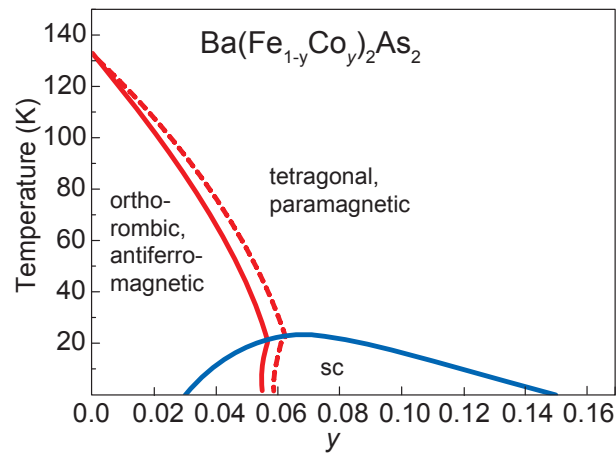
Fig. 1.3.: Phase diagram of $Ba(Fe_{1-y}Co_y)_2As_2$, Data from [25] and [29].
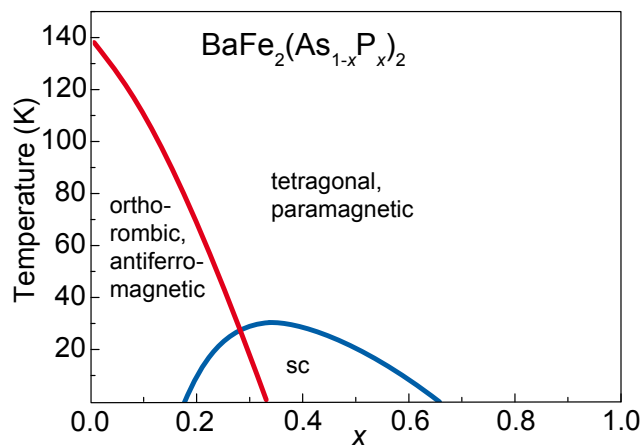
Fig. 1.4.: Phase diagram of $BaFe_2(As_{1-x}P_x)_2$, Data from [26].
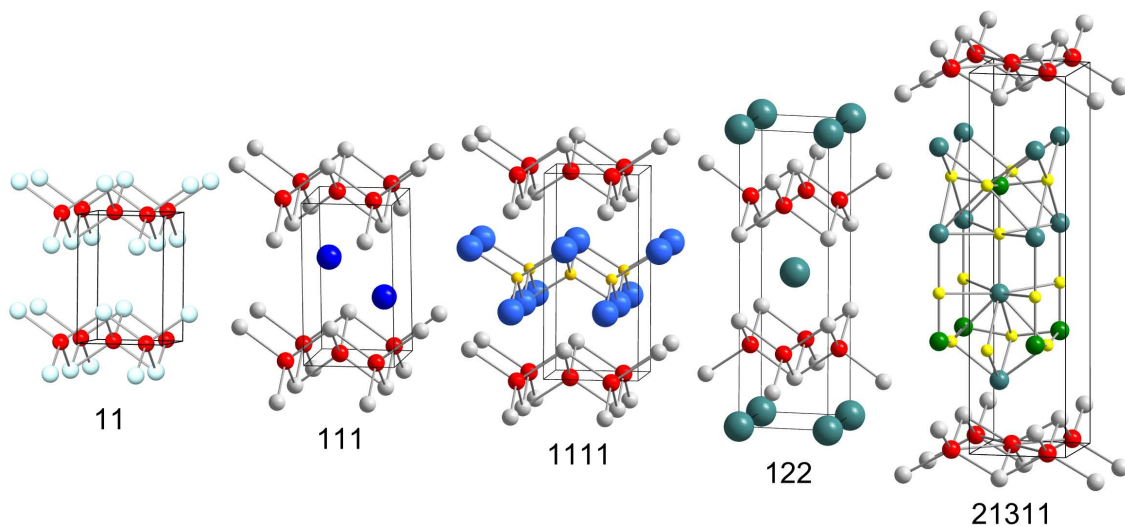
Fig. 1.5.: Structures of iron arsenide and chalcogenide superconductors: 11, 111, 1111, 122 and 21311 classes

superconductivity[28]. Superconductivity sets in while SDW anomaly and antiferromagnetism are still observed, but the highest T_c's are found beyond the point where the phase transition is completely suppressed. The underdoped part of the phase diagrams, where both superconductivity and antiferromagnetism are observed, has long been the subject of controversies whether the antiferromagnetic and the superconducting phase are separated or microscopically coexisting. The first convincing evidence, that indeed both phases coexist, was presented for $Ba(Fe_{1-y}Co_y)_2As_2$, where the orthorhombic distortion[29] and the intensity of the (1/2, 1/2, 1) magnetic reflection[30] observed with neutron scattering decrease again below T_c. This shows that the onset of superconductivity directly influences both structure and magnetism and speaks strongly in favor of a coexistance. Further studies support these results and recent works show similar effects for $Ba(Fe_{1-y}Rh_y)_2As_2$[31] and $Ba_{1-x}K_xFe_2As_2$[32].

Within the last four years, superconductivity was discovered in several more classes of compounds containing tetrahedral iron pnictide or chalcogenide layers – some of which had been known for a long time, others synthesized for the first time. Today, in addition to the already mentioned 1111- (the rare earth iron
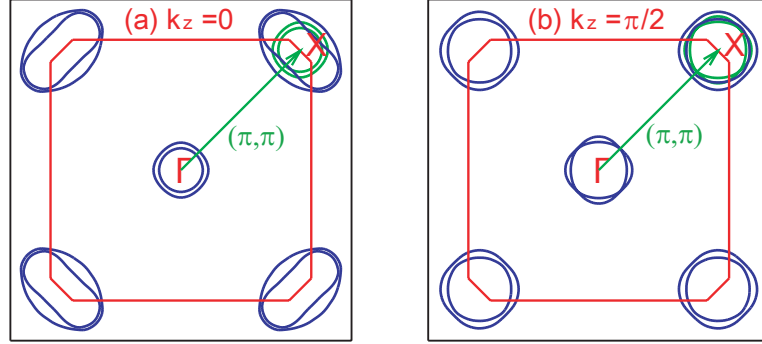
Fig. 1.6.: 2D section of the Fermi surface of BaFe$_2$As$_2$ with nesting vector[47]

arsenide oxides) and 122-classes of iron arsenides, superconductivity is known to exist in the so-called 111-phases (for example Na$_{1-x}$FeAs[33,34] and LiFeAs[35–37], T$_{c,max}$ ∼ 25 K), the 11-phases (for example FeSe[38] and Fe$_{1+y}$(Te$_{1-x}$Se$_x$)[39], T$_{c,max}$ ∼ 15 K), the 21311-phases (for example Sr$_2$VO$_3$FeAs, T$_c$ ∼ 37 K[40]) and the 23522-phases (for example Ca$_3$Al$_2$O$_{5-y}$Fe$_2$As$_2$ with $T_c = 30.2$ K[41]). The most recent discoveries are the selenides A$_x$Fe$_{2-y}$Se$_2$ (A = K, Rb, Cs, Tl), with a deficiency of both potassium and iron and superconducting transition temperatures up to 32 K[42,43] and the iron platinum arsenides (CaFe$_{1-x}$Pt$_x$)$_{10}$Pt$_z$As$_8$[44–46] with transition temperatures up to 38 K. Examples for several classes of iron based superconductors are shown in Figure 1.5. As can be seen in the figure, all iron based superconductors contain FeAs$_{4/4}$ or FeSe$_{4/4}$ tetrahedra layers be separated by alkaline or alkaline earth atoms, layers of rare earth oxide, platinum arsenide (not shown in the figure) or by perovskite-type layers.

Since all iron based superconductors share FeAs$_{4/4}$ (or FeSe$_{4/4}$) tetrahedra layers as building blocks, these layers must play a crucial role for superconductivity. Indeed, the Fe $3d$ states near E$_F$ dominate the electronic properties of the material. The electronic structure of the iron based superconductors is that of a semi-metal[48] and shows quasi-two-dimensional qualities[49]. Figure 1.6 displays a 2D section of the Fermi surface of BaFe$_2$As$_2$[47], which consists of a hole like

cylinder around Γ and electron-like cylinders around X, formed by several bands crossing the Fermi energy from above (∪ shaped, in the case of the electron-like cylinders) or below (∩-shaped, in the case of the hole-like cylinders). The hole Fermi surface cylinders are transformed onto the electron surface cylinders by a commensurate nesting vector (π, π). If this Fermi-surface nesting is good, charge density wave (CDW) and spin density wave (SDW) instabilities may develop[50]. As described above, $BaFe_2As_2$ undergoes a structural and magnetic phase transition to an antiferromagnetically ordered phase at low temperatures. The antiferromagnetic wave vector q $= (\pi, \pi)$ is the same as the nesting vector shown in Figure 1.6[51]. Doping tunes the Fermi surface and shifts the system away from the good nesting, until finally the phase transition is suppressed. However, the instability of the electronic structure is also believed to make the system susceptible to superconducting pairing[51]. Experiments[52,53] as well as theoretical investigations[54,55] suggest that strong interband scattering between nearly nested Fermi surface sheets plays an important role in superconductivity.

Because the iron d-states dominate the electronic structure close to the Fermi level and strong Fe-As (and also Fe-Fe) bonds exists, the geometry of the $FeAs_{4/4}$ tetrahedra layers is strongly coupled to the electronic and magnetic properties of the iron pnictide superconductors. Thus it is not astonishing that the relationship between structural parameters and properties is and has been a much discussed issue. As already mentioned, the highest T_c in $Ba_{1-x}K_xFe_2As_2$ is observed at $x = 0.4$, where the As-Fe-As angle ε is close to the ideal tetrahedral angle of $109.47°$. As shown in Figure 1.7 (top), the $FeAs_{4/4}$-layer of the 122-compounds contains two different As-Fe-As angles, ε (twofold) and ε' (fourfold). The twofold As-Fe-As angle ε can be calculated from a, c and z using $\varepsilon = 2\arctan(\frac{a/2}{(z-0.25)\cdot c})$ and the fourfold angle ε' is dependent on ε through the relation $\cos(\varepsilon') = \frac{1}{2}(1 + \cos(\varepsilon))$. Early on, a correlation between the angle As-Fe-As angle ε and the superconducting transition temperature in the iron pnictide superconductors was collected by Lee et. al.[59]. A plot of T_c versus ε for various 1111-compounds showed the high-
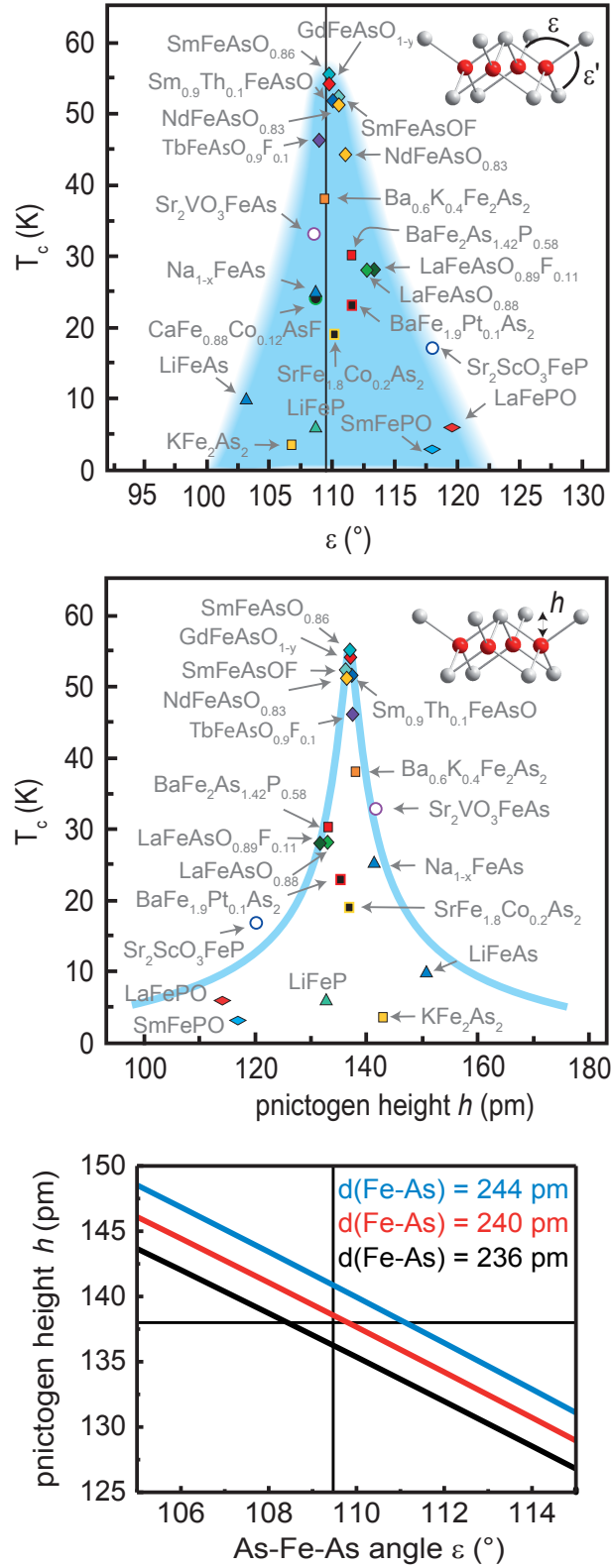
Fig. 1.7.: top: T_c versus As-Fe-As angle ε for various iron pnictide superconductors, Data from [56] p121 - 126 and [24,57,58]. Middle: pnictogen height h versus T_c, data from [56] and [24,57,58]. Bottom: Correlation between ε and h for d(FeAs) = 236 - 244 pm.

est T_c's appear for a $FeAs_4$ coordination close to a regular tetrahedron. Figure 1.7 (top) shows such a plot for a number of 1111-compounds and other iron pnictide superconductors (the highest T_c's for the different doping series are shown). However, although there seems to be a trend towards ideal tetrahedral geometry in the high T_c compounds, not all compounds with ε close to 109.47° also have high T_c's. This shows that while ε might have some relevance, it is not the predominant parameter controlling T_c.

Another parameter discussed for its correlation to T_c is the distance h between Fe- and the adjacent pnictogen layer[60]. The highest T_c's of selected superconductors with a Fe valence of 2+ and undisturbed Fe-layers were found to give a symmetric curve with a peak around 138 pm (a plot of h versus T_c is shown in Figure 1.7 (middle)). Superconductors with partial substitution of the Fe position deviate, possibly because the disorder within the $FeAs_{4/4}$ layer is unfavorable for higher T_c's. Theoretical calculations suggested that the anion height h might be a "possible switch" between high T_c nodeless $s^{\pm}$ and low T_c nodal pairing for the 1111-compounds[61]. For the 122-compounds, the pnictogen height is given by $h = (z - 0.25) \cdot c$ and related to the As-Fe-As angle ε by $h = d(\text{Fe-As}) \cdot \cos(\frac{\varepsilon}{2})$. Thus it depends both on the Fe-As bond length and the angular geometry of the $FeAs_4$ tetrahedra. The correlation between h and ε is shown in Figure 1.7 (bottom) for 244 pm (blue) $\geq$ d(FeAs) $\geq$ 236 pm (black). For a Fe-As distance of 240 pm (red), the ideal tetrahedral angle of 109.47° (vertical line) almost corresponds to the "ideal" pnictogen height of 138 pm (horizontal line).

A flaw for all these considerations is the fact that basic structural information is still lacking for many iron based superconductors, let alone the high quality data neccesary for an exact determination of the As-Fe-As angle or the Fe-As bond length. Also, most structural data was determined at room temperature and not at temperatures close to T_c. To remedy this problem, not only the synthesis of new superconducting compounds and known superconductors and a characterization of their physical properties is neccesary in the course of further

research on iron arsenide superconductors, but also the gathering of detailed structural information on all these compounds – a task for crystallographers and solid state chemists.

Work on this thesis started in 2008, only a few months after the discovery of superconductivity in doped $BaFe_2As_2$. The first goal at that time was the investigation of further compounds crystallizing in the $ThCr_2Si_2$-type structure with respect to phase transitions, magnetic properties and possible superconductivity. One candidate that seemed to be very similar to $BaFe_2As_2$ because of its structural phase transitions, was $SrRh_2As_2$. However, a closer look revealed a more complicated and challenging structural chemistry. The first two chapters of this work are devoted to the study and solution of the intriguing crystallographic problems of the three $SrRh_2As_2$ phases and the characterization of further ternary rhodium arsenides. Furthermore, high quality single crystals of $Ba_{1-x}K_xFe_2As_2$ were synthesized and single crystals as well as powder samples of $Ba_{1-x}K_xFe_2As_2$ were investigated with synchrotron X-ray diffraction methods as described in chapters 5 and 6. Finally, the last part of this thesis concentrates on the question which effects of doping are actually responsible for the occurrence of superconductivity in $BaFe_2As_2$. Is the superconductivity induced by the alteration of charge in the $FeAs_{4/4}$-layer, by the disorder introduced by doping, or by the structural changes? To help elucidate this issue, several substitution series of 122-iron arsenides were prepared and the influence of hole and electron or charge and isoelectronic doping on superconductivity, magnetic and structural properties and their mutual relationship was studied (chapters 7,8,9 and 10).

2. Synthesis

2.1. Starting materials and general techniques

A list of the starting materials used in this work is given in table 2.1.

  All reactions were carried out in sealed silica ampoules under an atmosphere of purified argon. Prior to sealing, the silica ampoules were connected to a vacuum line, evacuated using a rotary vane pump and put under dry argon. The drying and purification of argon was archieved by passing the gas through columns filled with BTS-catalyst (copper dispersed on a ceramic carrier matrix, Fluka) kept at a temperature of 393 K, molecular sieve (porewidth 0.4 nm, Merck) and phosphorus pentoxide (Merck).

The synthesis was carried out in tubular furnances with electrical resistance heating and Pt/PtRh thermocouples to measure the temperature, connected to programmable controllers (Eurotherm). Checked with an external thermometer, the actual temperatures were found to vary by ~ 60 K for different furnances. The temperature in the furnances used for this thesis was mostly 40 K higher than measured by the build-in thermocouples at the typical temperatures used for synthesis. This has been taken into account for the temperature programs described in this thesis.

Table 2.1.: List of starting materials used in this work

name	formula	supplier	purity	appearence
potassium	K	Sigma-Aldrich	99,95 %	ingot
calcium	Ca	Sigma-Aldrich	99,99 %	dendritic pieces
strontium	Sr	Alfa Aesar	99,95 %	dendritic pieces
barium	Ba	Sigma-Aldrich	99,99 %	dendritic pieces
iron	Fe	Chempur	99.9 %	powder
cobalt	Co	Sigma-Aldrich	99,9 %	powder
rhodium	Rh	*	99,95 %	powder
phosphorus (red)	P	Chempur	99,999 %	powder
arsenic	As	Alfa Aesar	99,999 %	pieces
bismuth	Bi	Fluka	99.99 %	granules
lead	Pb	Chempur	99,999 %	granules

*Allgemeine Gold- und Silberscheideanstalt AG

2.2. Preparation of (binary) transition metal arsenides

The transition metal arsenides used as starting materials (like FeAs, RhAs, $Fe_{1-y}Co_yAs$ and $Fe_{1-y}Co_yAs_{1-x}P_x$) were prepared as following: Stoichiometric amounts of the elements were sealed in pre-dried silica ampoules under an atmosphere of purified argon using an oxyhydrogen burner. During preparation, all elements were handled in air, but arsenic was stored under an atmosphere of purified argon. For sample sizes of 0.5 g silica ampoules with $\varnothing = 11$ - 12 mm were utilized, while 14 - 15 mm were used for 1 g samples. Reaction temperatures up to 1173 K were used, since at higher temperatures a reaction with the ampoule material takes place. If several reaction steps (as in the case of $Fe_{1-y}Co_yAs$) were necessary, the ampoules were opened and all pieces of silica removed before homogenizing the sample. The reaction products were checked regularly for ferromagnetic impurities with the help of a magnet. All transition metal arsenides

named above are stable in air.

2.3. Preparation of polycrystalline samples of ThCr$_2$Si$_2$-type compounds

Even though most ternary ThCr$_2$Si$_2$-type phases are stable in air, frequently air sensitive intermediate products (possibly alkaline or earth alkaline arsenides) can be observed, quickly oxidizing upon air contact with a change of colour to brown or red. For this reason, all compounds containing alkaline or earth alkaline elements were handled only in an argon filled glovebox (MB150-Gl, O$_2$ < 1 ppm, H$_2$O < 1 ppm, MBraun) until the synthesis was complete.

For the preparation of ThCr$_2$Si$_2$-type phases stoichiometric mixtures of the elements (or mixtures of alkaline or earth alkaline metal and transition metal arsenide) were weighed into alumina crucibles, which were placed in pre-dried silica ampoules ($\varnothing$ = 14 - 15 mm) that were sealed under an atmosphere of purified argon. The handling of potassium was facilated by the use of alumina inlays that also help to reduce the loss of potassium by evaporation during the reaction. Usually, a first reaction step at lower temperatures (923 K - 1023 K) followed by homogenization of the sample was carried out to prevent the sticking of the sample to the crucible. The first reaction step typically yields a mixture of binary arsenides that react to the ternary compounds upon annealing at 973 - 1273 K. In most cases, complete homogenization of the sample is necessary to get clean reaction products, sometimes even to get the ternary phase as product at all. Detailed temperature programs for all compounds are given in the respective chapters.

The ThCr$_2$Si$_2$-type phases synthesized in this thesis have a metallic appearance and are stable in air (with the exception of Sr$_{1-x}$Ba$_x$Rh$_2$As$_2$ and the potassium iron arsenides which are unstable in air).

2.4. Preparation of single crystals

A number of single crystals were selected directly from polycrystalline samples. If the quality of these crystals was not sufficent, flux methods were applied for the synthesis of high quality crystals.

Synthesis in a Pb/Bi flux was performed using alumina crucibles sealed in silica ampoules. Depending on the composition, this flux is still liquid at temperatures as low as ~ 400 K, because the Pb/Bi phase diagram has an eutectic point for 45 wt % Pb at 398.5 K. After the reaction, the crucibles were smashed and the reaction mixture put into concentrated acetic acid with a few ml of H_2O_2 (30 %) added to dissolve the flux. This typically took several days. From time to time, H_2O_2 was added. The suspension was filtered and the crystals washed first with acetic acid, then with water. In most cases, mixtures of binary and ternary arsenides were obtained, from which the desired crystals were selected.

Synthesis of $Ba_{1-x}K_xFe_2As_2$ single crystals gave best results in a FeAs self-flux. Because of the high melting point of FeAs, synthesis has to be carried out above 1323 K. To prevent the evaporation of potassium at these temperatures, which would result in the destruction of the silica ampoules, the reaction mixture was put directly into Nb tubes which were welded under an atmosphere of purified argon. The closed Nb tubes were again sealed in silica ampoules. The reaction products were removed from the Nb tubes, if necessary carefully crushed and single crystals were selected.

3. Structural Phase Transitions in SrRh$_2$As$_2$

3.1. Introduction

The coupling of electronic and lattice degrees of freedom creates some of the most intriguing phenomena in solid state materials. Two well known manifestations of electron-lattice coupling are charge-/spin-density-waves (CDW, SDW)[50] and conventional superconductivity[62]. In superconductors, the coupling is usually weak, but it determines the critical temperature T_c. Stronger coupling increases T_c to a certain limit, while too strong interactions can drive the system to a CDW state, where a structural distortion reduces the electronic energy.

Structural phase transitions associated to CDW instabilities have been observed in many metallic materials with quasi low-dimensional crystal structures, among them transition-metal chalcogenides[63,64] and oxides[65]. CDW ordering has often been considered as a manifestaion of the Peierls-instability, thus relying on nesting, which means that a piece of the Fermi surface can be translated by a vector **q** and superimposed on another piece of the surface. Meanwhile, reasonable doubts arise whether nesting is the only driving force of the CDW, and in

fact, **q**-vectors extracted from Fermi surface nesting are in some cases inconsistent with experimental wave vectors[66] even in the archetypical CDW compound $TaSe_2$[67].

Layered crystal structures also constitute the basis of the high-temperature superconductors, both the copper oxides[1] and the iron arsenides[5,9]. As described in chapter 1, the latter are build up by layers of edge-sharing $FeAs_4$-tetrahedra, separated for example by oxide layers as in LaOFeAs with ZrCuSiAs-type structure[68] or by alkaline earth metals as in $BaFe_2As_2$ with $ThCr_2Si_2$-type structure[10]. These non-superconducting parent compounds exhibit SDW-type phase transitions, accompanied by a reduction of the space group symmetry from tetragonal to orthorhombic[8,69]. In these materials, the SDW wave vectors perfectly coincide with the Fermi surface nesting, which is also believed to play a certain role in the pairing mechanism[70].

The orthorhombic low-temperature structure of $BaFe_2As_2$ was first classified[12] as isotypic to the β-$SrRh_2As_2$-type in the space group *Fmmm*[71]. Indeed also the rhodium compound transforms to the tetragonal $ThCr_2Si_2$-type (γ-$SrRh_2As_2$, space group *I4/mmm*), but at much higher temperature (555 K) in comparison with $BaFe_2As_2$ (140 K)[8] and $SrFe_2As_2$ (210 K)[72]. Furthermore, the orthorhombic lattice distortion, measured as $\delta = |a-b|/(a+b)$, is about one order of magnitude larger in $SrRh_2As_2$ ($\delta \approx 10^{-2}$) than in $BaFe_2As_2$ ($\delta \approx 10^{-3}$) Despite the striking symmetry congruence of the *I4/mmm* $\leftrightarrow$ *Fmmm* structural transitions in $SrRh_2As_2$ and $BaFe_2As_2$, both are not expexted to have the same origin. Since $SrRh_2As_2$ carries no magnetic moment, the driving force is not magneto-elastic coupling by antiferromagnetic SDW ordering as in $BaFe_2As_2$. Thus, the $\beta \rightarrow \gamma$ transition of $SrRh_2As_2$ may be assigned to a possible CDW instability of the $RhAs_{4/4}$ layers. Recently published band structure calculations[73] revealed no hint to an instability, however, the electronic susceptibilty has not yet been analyzed in detail. Furthermore, β-$SrRh_2As_2$ transforms to a third modification (α-$SrRh_2As_2$), which is stable below 463 K. The structure of α-$SrRh_2As_2$ was

assumed to be closely related to the orthorhombic BaNi$_2$Si$_2$-type (space group *Cmcm*), but could not be successfully refined. Thus the structures of the α- and the β-phases in the following sequence of polymorphs are unclear so far.

$$\alpha\text{-SrRh}_2\text{As}_2 \xrightarrow{463\text{K}} \beta\text{-SrRh}_2\text{As}_2 \xrightarrow{555\text{K}} \gamma\text{-SrRh}_2\text{As}_2$$

In order to shed light on several open issues regarding the crystal structures and phase transitions of polymorphic SrRh$_2$As$_2$ and its relationships to those occurring in the isostructural iron arsenides, SrRh$_2$As$_2$ has been synthesized and detailed single crystal X-ray experiments were conducted.

3.2. Experimental Details

Powder samples of α-SrRh$_2$As$_2$ were synthesized by heating stoichiometric mixtures of the elements in alumina crucibles that were sealed in silica tubes under an atmosphere of purified argon. The mixtures were heated to 893 K, kept at this temperature for 10 h and cooled down to room temperature. The reaction products were homogenized and annealed at 1273 K for 30 hours several times. For the synthesis of β-SrRh$_2$As$_2$, the sample was quenched after the last annealing step. X-ray powder patterns have been measured on a STOE Stadi-P diffractometer (Cu-K$\alpha_1$radiation). The TOPAS package[74] was used for Rietveld refinements.

Single crystals of α-SrRh$_2$As$_2$ were grown in a Pb/Bi-flux (55 wt % Bi, ten times surplus of flux) by heating to 1373 K, holding the temperature for 30 h, cooling to 433 K with 2 K/h and then quenching the sample. Single crystals of β-SrRh$_2$As$_2$ were obtained in a similar way using 45 wt % Bi and a cooling rate of 30 K/h. The flux was dissolved in HAc/H$_2$O$_2$, and revealed platelike crystals with a tendency to cleave. EDX measurements (on the crystal of α-SrRh$_2$As$_2$ used for structure determination and the crystal of β-SrRh$_2$As$_2$ used for high temperature diffraction) confirm the composition and show no Pb or Bi was incorporated into the structure. The crystals were checked by Laue photographs using white molybdenum radiation. Single crystal intensity data of α-

(a)   **(b)**
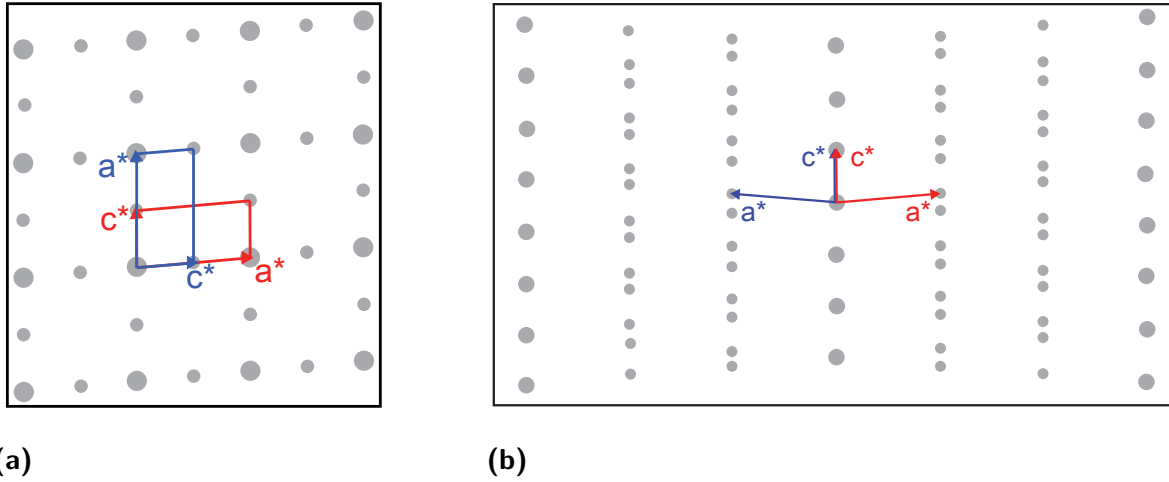
Fig. 3.1.: Schematical picture of the reciprocal space of α-SrRh$_2$As$_2$ (a) and Sr$_{1-x}$Ba$_x$Rh$_2$As$_2$ (b) with the unit cells of the two twin domains.

and γ-SrRh$_2$As$_2$ was recorded on a STOE IPDS imaging plate detector (Ag-K$_\alpha$, graphite monochromator, ψ-scan) equipped with a Heatstream (Stoe & Cie Gmbh, Darmstadt, Germany) device for high temperature measurements. Single crystal intensity data of β-SrRh$_2$As$_2$ was collected on a Gemini four-circle diffractometer equipped with an Atlas CCD detector. For structure solution and refinement the SHELX suite of programs[75,76] (α-SrRh$_2$As$_2$ and γ-SrRh$_2$As$_2$) and the program Jana2006[77] (β-SrRh$_2$As$_2$) were used. The electronic structure and Crystal Orbital Hamilton Function (COHP) of α-SrRh$_2$As$_2$ and γ-SrRh$_2$As$_2$ were calculated from self-consistent TB-LMTO-ASA potentials and wave functions[78] using density-functional (DFT) methods.

3.3. α-SrRh$_2$As$_2$

Diffraction patterns of the room temperature phase pretended orthorhombic *mmm* symmetry as reported in Ref.17, but all attempts at finding a satisfactory structure model failed. A careful inspection of the pattern revealed multiple twinning, but only two main domains contribute considerably as shown in Fig-
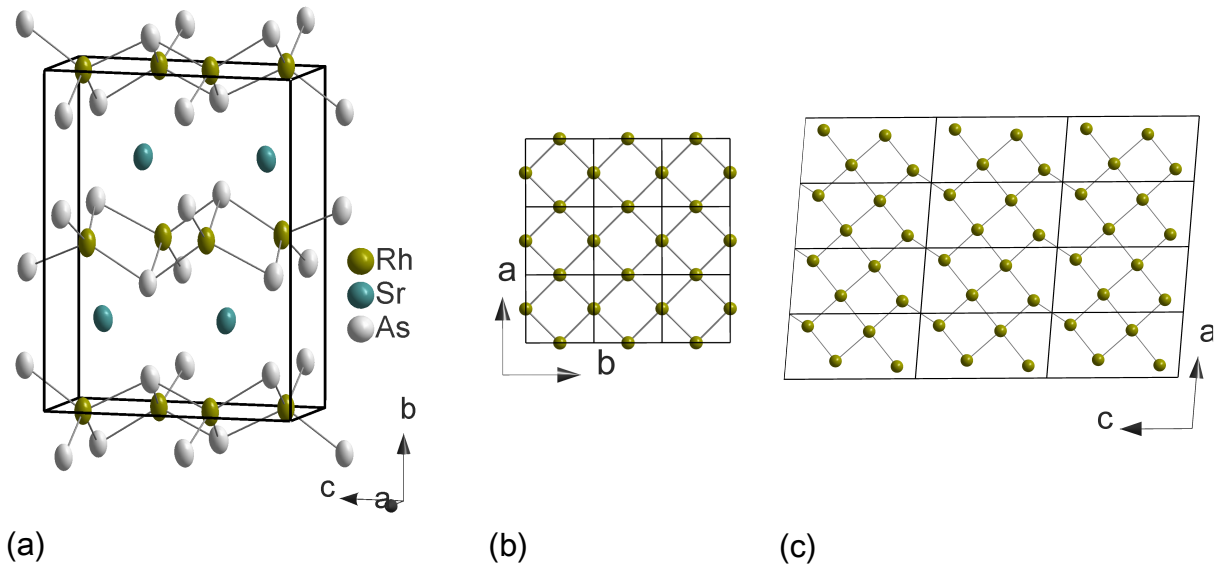
Fig. 3.2.: (a) Unit cell of α-SrRh$_2$As$_2$, the anisotropic displacement parameters (95 % probability) are shown. (b) Comparison of the rhodium networks in γ- and α-SrRh$_2$As$_2$ (c).

ure 3.1(a). Their unit cell dimensions are $a = 421.2(1)$ pm, $b = 1105.6(2)$ pm, $c = 843.0(1)$ pm and $\beta = 95\,°$, respectively. The latter is supported by observations in single crystals of α-SrRh$_2$As$_2$ with about 10 % of Sr substituted by Ba, where an easier kind of twinning occurs and the unit cell dimensions can easily be identified (Figure 3.1(b)). The domains shown in Figure 3.1(a) transform onto each other by a twofold rotation around [1 0 2] that feigns the two times larger pseudo unit cell $a \approx 842$ pm, $b \approx 1106$ pm, $c \approx 842$ pm and $\beta = 95\,°$ or a four times larger pseudo-orthorhombic unit cell with $A = $ -2a-$c = 1138$ pm, $B = $-$b = $ 1105.6 pm, $C = $ -2a+$c = 1243.2$ pm, $\alpha = 90°$, $\beta = 90.04°$, $\gamma = 90°$. Integration of the intensity data was performed using this doubled monoclinic pseudo unit cell. An absorption correction was performed using the shape of the crystal as obtained by the diffractometer's video system. Then the reflections were transformed according to the two domains, stored into a .hklf5 file and merged with the program mergehklf5[79]. The structure was solved and refined in the space group $P2_1/c$ with R$_1 = 0.0928$ (Table 3.1).

Table 3.1.: Crystallographic data of α-SrRh$_2$As$_2$

Empirical formula	SrRh$_2$As$_2$
Crystal system, space group	Monoclinic, $P2_1/c$, No. 14
a, b, c (pm)	421.2(1), 1105.6(2), 843.0(1)
$\beta°$	95.06(2)
Cell volume (nm^3)	0.3920(1)
Molar mass (g/mol)	443.3
Calculated density (g/cm^3), Z	7.53, 4
Radiation type, λ (Å)	Ag-Kα, 0.56087
2θ range	3.65 - 29.95
Transmission (min, max)	0.1960, 0.5600
Absorption coefficent (mm^{-1})	20.46
Total number of reflections	12430
Independent reflections, R$_{int}$	3652, 0.2188
Reflections with $I > 2\sigma(I)$, R_σ	1582, 0.1545
Refined parameters, Goodness-of-fit on F^2	47, 0.86
R_1, $wR2$ ($I > 2\sigma(I)$)	0.0928, 0.2312
R_1, $wR2$ (all data)	0.1891, 0.3107
Largest residual peak, hole $e^-/$Å^3	5.654, -6.042
Twin fraction	51.7(3) %

Atomic parameters:

		x	y	z	U$_{eq}$
Sr	$4e$	0.2478(4)	0.7539(1)	0.1341(2)	0.0184(3)
Rh1	$4e$	0.2245(3)	0.5067(2)	0.3807(2)	0.0166(3)
Rh2	$4e$	0.3116(4)	0.0093(2)	0.3522 (2)	0.0179(3)
As1	$4e$	0.1868(4)	0.4072(2)	0.1126(2)	0.0185(3)
As2	$4e$	0.2749(4)	0.1229(2)	0.1108(2)	0.0171(3)

Table 3.2.: Interatomic distances and angles of α-SrRh$_2$As$_2$

Interatomic distances and angles					
Rh1 -	Distance	Rh2 -	Distance	Sr3 -	Distance
As4	240.8(2)	As4	238.8(2)	As4	317.0(2)
As4	246.4(2)	As5	239.1(2)	As4	319.4(2)
As4	247.0(2)	As5	242.4(2)	As5	319.5(2)
As5	251.1(2)	As5	248.3(2)	Rh2	327.8(2)
Rh2	286.4(3)	Rh2	284.7(3)	As4	330.1(2)
Rh1	288.4(2)	Rh1	286.4(3)	Rh2	337.1(2)
Rh2	289.0(2)	Rh1	288.8(2)	As5	338.8(2)
Rh1	294.3(3)			Rh1	340.1(2)
				Rh1	342.8(2)
As5 -				Rh1	344.4(2)
As5	313.0(1)				
As4	317.0(1)				
Angles					
As4-Rh1-As4	105.68(8)	As4-Rh2-As5	110.23(7)		
As4-Rh1-As4	107.53(7)	As4-Rh2-As5	110.89(8)		
As4-Rh1-As5	117.5(1)	As4-Rh2-As5	123.89(9)		
As4-Rh1-As4	117.2(1)	As5-Rh2-As5	122.0(1)		
As4-Rh1-As5	104.02(7)	As5-Rh2-As5	108.54(8)		
As4-Rh1-As5	105.46(8)	As5-Rh2-As5	79.24(8)		

Selected interatomic distances and bond angles of α-SrRh$_2$As$_2$ are compiled in Table 3.2. The shortest As-As distances between the RhAs$_4$-tetrahedron layers is 313.0 pm, thus no significant interlayer bonding is expected. The Rh-As distances range from 238.8 to 251.1 pm and the As-Rh-As angles in the RhAs$_4$-tetrahedra from 79.24 ° to 123.89 °. The strong distortions of the RhAs$_4$ - tetrahedron layers are visible in Figure 3.2 (a), which shows the unit cell of α-SrRh$_2$As$_2$. The distortion is best grasped by looking at the positions of the Rh atoms within the RhAs-layers (Figure 3.2 (c)). In contrast to the regular square network of
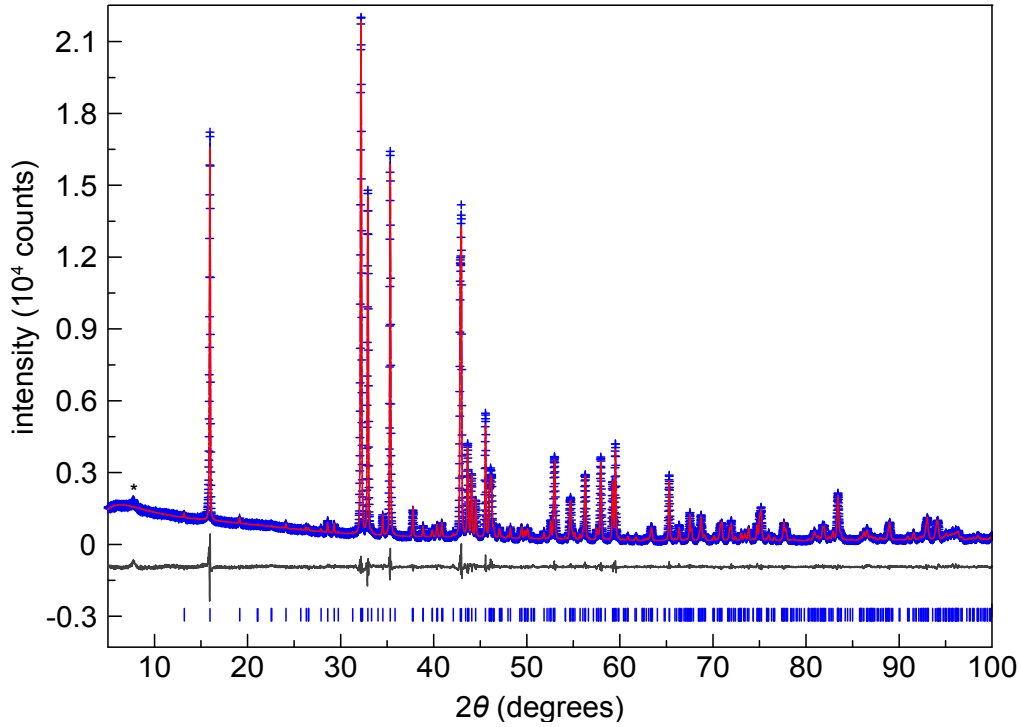
Fig. 3.3.: X-ray powder pattern (top, blue), Rietveld fit (top, red) and difference curve (bottom) of α-SrRh$_2$As$_2$ (blue tick marks)

Rh in the tetragonal high temperature phase with a constant distance of 290 pm between the Rh atoms (Figure 3.2 (b)), Rh-Rh distances in α-SrRh$_2$As$_2$ vary from 284.7 pm to 378.5 pm, and chains of four Rh atoms with short distances alternate with one longer distance between the chains.

A powder diffraction pattern of α-SrRh$_2$As$_2$ together with the Rietveld refinement is shown in Figure 3.3.

3.4. β-SrRh$_2$As$_2$

First measurements of β-SrRh$_2$As$_2$ single crystals revealed orthorhombic all face centered symmetry with unit cell parameters $a = 1114.4(3)$ pm, $b = 574.4(2)$ pm and $c = 611.5(2)$ pm in agreement with Ref.17. An initial refinement using the space group *Fmmm* converged to R$_1 = 0.055$, but the anisotropic displacement parameters were not acceptable and clearly hint at a lower symmetry. The in-

(a)   **(b)**
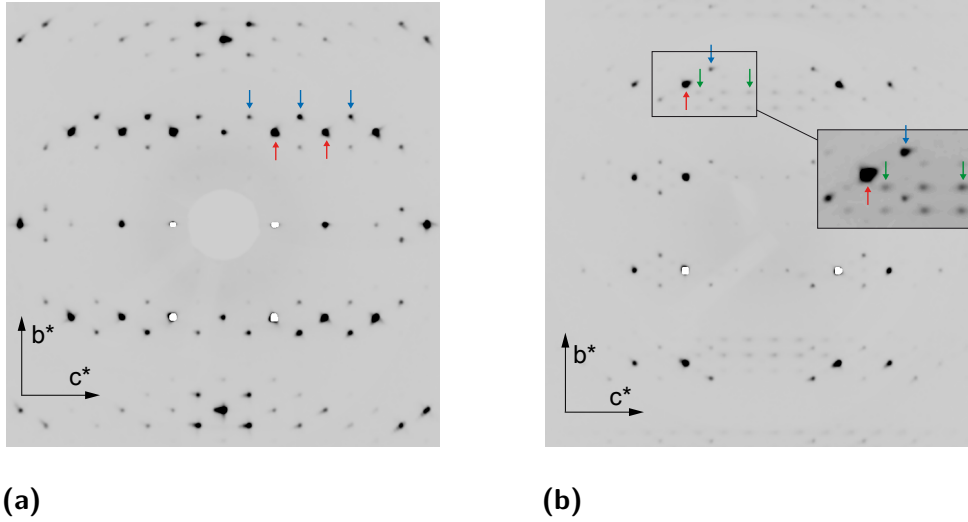
Fig. 3.4.: (a) h0l-layer of β-SrRh$_2$As$_2$ with main reflections (red arrows) and strong satellite spots (blue arrows) at **q** = (1, 0, 0.3311(4)), (b) h-1l-layer with main reflections (red arrows), strong satellites (blue arrows) and weak satellites (green arrows) corresponding to **q** = (0.5, 0, ≈1/6) (contrast in the enlarged part modified).

spection of the diffraction pattern revealed additional satellite spots surrounding each Bragg position of the orthorhombic cell as shown in Figure 4. These strong satellite reflections were indexed using the nearly commensurable modulation vector **q** = (1, 0, ≈1/3). Additional, very weak spots were detected at **q** = (0.5, 0, ≈1/6) and further, barely detectable reflections exist for some (h+1/2, k, l+1/2) (possibly 3rd order satellites) and (h, k+1/2, l+1/2). Using the (0.5, 0, ≈1/6) reflections as first order satellites, we have the rather unusual case that the second order satellites are much stronger than the first order ones. This clearly indicates that the second order components of the modulation functions are predominant. As a first approach, we have neglected the weak first order spots and tried to find a solution using **q** = (1, 0, 0.3311(4)) as the modulation vector, which is compatible with the (3+1)-dimensional superspace group $Fmmm(10\gamma)\sigma00$.

A comparison of the lattice parameters shows similarities between the above mentioned pseudo orthorhombic lattice A, B, C of α-SrRh$_2$As$_2$ and the cell parameters of β-SrRh$_2$As$_2$ ($a \approx$ A, $b \approx$B/2, $c \approx$ C/2). Thus it seems possible that the

α-phase is still partially present in the crystal of the β-phase. This would cause additional reflections with (h, k+1/2, l+1/2) and violations of the F-centering, both of which we observe. A multiphase refinement of the crystal gives a significantly better fit for the collected data and yields a volume fraction of 68 % β-phase and 16 % for each of the α-phase twin components. The refinement data are summarized in Tables 3.3, 3.4 and 3.5. The **q**-vector is close to commensurable, but the best refinement results were obtained with the incommensurate model. The overlap option for closest reflections implemented in Jana2006 was used. Both first and second order satellite reflections are reasonably well refined (see Table 3.3).

The strongest modulation concerns the position of the Rh-atom in c-direction (Figure 3.5 a). A crenel function was used to describe the modulation, combined with a positional modulation function expressed by Legendre polynomial. No modulation of the Rh atoms in a- and b-directions were observed. The strong modulation of the Rh atom influences the adjoining As atom, which shows a positional modulation in c-direction that can be described very well by a combination of one sinus and one cosinus term (Fig 3.5 b). For the As atom also a second positional modulation with smaller amplitude is observed in a-direction (Fig 3.5 c). The Sr atoms show pretty much the same modulation in a-direction (Figure 3.5 d). The modulation function of the ADP parameters was also refined, with the biggest changes found for the ADP parameters of the As atom (see Table 3.4). Figure 3.6 shows the modulated structure of β-SrRh$_2$As$_2$ (view along the b-axis, three unit cells in c-direction are shown). Both the slight modulations of As and Sr in c-direction and the modulations of the ADP parameters are visible. Figure 3.7 c) illustrates the modulation within the RhAs$_{4/4}$ tetrahedra planes (only the Rh atoms are shown). The modulation leads to a strong elongation of every seventh Rh-Rh distance to 358.0 pm along c, while the adjoining distances have a length of 313.2 pm and 295.8 pm and the shorter ones as well as all distances parallel to b remain close to 287 pm. Figure 3.7 b) shows the t-plot of the Rh-Rh

Table 3.3.: Crystallographic data of β-SrRh$_2$As$_2$

Empirical formula	SrRh$_2$As$_2$
Crystal system, space group	orthorhombic, $Fmmm(10\gamma)\sigma00$
a, b, c (pm)	1114.4(3), 574.4(2), 611.5(2)
Cell volume (nm^3)	0.3914 (2)
Molar mass (g/mol)	443.3
Calculated density (g/cm^3), Z	7.52, 4
Radiation type, λ (Å)	Mo-Kα, 0.7107
Temperature (K)	293
2θ range	5.7272 - 58.6562
Transmission (min, max)	0.23117, 1.000
Absorption coefficent (mm^{-1})	38.425
Total number of reflections	23001
Independent reflections, R$_{int}$	1271, 0.0470
Reflections with $I > 3\sigma(I)$, R_σ	833, 0.0105
Main reflections: $I > 3\sigma(I)$/ all	327/ 479
1. order satellites: $I > 3\sigma(I)$/ all	225/ 258
2. order satellites: $I > 3\sigma(I)$/ all	281/ 534
Refined parameters, Goodness-of-fit on F^2	47 , 5.90
R_{obs} $I > 3\sigma(I)$/all	0.0563/ 0.0918
Main reflections:	0.0424/ 0.0567
1. order satellites:	0.0569/ 0.0658
2. order satellites:	0.0911/ 0.19524
$wR2$ $(I > 3\sigma(I))$, $wR2$ (all)	0.1089/ 0.1260
Main reflections:	0.0982/ 0.0991
1. order satellites:	0.1045/ 0.1054
2. order satellites:	0.1364/ 0.1942
Residual peak, hole e^-/Å^3	6.67/-5.66

Table 3.4.: parameters of the modulation functions of β-SrRh$_2$As$_2$

Atom		x, y, z	U_{11}	U_{22}	U_{33}
Rh	8d	0.75, 0.25, 0.25	0.0252(7)	0.0083(5)	0.0282(7)
Sr	4d	0, 0.5, 0	0.0163(11)	0.0103(12)	0.0174(10)
As	8d	0.1410(2), 0, 0	0.0198(8)	0.0312(10)	0.0204(7)

Fourier coefficients of the modulation functions

		u_x^S	u_y^S	u_z^S	u_x^C	u_y^C	u_z^C
Rh	1. order						
		0	0	-0.0621(5)	0	0	0
	2. order						
		0	0	0.0255(6)	0	0	0
Sr		-0.0141(2)	0	0	0	0	0
As		-0.01136(14)	0	0.0278(3)	0.01391(17)	0	0.0227(2)

Crenel function	width	center
Rh	1	0.5

Coefficients of the modulation function of the ADP parameters

Atom	term	U_{11}	U_{22}	U_{33}
Rh	s	0	0	0
	c	-0.0000(9)	0.0034(8)	0.00442(15)
Sr	s	0	0	0
	c	0	0	0
As	s	-0.0040(9)	-0.0220(6)	-0.0081(4)
	c	0.0049(12)	0.0269(7)	0.0099(5)
		U_{12}	U_{13}	U_{23}
Rh	s	0.0013(6)	0	0
	c	0	0	0
Sr	s	0	0	0
	c	0	-0.0015(6)	0
As	s	0	-0.0079(7)	0
	c	0	-0.0064(5)	0

Table 3.5.: crystallographic data of α-SrRh$_2$As$_2$ in the multiphase refinement

Atom	x	y	Z	Uiso
Sr1	0.246(2)	0.757(2)	0.1294(11)	0.020(3)
Rh1	0.215(3)	0.5007(13)	0.3911(15)	0.0104(19)
Rh2	0.308(5)	0.0046(14)	0.348(2)	0.028(2)
As1	0.207(4)	0.4015(15)	0.128(2)	0.038(5)
As2	0.273(3)	0.1244(11)	0.1169(16)	0.021(3)
twinning matrices: β-phase to α-phase				
1. (0 1 0 -0.5 0 -1 -0.5 0 1)	2. (0 -1 0 -0.5 0 -1 0.5 0 -1)			

distances. As expected, the biggest change of the Rh-Rh distances takes place near the "jump" of the Rh modulation function. The Rh-As distances (t-plot shown in Figure 3.7 a) vary from $\sim$227 pm to 257 pm, the variation is bigger than in α-SrRh$_2$As$_2$. Both the minimal and maximal distances occur near the jump of the modulation function of the Rh-atom, as the As atoms adjust to their bonding partner. Near this point, also enlarged atomic displacement parameters are observed (Figure 3.6).

This model describes the essential characteristics of the modulated structure of β-SrRh$_2$As$_2$, even though the much weaker satellite reflections with **q** = (0.5, 0, $\approx$1/6) are still neglected. These will probably allow to describe the modulation in more detail, and maybe help to improve both displacement parameters and Rh-As distances close to the jump of the modulation. However, due to the very weak intensity of these spots, we were not able to measure them with the accuracy required to improve our model.

Previous publications[71] mentioned the β-phase as a high temperature polymorph stable between about 463 and 555 K. We confirm these results as we could observe the phase transition from α to β- phase with high temperature powder diffraction. A flux synthesized crystal of β-SrRh$_2$As$_2$ showed still the same satellite reflections found at room temperature at 563 K, but the quality was not
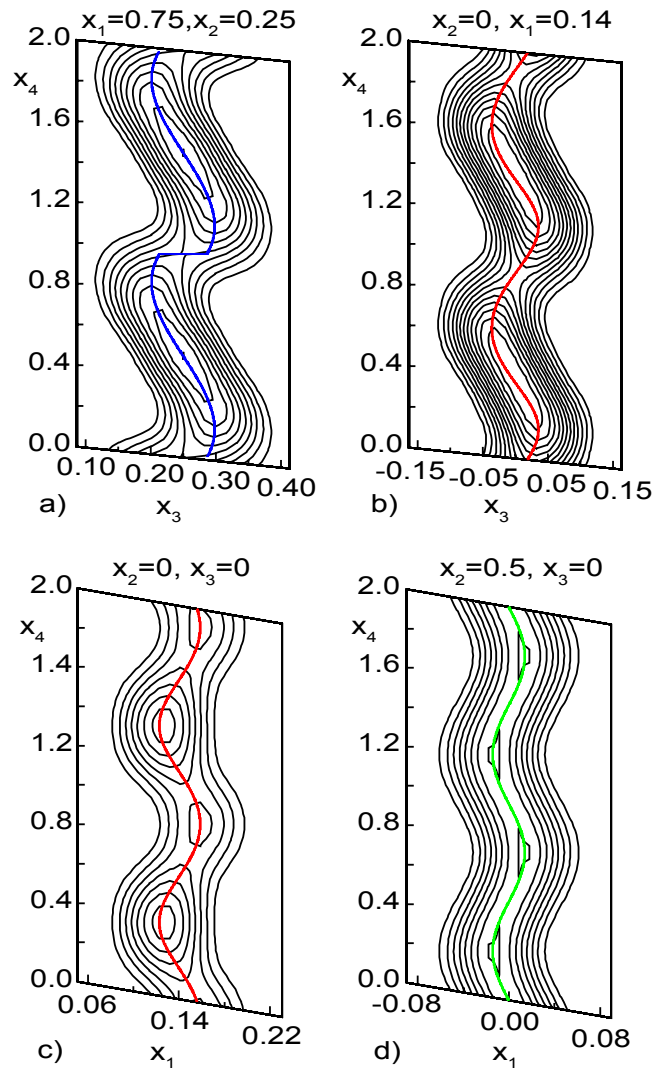
Fig. 3.5.: Fourier map with a) positional modulation of Rh in *c*-direction, b) of As in *c*-direction, c) Positional modulation of As in *a*-direction, d) of Sr in *a*-direction.

sufficient for further x-ray analysis. Upon cooling, the crystal transformed to α-SrRh$_2$As$_2$, the stable polymorph at room temperature.

One might remark that powder samples β- and α-phase were synthesized under very similar conditions (section 3.2). Indeed, although the synthesis of polycrystalline β-SrRh$_2$As$_2$ could be reproduced, later experiments gave α-SrRh$_2$As$_2$. It seems that β-SrRh$_2$As$_2$ can be quenched only under certain conditions (as it is the case in the flux). Figure 3.8(a) displays the rietveld-refined x-ray pattern of a powder sample of β-SrRh$_2$As$_2$ (black and green tick marks) with 16 % α-
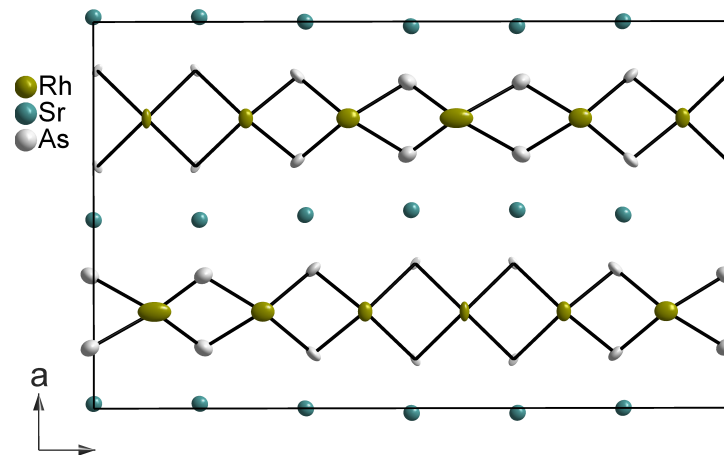
**Fig. 3.6.:** Modulated structure of β-SrRh$_2$As$_2$, projection along b.

SrRh$_2$As$_2$ as side phase (light blue tick marks). β-SrRh$_2$As$_2$ was refined in the superspace group $Fmmm(10\gamma)\sigma00$ with a slightly simplified version of the structure model presented above, taking into account only the first order satellite reflections. These reflections are clearly visible in the diffraction pattern 3.8(b) (top, green tick marks) and the reason a refinement with just the basic structure gives no satisfactory fit of the data, as Figure 3.8(b) (bottom) shows, where β-SrRh$_2$As$_2$ was refined in Fmmm without the modulation.

Although β-SrRh$_2$As$_2$ can be quenched to room temperature under certain conditions, the polymorph is not entirely stable at this temperature and slowly transforms to α-SrRh$_2$As$_2$. The fraction of α-phase in the single crystal of β-SrRh$_2$As$_2$ used for structure determination increased from 7 % to about 30 % within one year at ambient conditions. A similar increase of the content of α-SrRh$_2$As$_2$ was observed for a powder sample. Under pressure, the transformation to the stable α phase takes place rather quickly: at a pressure of 1 - 2 GPa in a hand press, β-SrRh$_2$As$_2$ changes completely into α-SrRh$_2$As$_2$ within 30 minutes (Figure 3.9).

β-SrRh$_2$As$_2$ has the characteristics of a pauli-paramagnetic metal: Magnetic susceptibility measurements from 300 to 1.8 K on a sample of β-SrRh$_2$As$_2$ with some fraction of α-SrRh$_2$As$_2$ showed values typical for a Pauli-paramagnetic
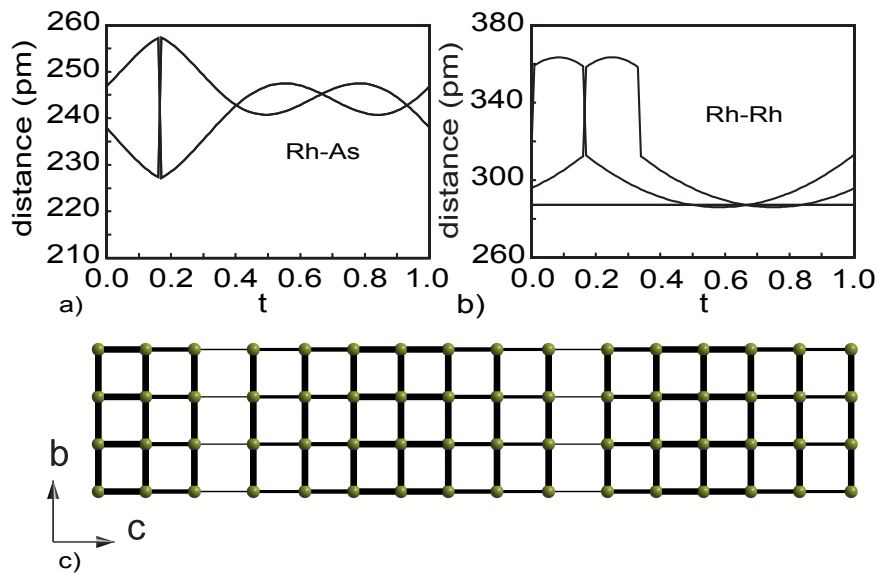
Fig. 3.7.: a) t-plot of the Rh-As distances (pm), b) t-plot of the Rh-Rh distances (pm), c) Rh-Rh network in β-SrRh$_2$As$_2$, elongated distances are shown with thinner lines.

(a)   **(b)**
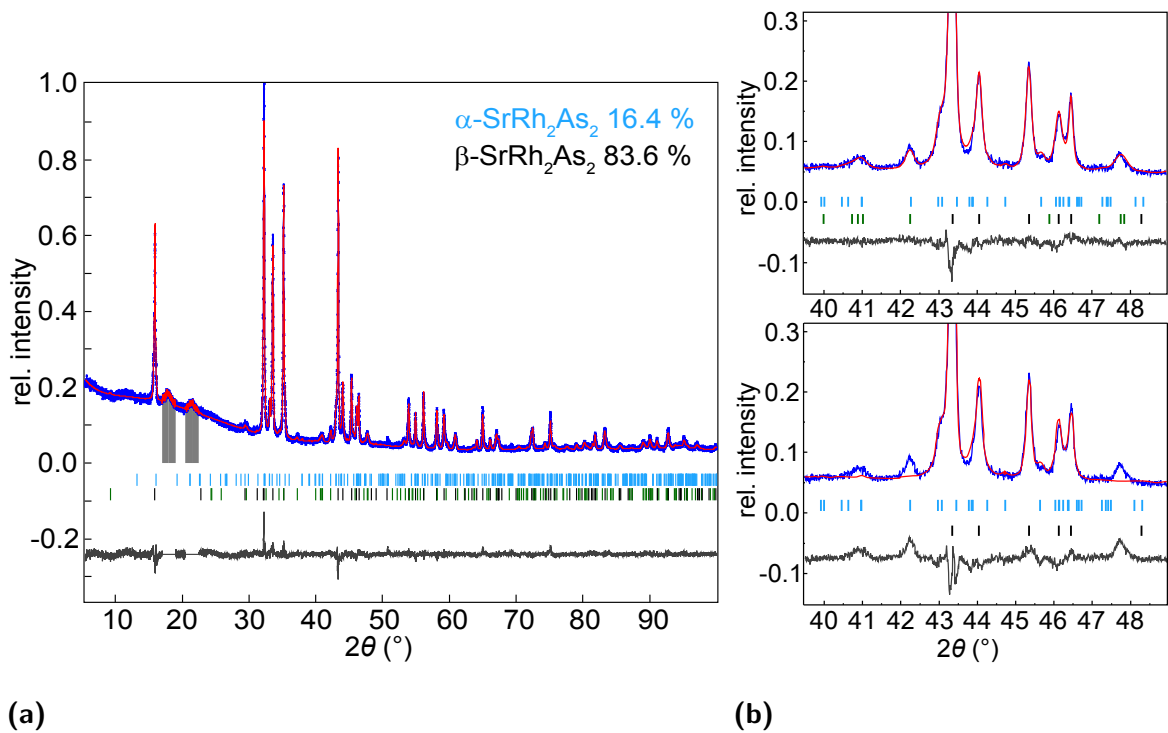
Fig. 3.8.: (a) X-ray powder pattern (top, blue), Rietveld fit (top, red) and difference curve (bottom) of β-SrRh$_2$As$_2$ (black tick marks, satellite reflections green tick marks), side phase α-SrRh$_2$As$_2$ (light blue tick marks), excluded regions marked in gray. (b) section of the rietveld refinement of β-SrRh$_2$As$_2$ with satellite reflections (top) or of the basic structure (bottom).
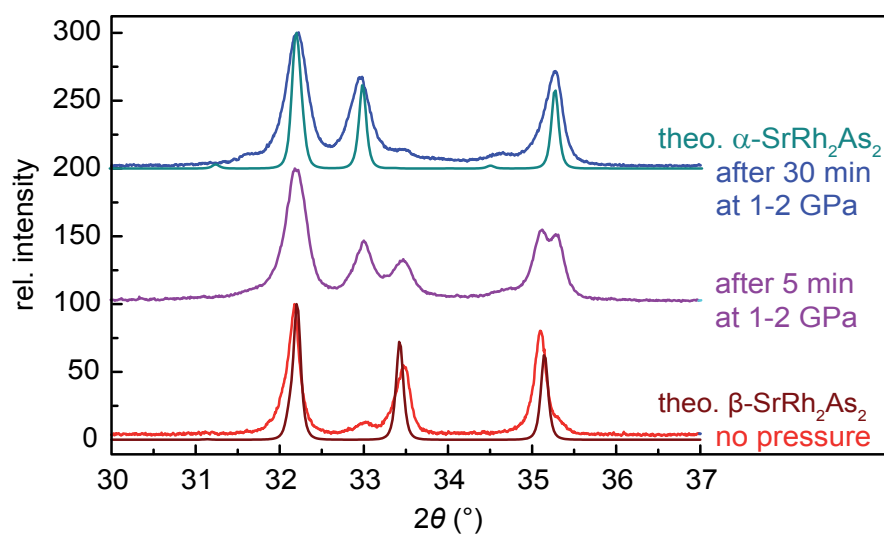
Fig. 3.9.: α-SrRh$_2$As$_2$ transforms to β-SrRh$_2$As$_2$ under pressure, bottom: diffractogram before pressure treatment, middle: diffractogram taken at ambient pressure after 5 min at 1 - 2 GPa and 298 K, top: after 30 min at 1 - 2 GPa.

metal (between $\sim 5.2 \cdot 10^{-9}$ and $5.75 \cdot 10^{-9}$ m^{3}mol^{-1}, making the susceptibility almost temperature-independent), although some traces of ferromagnetic impurity were observed.

3.5. γ-SrRh$_2$As$_2$

Several attempts to obtain powder samples or single crystals of γ-SrRh$_2$As$_2$ by quenching from high temperatures remained unsuccessful, but the diffraction pattern of a β-SrRh$_2$As$_2$ crystal measured at 623 K showed tetragonal symmetry. As described in the literature[71], γ-SrRh$_2$As$_2$ crystallizes in the tetragonal ThCr$_2$Si$_2$-type structure (Table 3.6). The lattice parameter c is 1156.1(3) pm at 623 K, thus elongated compared to 1143.1(6) pm as reported for the γ-phase at room temperature.[71] Also the ADP parameters are enlarged due to the higher temperatures.

**Table 3.6.:** Crystallographic data of γ-SrRh$_2$As$_2$

Empirical formula	SrRh$_2$As$_2$
Crystal system, space group	Tetragonal, $I4/mmm$, No. 139
a, c (pm)	412.68(6), 1156.1(3)
Cell volume (nm^3	0.19688(6)
Molar mass (g/mol)	443.3
Calculated density (g/cm^3), Z	7.477, 2
Radiation type, λ (Å)	Ag-Kα, 0.56087
Temperature (K)	623
2θ range	4.6 - 60.9
Transmission (min, max)	0.0605, 0.6104
Absorption coefficent (mm^{-1})	20.32
Total number of reflections	2268
Independent reflections, R$_{int}$	213, 0.1229
Reflections with $I > 2\sigma(I)$, R_σ	168, 0.0604
Refined parameters, Goodness-of-fit on F^2	8, 1.158
R_1, $wR2$ ($I > 2\sigma(I)$)	0.0376, 0.1392
R_1, $wR2$ (all data)	0.0516, 0.1623
Largest residual peak, hole e^-/Å^3	4.164, -1.494

Atomic parameters:

Sr	2a	$(0,0,0)$	U$_{eq}$ = 0.0211(4)
Rh	4d	$(0,0.5,0.25)$	U$_{eq}$ = 0.0286(4)
As	4e	$(0,0,z)$, $z = 0.3637(2)$	U$_{eq}$ = 0.0255(4)

3.6. Electronic structure and discussion

The distortions of the ThCr$_2$Si$_2$-type structure in SrRh$_2$As$_2$ mainly affect the Rh-Rh bonds within the RhAs$_{4/4}$-layer, while the changes of other bond lengths may be regarded as consequences of that. It seems probable that the origin of the polymorphism lies in the Rh-Rh bonding situation, which has been analyzed by the Crystal Orbital Hamilton Population (COHP) method[78]. Figure 3.10 shows

COHP curves of the Rh-Rh bonds in tetragonal γ-SrRh$_2$As$_2$ with ThCr$_2$Si$_2$-type structure and monoclinic α-SrRh$_2$As$_2$. For γ-SrRh$_2$As$_2$ (Figure 3.10 a)), the calculations show strongly Rh-Rh antibonding states around the Fermi energy E$_F$, caused by $dd\sigma$*-type interactions of the in-plane rhodium orbitals within the square network as shown in Figure 3.2 (right). As those interactions are quite unfavourable, one would expect the situation to be improved in the low temperature phases. The very similar situation of SrRh$_2$P$_2$ has been analyzed earlier in detail.[80] If we look at the structural changes within this Rh-Rh network for the low temperature phases, we first find the distortion from tetragonal to orthorhombic in β-SrRh$_2$As$_2$. The additional modulation causes strong elongations of several Rh-Rh-bonds (Figure 3.7 c)). Every seventh bond along c is stretched to 358.0 pm, with the adjoining bonds elongated slightly to 313.2 and 295.8 pm. All other bonds in this direction and all bonds along b are almost the same as in the γ-phase, with 287.12 pm and 287.4 pm compared to 290 pm in γ-SrRh$_2$As$_2$. This elongation of several bonds without much shortening of others is also reflected by the lattice parameters: The identical diagonals in the tetragonal γ-phase are $a\cdot\sqrt{2} = 581.5$ pm, and split into 574.4 pm (-7 pm) and 611.5 pm ($+30$ pm) in the β-phase. The monoclinic distortion in α-SrRh$_2$As$_2$ is even more successful in elongating Rh-Rh distances (Figure 3.2): every fourth distance is widened to 378 pm. The effect of the structural changes on the bonding situation in α-SrRh$_2$As$_2$ can be studied in the Rh-Rh COHP that is shown in Figure 3.10 (right). Most of the antibonding states that were present at E$_F$ in γ-SrRh$_2$As$_2$ have been lowered in energy, and are thus less unfavourable. This can be considered as a typical CDW scenario, where compounds compensate highly symmetric but unfavourable bonding situations by splitting bonds in longer and shorter ones yielding lower symmetry structures. More detailed calculations and analysis of the electronic structure including the Fermi surface topology are still necessary to obtain details of a CDW scenario, but are beyond the scope of this work.

In spite of some similarities, this situation is clearly different from that in
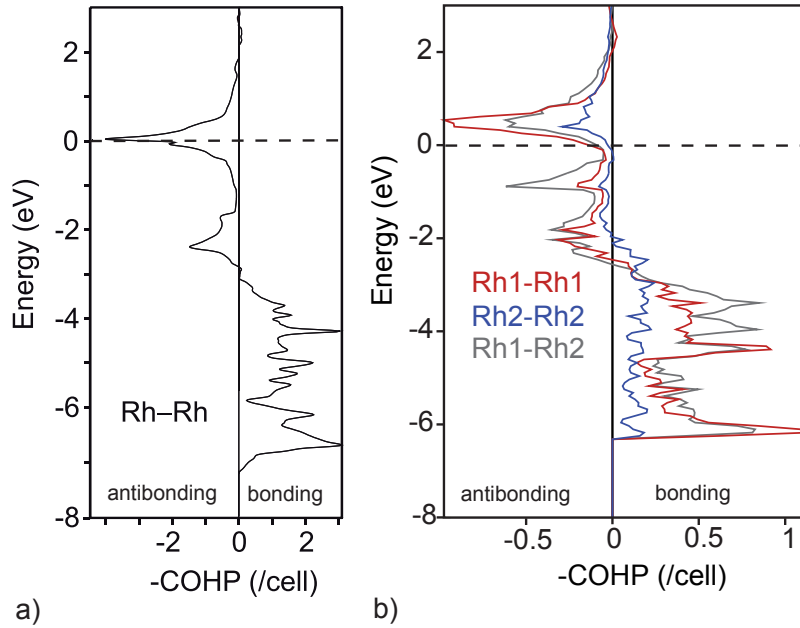
Fig. 3.10.: a) Rh-Rh-COHP of tetragonal γ-SrRh$_2$As$_2$ b) Rh-Rh-COHP of monoclinic α-SrRh$_2$As$_2$

BaFe$_2$As$_2$, where the orthorhombic distortion is much smaller and intimately connected to magnetic interactions. Our results suggest that the much more pronounced effect in SrRh$_2$As$_2$ is caused by the larger overlap the in-plane $4d$-orbitals responsible for strong Rh-Rh bonding. The higher electron count of SrRh$_2$As$_2$ places the Fermi-level just in the middle of the Rh-Rh antibonding $dd\sigma^*$-bands which can be stabilized by splitting in a structure with lower symmetry. This is different in BaFe$_2$As$_2$, where the Femi-level cuts Fe-Fe antibonding bands of $dd\pi^*$ character that overlap too weak to cause a strong lattice distortion.

3.7. Conclusions

In summary, single crystals and powder samples of SrRh$_2$As$_2$ have been synthesized the structures of three polymorphs have been studied in detail. The up to now unknown structure of α-SrRh$_2$As$_2$ was solved, that crystallizes in the monoclinic space group P2$_1$/c with $a = 421.2(1)$ pm, $b = 1105.6(2)$ pm, $c = 843.0(1)$ pm and $\beta = 95$ ° and is twinned. The previous structural model for β-SrRh$_2$As$_2$

was revealed to describe only the average structure. A structural modulation with $\mathbf{q} = (0.5, 0, 0.1655)$ was found, where second order satellites are much stronger than first order satellites. Taking into account the strong satellites we present an incommensurate structure in the (3+1) dimensional superspace group Fmmm$(10\gamma)\sigma00$ with the unit cell parameters $a = 1114.4(3)$ pm, $b = 574.4(2)$ pm and $c = 611.5(2)$ pm and a modulation vector $\mathbf{q} = (1, 0, 0.3311(4))$. The strong modulation of the Rh atom could be described by a crenel function and leads to a variation of the Rh-Rh distances along c from to 287 pm to 358 pm. For the γ-phase, high temperature single crystal data confirm the ThCr$_2$Si$_2$-type structure of γ-SrRh$_2$As$_2$ as reported in literature. DFT calculations with COHP bonding analysis show that distortion and elongation of Rh-Rh bonds lead to lowering in energy of antibonding states in α-SrRh$_2$As$_2$ compared to tetragonal γ-SrRh$_2$As$_2$, thus the driving force of the lattice distortions comes from Rh-Rh bonding and has no magnetic origin as suggested for BaFe$_2$As$_2$.

4. CaRh$_2$As$_2$ and Sr$_{1-x}$Ca$_x$Rh$_2$As$_2$

4.1. Introduction

Several alkaline earth and rare earth rhodium arsenides with composition 1:2:2 have been synthesized and characterized so far, among them SrRh$_2$As$_2$, BaRh$_2$As$_2$, EuRh$_2$As$_2$[71] and LaRh$_2$As$_2$[81]. BaRh$_2$As$_2$ was reported to crystallize in the well-known tetragonal ThCr$_2$Si$_2$-type structure, where layers of edge sharing RhAs$_{4/4}$ tetrahedra alternate with barium atoms[71]. In BaRh$_2$As$_2$ this structure remains stable at low temperatures, no phase transitions were found[82]. SrRh$_2$As$_2$, on the contrary, shows a more interesting structural chemistry, as described in the previous chapter.

The structural diversity of SrRh$_2$As$_2$, especially the existance of an incommensurate β-phase, seems to be quite unique among the ternary arsenides with (high temperature) ThCr$_2$Si$_2$-type structure. However, incommensurable modulated phases have been reported both for SrPt$_2$As$_2$ and EuPt$_2$As$_2$[83] where the average structure of can be derived from the CaBe$_2$Ge$_2$-type structure with its alternating PtAs$_{4/4}$ and AsPt$_{4/4}$ tetrahedra layers. The modulated structure of SrPt$_2$As$_2$ was solved and refined in the superspace group $Pmmn(\alpha00)0\sigma0$ with $\mathbf{q} = (0.62, 0, 0)$, the modulation having both occupational and displacive components within the RhAs$_{4/4}$ tetrahedra layer. Under pressure, a lock-in phase transition with doubling of a was found at 60 kbar. This rises the question how SrRh$_2$As$_2$ would react to pressure. A way to apply internal or "chemical pressure" is the substitution of Sr by Ca, as the ionic radius of Ca is smaller than the radius of Sr. However, CaRh$_2$As$_2$ is unknown so far, only two ternary calcium rhodium

arsenides - Ca$_4$Rh$_{13}$As$_9$[84] and CaRh$_6$As$_4$[85] are described in the literature, but no compound with the composition 1:2:2.

Here not only synthesis and properties of CaRh$_2$As$_2$, but also a detailed investigation of the effects of "chemical pressure" on the structure of SrRh$_2$As$_2$ in the solid solution Sr$_{1-x}$Ca$_x$Rh$_2$As$_2$ are reported.

4.2. Experimental Methods

For the synthesis of polycrystalline CaRh$_2$As$_2$ stoichiometric mixtures of Ca and RhAs were heated in alumina crucibles, sealed in silica tubes under an atmosphere of purified argon, heated to 1313 K and kept at this temperature for 30 h. The reaction products were homogenized and annealed at 1313 K three times for 30-60 h. Single crystals of CaRh$_2$As$_2$ were obtained by heating the elements first to 1123 K (10h), homogenizing, annealing for 110 h at 1273 K and cooling to room temperatur at 10 K/h. To synthesize Sr$_{1-x}$Ca$_x$Rh$_2$As$_2$, stoichiometric mixtures of the elements were heated to 893 K with 50 K/h and kept at this temperature for 10 h. This first step was followed by several annealing steps at 1093 K (10 h) and 1273 K (three times, 20-50 h). After each step, the sample was well homogenized. For some samples, RhAs or Ca$_4$Rh$_{13}$As$_9$ and CaRh$_6$As$_4$ were observed as impurity phases. Single crystals of Sr$_{1-x}$Ca$_x$Rh$_2$As$_2$ could be obtained as following: After a first reaction step at 973 K (10 h) the sample was thoroughly homogenized, heated to 1423 K and kept at this temperature for 20 h before cooling to room temperature at a rate of 5 K/h.

X-ray powder diffractograms were collected on a STOE Stadi-P (Cu Kα_1-radiation) and for Rietveld refinements, the TOPAS[74] package or Jana2006[77]was used. Single crystal intensity data of CaRh$_2$As$_2$ was recorded on a STOE IPDS imaging plate detector (Mo-Kα, graphite monochromator, ϕ-scan). For structure solution and refinement, the SHELX suite of programs and the program Jana2006 were used. Resistivity was measured with a cold pressed and annealed (873 K)

(a)   **(b)**
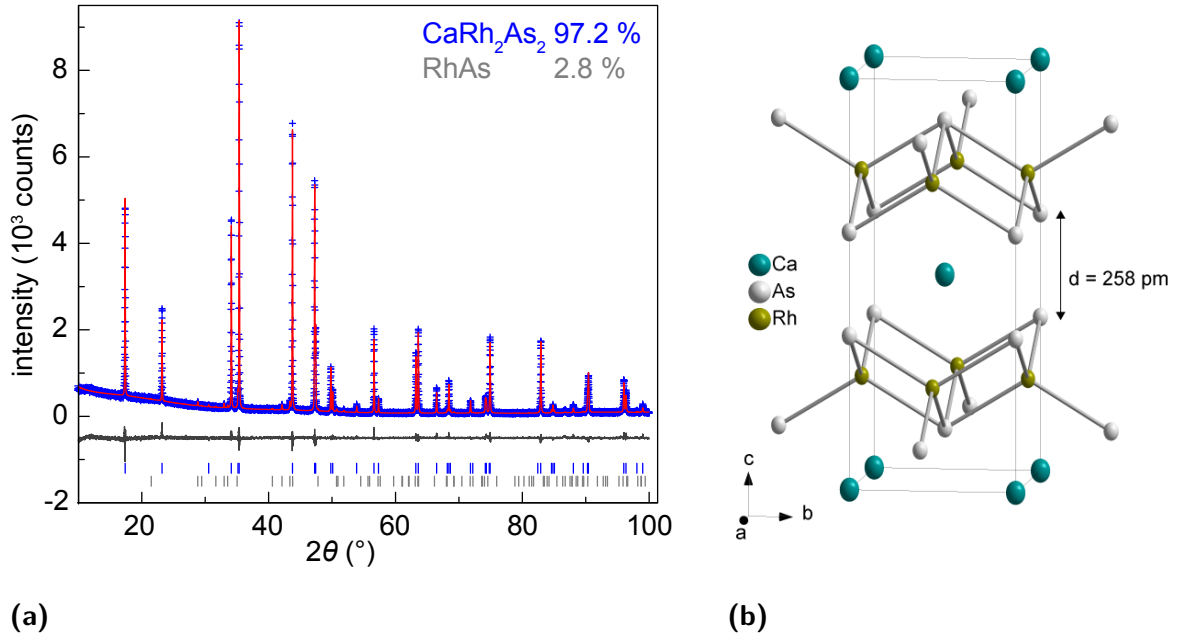
Fig. 4.1.: (a) X-ray powder pattern (top, blue), Rietveld fit (top, red) and difference curve (bottom) of CaRh$_2$As$_2$ (blue tick marks) containing 2.8 % of RhAs (grey tick marks). (b) crystal structure of CaRh$_2$As$_2$.

pellet using by the four probe method. The magnetic properties were measured utilizing a SQUID magnetometer (MPMS-XL Quantum Design Inc.). The Ca content of the Sr$_{1-x}$Ca$_x$Rh$_2$As$_2$ samples was determined by EDX measurements where variations by no more than $\pm$ 4 % were found.

4.3. Results and Discussion

Figure 4.1(a) shows the powder diffraction pattern and rietveld refinement of polycrystallinic CaRh$_2$As$_2$; a small percentage of RhAs is observed as impurity phase. CaRh$_2$As$_2$ crystallizes in the ThCr$_2$Si$_2$-type structure as confirmed by single crystal data. The crystal structure was solved and refined in the tetragonal space group $I4/mmm$ with $a = 415.0(6)$ pm and $c = 1023(2)$ pm (see 4.1) with a reasonable R$_1$-value of 0.0628. Figure 4.1(b) presents the unit cell of CaRh$_2$As$_2$ (anisotropic displacement parameters with 90 % probability are shown) and Table

4.1 gives an overview of distances and angles in CaRh$_2$As$_2$. The Rh-As distance is 243.1(3) pm, close to the 240 pm expected for a Rh-As bond. Compared to the homologous alkaline earth rhodium arsenides, c is much shorter and a compression of the RhAs$_4$-tetrahedra layers along c is observed, with the As-Rh-As angle ε' reduced to 105.75(8)° and the corresponding As-Rh-As angle ε increased to 117.20(17)°. Adding to the effect is a slight elongation of a to a value of 415.0(6) pm in CaRh$_2$As$_2$ compared to 405 pm in BaRh$_2$As$_2$ and close to the 412.6 pm observed for γ-SrRh$_2$As$_2$ at 623 K. Consequently, the Rh-Rh distance of 293.4(4) pm in CaRh$_2$As$_2$ is longer than the 286.6 pm reported for BaRh$_2$As$_2$ and close to 291.8 pm observed in γ-SrRh$_2$As$_2$ at 623 K. In the low temperature phases of SrRh$_2$As$_2$, the shortest Rh-Rh distances are 284.7(3) pm (α-phase) and 287 pm (β-phase), much shorter than in what is observed here in CaRh$_2$As$_2$. The main difference between CaRh$_2$As$_2$ and the other homologous rhodium arsenides however lies in the As-As distance between the RhAs$_4$-tetrahedra layers: while 315 pm are observed for α-SrRh$_2$As$_2$ and $\approx$ 390 pm in BaRh$_2$As$_2$ or γ-SrRh$_2$As$_2$, the As-As distance in CaRh$_2$As$_2$ is 258.2(8) pm and As-As bonding can be expected.

Unlike γ-SrRh$_2$As$_2$, CaRh$_2$As$_2$ undergoes no structural phase transitions. Low temperature powder diffraction shows no splitting of reflections at low temperatures. The resistivity of CaRh$_2$As$_2$ (Figure 4.2(a)) gives no hint at anomalies, metallic behaviour with ρ_s = 0.025 mΩm at 300 K is observed. The susceptibility of the compound is in the range of a Pauli-paramagnetic metal (5.3-5.42 · 10^{-9} mol^{-1} m^3) and is almost temperature independent between 1.8 K and 250 K (Figure 4.2(b)).

Our results show that the structure of CaRh$_2$As$_2$ remains tetragonal at low temperatures, in contrast to SrRh$_2$As$_2$, where two phase transitions associated with a rather strong distortion of the RhAs$_4$-layers are observed. To find out how the structure of SrRh$_2$As$_2$ changes under chemical pressure with increasing Ca content, we prepared the solid solution Sr$_{1-x}$Ca$_x$Rh$_2$As$_2$.

**Table 4.1.:** Crystallographic data of CaRh$_2$As$_2$

Empirical formula	CaRh$_2$As$_2$
Crystal system, space group	Tetragonal, *I4/mmm*, No. 139
a, *c* (pm)	415.0(6), 1023(2)
Cell volume (nm^3)	0.1762(5)
Molar mass (g/mol)	395.8
Calculated density (g/cm^3), *Z*	7.46, 2
Radiation type, λ (Å)	Mo-Kα, 0.71073
Temperature (K)	293
2θ range	4.6 - 60.9
Transmission (min, max)	0.2404, 0.5691
Absorption coefficent (mm^{-1})	29.185
Total number of reflections	797
Independent reflections, R$_{int}$	101, 0.1444
Reflections with $I > 2\sigma(I)$, R_σ	88, 0.0607
Refined parameters, Goodness-of-fit on F^2	8, 1.044
R_1, $wR2$ ($I > 2\sigma(I)$)	0.0628, 0.1603
R_1, $wR2$ (all data)	0.0664, 0.1584
Largest residual peak, hole $e^-/\text{Å}^3$	3.404, -1.837

Atomic parameters:

Ca	2*a*	$(0, 0, 0)$	U$_{eq}$ = 0.0113(14)
Rh	4*d*	$(0, 0.5, 0.25)$	U$_{eq}$ = 0.0162(9)
As	4*e*	$(0, 0, z)$, $z = 0.3738(3)$	U$_{eq}$ = 0.0173(9)

Interatomic distances and angles

distance (pm)	Rh-Rh	293.4(4)
	Rh-As	243.1(3)
	As-As	258.2(8)
	Ca-As	320.6(4)
	Ca-Rh	329.3(4))
angle (°)	As-Rh-As	105.75(8)
	As-Rh-As	117.20(17)

(a)   **(b)**
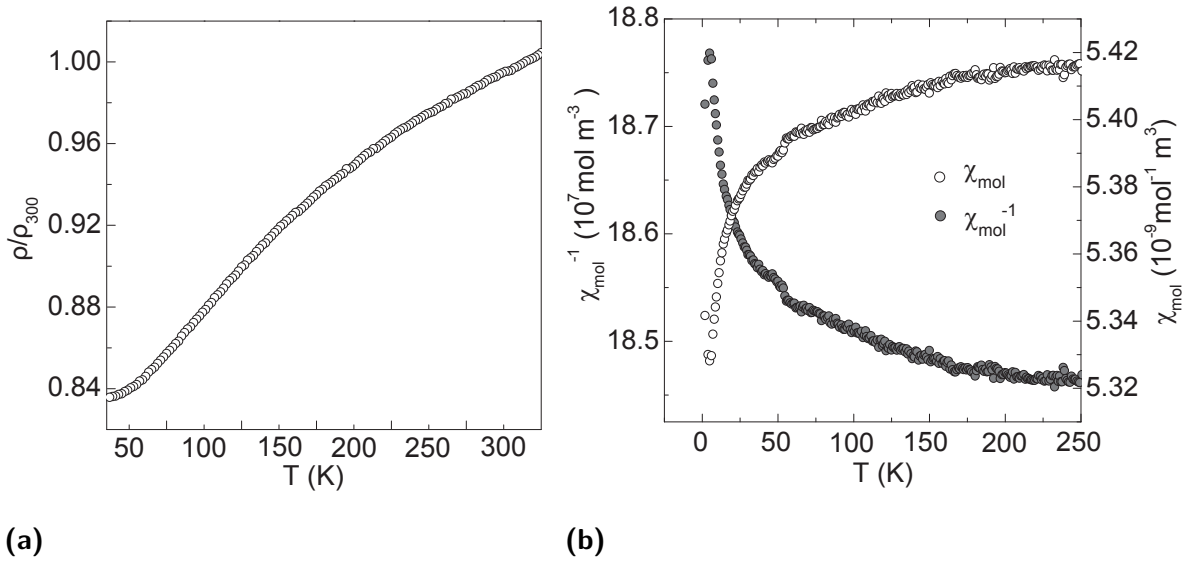
Fig. 4.2.: (a) Normalized electrical resistance ρ/ρ_{300} of CaRh$_2$As$_2$. (b) molar susceptibility χ_{mol} (open symbols) and inverse molar susceptibility (filled symbols) of CaRh$_2$As$_2$.
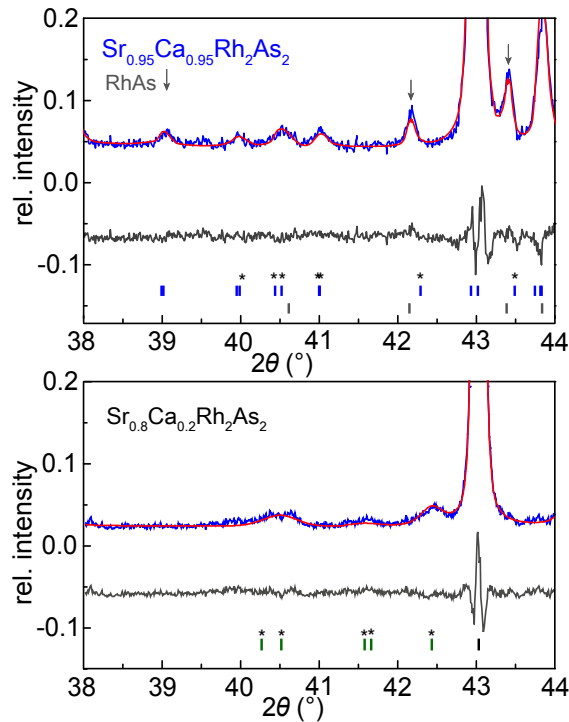
Fig. 4.3.: Section of the rietveld refinement of Sr$_{1-x}$Ca$_x$Rh$_2$As$_2$ with $x = 0.05$ (top) and $x = 0.2$ (bottom). The tick marks of the reflections doubling the c axis (top) of the α-phase and the satellite reflections of the β-phase (green, bottom) are marked with asterisks.

Table 4.2.: Crystallographic data of $Sr_{0.57}Ca_{0.43}Rh_2As_2$

Crystal system, space group	orthorhombic, $Fmmm(10\gamma)\sigma00$
a, c (pm)	1062.0(5), 579.1(3), 614.1(3)
q-vector	(1, 0, 0.347)
Cell volume (nm^3)	0.3914 (2)
Molar mass (g/mol)	443.3
Calculated density (g/cm^3), Z	7.447, 4
Radiation type, λ (Å)	Mo-Kα, 0.7107
Temperature (K)	293
2θ range	3.84 - 30
Transmission (min, max)	0.143, 0.0618
Absorption coefficent (mm^{-1})	34.74
Total number of reflections	3855
Independent reflections, $R_{int}(all)$	1476, 0.1063
Reflections with $I > 3\sigma(I)$, $R_\sigma(all)$	653, 0.069
Main reflections: $I > 3\sigma(I)$/ all	391/551
1. order satellites: $I > 3\sigma(I)$/ all	262/ 925
Refined parameters, Goodness-of-fit on F^2	26, 4.18
R_{obs} $I > 3\sigma(I)$/all	0.0803, 0.1414
Main reflections:	0.0736/ 0.0955
1. order satellites:	0.1005/ 0.2187
$wR2$ ($I > 3\sigma(I)$), $wR2$ (all)	0.1448/ 0.1492
Main reflections:	0.1429/ 0.1441
1. order satellites:	0.1849/ 0.2377
Residual peak, hole $e^-/Å^3$	0.89/ -1.03
Twin fraction	48.39 %

Table 4.3.: parameters of the modulation functions of Sr$_{0.57}$Ca$_{0.43}$Rh$_2$As$_2$

Atom		x, y, z	U$_{11}$	U$_{22}$	U$_{33}$
Rh	8d	0.75, 0.25, 0.25	0.0236(6)	0.0126(5)	0.0296(10)
Sr	4d	0, 0.5, 0	0.0284(16)	0.0229(12)	0.0239(17)
As	8d	0.1360(2), 0, 0	0.0442(15)	0.0564(19)	0.0446(18)

Fourier coefficients of the modulation functions

		u$_x^S$	u$_y^S$	u$_z^S$	u$_x^C$	u$_y^C$	u$_z^C$
Rh	1. order						
		0	0	-0.0495(5)	0	0	0
Sr		-0.0069(10)	0	0	0	0	0
As		-0.0092(4)	0	0.0131(8)	0.0105(5)	0	0.0114(7)

Crenel function

	width	center
Rh	1	0.5

Coefficients of the modulation function of the ADP parameters

Atom	term	U$_{11}$	U$_{22}$	U$_{33}$
Rh	s	0	0	0
	c	-0.001(5)	0.002(4)	-0.022(4)
Sr	s	0	0	0
	c	0	0	0
As	s	0.0008(19)	-0.034(2)	-0.011(2)
	c	-0.001(2)	0.039(3)	0.012(3)
		U$_{12}$	U$_{13}$	U$_{23}$
Rh	s	0.0029(19)	0	0
	c	0	0	0
Sr	s	0	0	0
	c	0	-0.005(3)	0
As	s	0	-0.007(2)	0
	c	0	-0.0057(18)	0

Effectivly, three different structures are observed for $Sr_{1-x}Ca_xRh_2As_2$: for $SrRh_2As_2$ ($x = 0$), the stable phase at room temperature is the α-phase, which is also observed for $x = 0.05$. However, in the substitution range $0.2 \leq x \leq 0.6$ the compounds crystallize in the orthorhombic β-phase and for $x \geq 0.8$ the orthorhombic splitting ceases and the tetragonal $ThCr_2Si_2$-type γ-phase becomes stable. Figure 4.3 (top) presents in detail a section of the rietveld refinement of $Sr_{1-x}Ca_xRh_2As_2$ with $x = 0.05$: The clearly visible reflections caused by the doubling of c (tick marks marked with asterisks) show the compound crystallizes in the α-phase. For $x = 0.2$ (Figure 4.3 (bottom)) however, these reflections have disappeared, and instead satellite reflections (green tick marks, again marked with asterisks) are observed, indicating that the compound crystallizes in the β-phase. Indeed the diffraction pattern of a mixed crystal with the composition $Sr_{0.57}Ca_{0.43}Rh_2As_2$ shows satellite reflections corresponding to $\mathbf{q} = (1, 0, 0.347)$, indicating an incommensurate modulation. The structure was refined by using structure model of β-$SrRh_2As_2$ in the 3+1 dimensional space group $Fmmm(10\gamma)\sigma00$ with $R_1 = 0.0803$ (the results are summarized in Table 4.2 and 4.3), which is acceptable taking into account that the crystal is a non-merohedral twin. As only first order satellite reflections were observed, the structure model was simplified and the modulation of the Rh-atom described by only one positional modulation wave.

Figure 4.4 summarizes the changes of a, b, c, the cell volume and the As-As-distance between $RhAs_{4/4}$-layers in $Sr_{1-x}Ca_xRh_2As_2$ with increasing Ca substitution. All structural parameters were transformed to the orthorhombic cell for comparison. The parameters show non-linear variations, as might be expected due to the occurence of the three different structure types. In total, a shows a decrease of 8 %, it decreases slightly for $x \leq 0.4$, the slope of the decline becoming steeper for $0.4 \leq x \leq 0.6$ and leveling somewhat for $x > 0.7$. The lattice parameters b and c (and thus the magnitude of the orthorhombic splitting) remain almost the same throughout the stabiliy range of the orthorhombic phase
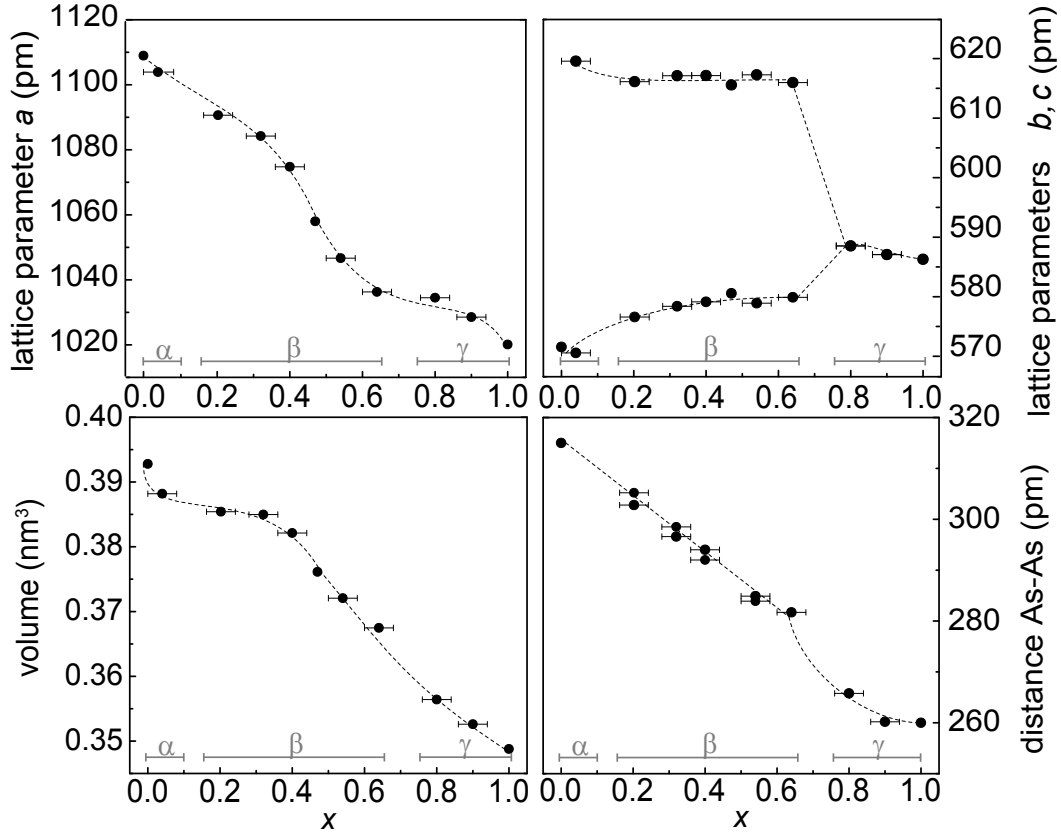
Fig. 4.4.: Structural parameters of Sr$_{1-x}$Ca$_x$Rh$_2$As$_2$ (rietveld refinement data): orthorhombic lattice parameter a in pm (top left), orthorhombic lattice parameters b and c in pm (top right), cell volume in nm^3 (bottom left) and As-As distance d in pm (bottom right). Lattice parameters of α and γ-Phase were transformed to the orthorhombic cell for comparison.

($0.2 \leq x \leq 0.6$). The distortion vanishes only after most of the reduction of a has taken place at $x > 0.6$, then b increases by 1.6 % and c decreases by 2.8 % to 587.0 pm in the tetragonal phase. In total, b increases by 2.5 % and c decreases by 6 %. Figure 4.4 (bottom right) shows how the As-As distance between RhAs$_{4/4}$-layers changes with increasing Ca content. Due to the modulation, a variation of the values is observed for the β-phase, but less pronounced as one might expect from Figure 4.5, as the effects of the displacement in c- and a-direction partly cancel each other out. Upon entering the tetragonal phase, a decrease of the As-As distances from 282 ($x = 0.6$) to 265 pm for $x = 0.8$ is observed.

As we can see, one effect of chemical pressure is the stabilization of first the
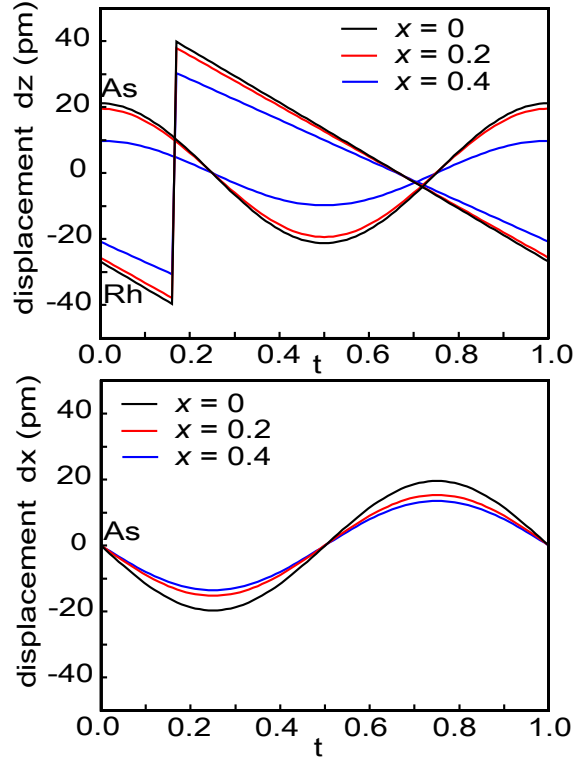
Fig. 4.5.: Displacement of the Rh and As atoms along t in c-direction (top) and of the As atom in a-direction (bottom) for β-SrRh$_2$As$_2$ (black), Sr$_{0.8}$Ca$_{0.2}$Rh$_2$As$_2$ (red) and Sr$_{0.57}$Ca$_{0.43}$Rh$_2$As$_2$ (blue).

β-phase and then the ThCr$_2$Si$_2$-type γ-phase at room temperature. Of interest is also the effect of pressure on the modulation of the incommensurate β-phase. The value of the **q**-vector is found to change slightly from 0.3311 in β-SrRh$_2$As$_2$ to 0.342 for $x = 0.2$ and 0.347 for $x = 0.4$. While the lattice parameters b and c (and thus the orthorhombic distortion) remain almost constant for $0.2 \leq x \leq 0.6$, the displacement of the rhodium atoms in c- direction within the Rh-Rh network becomes weaker, as Figure 4.5 illustrates by comparison of β-SrRh$_2$As$_2$, Sr$_{0.8}$Ca$_{0.2}$Rh$_2$As$_2$ (rietveld refinement data) and Sr$_{0.57}$Ca$_{0.43}$Rh$_2$As$_2$. The amplitude of the modulation for the arsenic atoms in c- and a- direction also decreases, because the modulation becomes less pronounced upon chemical pressure. At the same time, the satellite reflections become weaker, until they are barely visible for $x = 0.5$ (although the modulated model still gives a better fit of the powder data), and finally for $x = 0.6$, the X-ray-pattern shows no hint at satellite

49

reflections.

The effect of pressure on incommensurate to commensurate phase transitions has been extensivly studied for a class of ferroelectrics with composition A$_2$BX$_4$. One example is K$_2$SeO$_4$, that shows a phase transition to an incommensurate phase at 129.5 K, followed by a second, lock-in transition to a threefold superstructure at 93 K[86]. Under pressure, both phase transitions are shifted to lower temperatures. A decrease or increase of the commensurate to incommensurate phase transition temperatures under pressure is frequently observed, for example in Rb$_2$ZnCl$_4$, K$_2$ZnCl$_4$[87] and Sn$_2$P$_2$Se$_6$[88]. In SrPt$_2$As$_2$ the α component of the **q**-vector diminishes continously under pressure, until **q** = (0.5, 0, 0) is reached at 60 kbar and a lock-in phase transition to the two-fold superstructure takes place. In the case of Sr$_{1-x}$Ca$_x$Rh$_2$As$_2$, the chemical pressure introduced by the substitution of Sr by Ca influences not only the **q**-vector and the magnitude of the modulation, but also seems to have an effect on the phase transition temperatures. The temperature of the incommensurate to commensurate phase transition $\beta \rightarrow \alpha$ appears to be lowered under chemical pressure, leading first to the stabilization of the β- then the γ-phase at room temperature.

To summarize, the synthesis of CaRh$_2$As$_2$, a new compound crystallizing in the ThCr$_2$Si$_2$-type structure is reported. A distance of only 258 pm between the arsenic atoms of neighbouring RhAs$_{4/4}$-layers enables As-As bonding in CaRh$_2$As$_2$. The compound is a Pauli-paramagnetic metal and not subject to phase transitions. Investigating the influence of Ca substitution on SrRh$_2$As$_2$, the monoclinic α-phase is found to be stable for $x = 0.05$, the orthorhombic (and incommensurately modulated) β-phase for $0.2 \leq x \leq 0.6$ and the tetragonal (ThCr$_2$Si$_2$-type) γ-phase for $x \geq 0.8$. The lattice parameters show non-linear variations with increasing Ca content and the As-As distance is significantly reduced to 265 pm with the stabilization of the tetragonal phase. The chemical pressure has not only an influence on the **q**-vector, but also diminishes the magnitude of the modulation as illustrated by the weakening of the atomic distortion. The substitution

also seems to lower the phase transition temperatures of the mixed compounds compared to $SrRh_2As_2$.

5. Low temperature single crystal diffraction of $Ba_{1-x}K_xFe_2As_2$

5.1. Introduction

In the last two chapters, structure and properties of ternary rhodium arsenides with $ThCr_2Si_2$-type and related structures were explored, revealing facinating structural features, but no superconductivity. In this capter, the focus is shifted back to the iron arsenide superconductors - more precisely to potassium doped $BaFe_2As_2$. $Ba_{1-x}K_xFe_2As_2$ is certainly one of the most intensivly studied classes of iron arsenide superconductors. While the physical properties of $Ba_{1-x}K_xFe_2As_2$ single crystals have been studied in numerous experiments (including, for example, ARPES measurements, ^{75}As NMR, high pressure studies, RAMAN spectroscopy, etc.), so far little effort has been put into a detailed characterization of their structural properties at low temperatures. The available low temperature diffraction data is mostly from powder diffraction experiments. Tanatar et. al. [89] performed direct imaging of the structural domains in the low temperature phase of single crystalline $BaFe_2As_2$, and Rotundu et. al. [90] carried out neutron scattering experiments on $Ba_{1-x}K_xFe_2As_2$ single crystals, studying the temperature dependent variation of the intensity of the magnetic bragg peaks. However, no structural data from a complete single crystal data set at low temperatures has been published so far. Precise data, not only of the lattice parameters, but also the geometry of the $FeAs_4$ tetrahedra might be interesting, especially as far as differences to room temperature and possible small structural changes around T_c

are concerned. One example of subtle structural changes around T_c is known from the 1111 compounds. For tetragonal NdFeAsO$_{0.85}$ (phase transition completely suppressed), low temperature synchrotron powder diffraction experiments revealed subtle lattice anomalies. A change of slope at ∼180 K was found for the lattice constants, as well as for the Nd-O bond length and the geometry characteristics of the FeAs$_4$-tetrahedra, followed by a saturation at about 135 K (close to T$_N$ for NdFeAsO). Around T_c, smaller modifications leading to a reduction of the lattice anomalies were observed.

One of the downsides of Ba$_{1-x}$K$_x$Fe$_2$As$_2$ single crystals lies in the difficulty to obtain a homogeneous Ba/K ratio. The synthesis is usually carried out at high temperatures in a FeAs flux. Evaporation of Potassium leads to an depletion in potassium during crystal growth and causes inhomogenities in the potassium content of the crystal. Here small, but - as the diffraction experiments show - high quality single crystals of Ba$_{1-x}$K$_x$Fe$_2$As$_2$ ($x = 0$ - 0.43) were synthesized. The diffraction pattern, structure and the variation of the structural parameters at low temperatures were studied by means of synchroton single crystal diffraction.

5.2. Experimental Methods

For the synthesis of high quality single crystals of Ba$_{1-x}$K$_x$Fe$_2$As$_2$ ($x = 0$ - 0.43) the self-flux technique (using an FeAs self-flux) was applied. FeAs was prepared by sealing stoichiometric mixtures of Fe and As in silica ampoules and heating to 1013 K for 20 h. Then stoichiometric amounts of Ba and K and twice the stoichiometric amount of FeAs were filled into niobium tubes, that were welded under an atmosphere of of purified argon and sealed into silica ampoules. The best crystals were obtained by heating the reaction mixtures to 1413 K at a rate of 20 K/h and holding the temperature for 5 h before cooling to 1163 K at a rate of 20K/h and then quickly (200 K/h) to room temperature. The reaction mixture was separated from the niobium tube and, if necessary, carfully crushed. Under a

light microscope, single crystals with a typical size of 50 - 100 μm were selected. In addition to $Ba_{1-x}K_xFe_2As_2$ and FeAs, the reaction product contained some NbFeAs as a side phase. The crystal quality was checked by the Laue method. If the crystal quality was satisfactory, laboratory single-crystal datasets were collected on a STOE IPDS-I diffractometer with imaging plate detector using Mo-K$_\alpha$ radiation (graphite monochromator, $\lambda = 0.71073$ Å). The composition of the crystals was determined and the best crystals were selected. Synchrotron data was collected with $\lambda = 0.15818$ at beamline ID11 at the ESRF (Grenoble) on a heavy duty Huber diffractometer with a vertical rotation axis that was equipped with a Frelon2K CCD detector. The crystal to detector distance was set to 9.38 cm. For low temperature data collection (10- 70 K) a Helijet (Oxford Diffraction) was used. The crystals were mounted on a cryo loop (Hampton Research, Mounted Cryoloop, 20 micron, 0.05-0.2 mm loop size) with Paratone-N cryo oil. The temperature was calibrated with a powder sample of $TbAsO_4$ (see appendix A.2), showing a likely temperature offset by 5 K to lower temperatures (not yet substracted for the data shown in this chapter). The collected .edf frames were converted to Bruker format and the reflections indexed with the SMART[91] program, integrated using SAINT[92] and an absorption correction was applied with the program sadabs[93]. The data was cut off at a high resolution limit of 0.35 with XPREP[94] then solved and refined with the SHELX suite of programs[75,76]. For further data analysis and the calculation of diffraction planes, the ImageD11 suite of programs[95] was used. The superconducting transition temperatures of individual crystals were determined by zero-field-cooled/field-cooled measurements in a SQUID magnetometer (MPMS-XL Quantum Design Inc.). An example is given in Figure 5.1: for a crystal with composition $Ba_{0.76}K_{0.24}Fe_2As_2$ $T_c = 26$ K was determined .
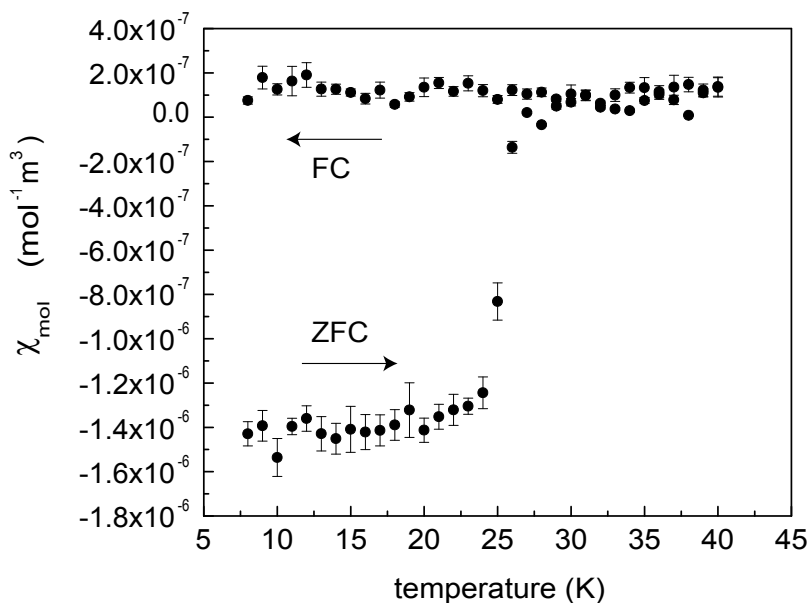
Fig. 5.1.: Zero-field-cooled/field-cooled measurement of a crystal with composition $Ba_{0.76}K_{0.24}Fe_2As_2$ and $T_c = 26$ K.

5.3. Results and discussion

At low temperatures, $BaFe_2As_2$ as well as $Ba_{1-x}K_xFe_2As_2$ ($x < 0.3$) undergo a structural phase transition from tetragonal (space group $I4/mmm$) to orthorhombic (space group $Fmmm$). With increasing potassium content, the transition temperature, for $x = 0$ at 135 K, decreases and the size of the orthorhombic distortion is reduced as well[12]. The low temperature single crystal measurements at ID11 revealed a splitting of reflections in agreement with the low temperature $Fmmm$ phase for $x < 0.24$. As an example, the splitting of diffraction spots and twinning observed in a crystal with composition $Ba_{0.845}K_{0.155}Fe_2As_2$ is discussed.

Figure 5.2 shows a section of the hk0 plane at a temperature of 20 K. The orthorhombic distortion at low temperatures causes a splitting of reflections. Because of the minuteness of the orthorhombic distortion, the effect is rather small, but still a splitting of reflections is observed for h, k > 4 and at h, k = 10 separate reflections were recorded. The small spot size demonstrates the high crystal quality. The diffraction pattern indicates multiple twinning: Along a* and b*,
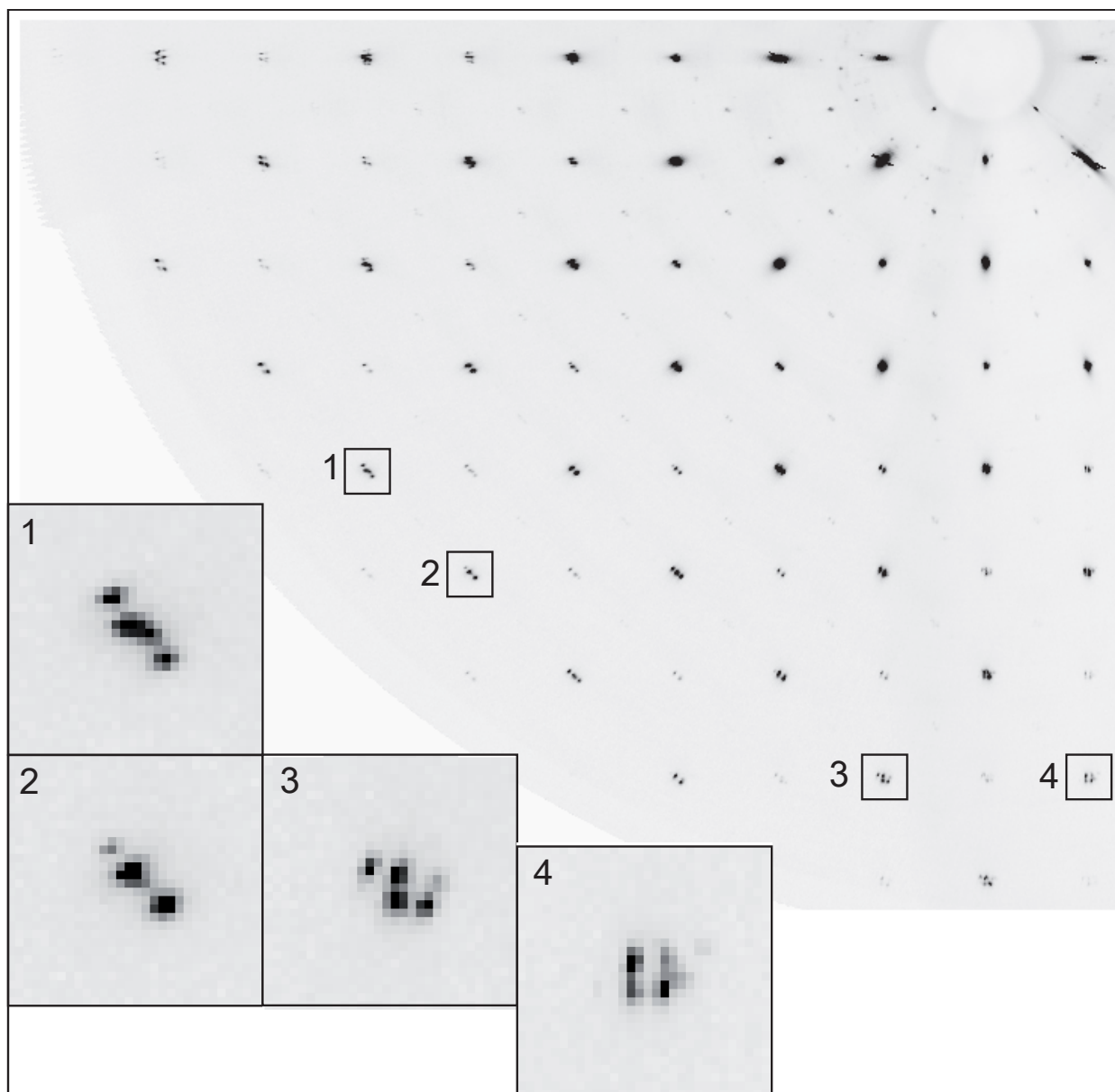
Fig. 5.2.: Section of the hk0 plane of a $Ba_{0.845}K_{0.155}Fe_2As_2$ - crystal at 20 K. The splitting of reflections caused by the orthorhombic distortion is clearly visible. 1-4: enlarged areas of the diffraction pattern showing groups of reflections corresponding to the different twin domains.
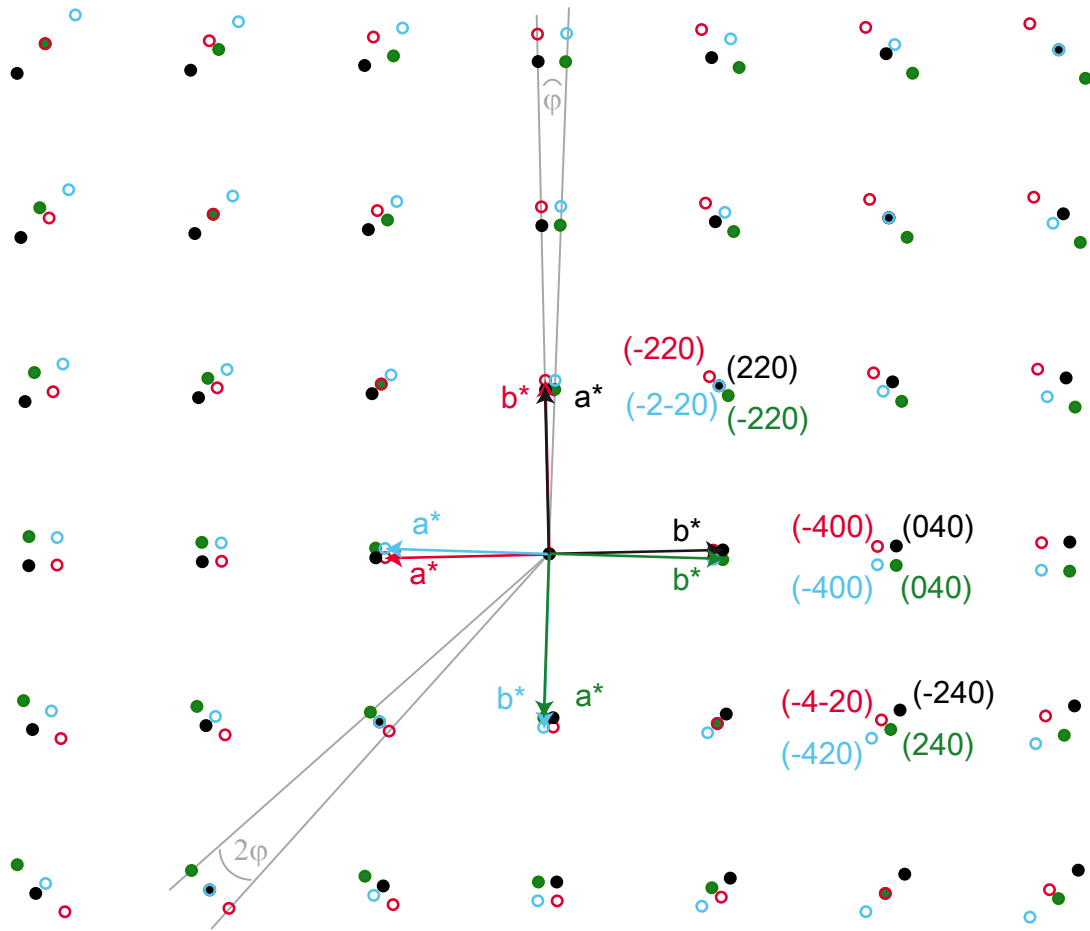
Fig. 5.3.: Schematical diffraction pattern of orthorhombic Ba$_{1-x}$K$_x$Fe$_2$As$_2$ ((hk0) plane). The reciprocal axes of the four twin domains and the corresponding reflections are depicted in red, blue, green and black.

each spot is split into four individual reflections (forming a square as seen in insert 4 of 5.2), along the diagonal however three linearly arranged reflections are visible (Figure 5.2 insert 2). In between, a mixture of both motives is observed (insert 1 and 3). This diffraction pattern can be explained by four twin domains as shown in Figure 5.3 (red, blue, green and black diffraction spots indicate the individual domains, the orthorhombic axes are shown). The occurrence of four twin domains can be explained by the loss of the four-fold rotational symmetry along c* (replaced by a two-fold rotation axis) and the (100)$_T$ mirror plane (no diagonal mirror plane exists in the orthorhombic cell) with the reduction of the

symmetry from tetragonal to orthorhombic. Along the diagonal, the reflections of two domains overlap resulting in the observation of three spots, while all four diffraction spots are visible along a* and b* (Figure 5.3). Although only two twin domains were observed in TEM studies of $BaFe_2As_2$[96], Tanatar et. al. reported four twin domains for $BaFe_2As_2$ at 10 K[89] and a diffraction pattern well in agreement with our data. The twinning described here is also well known from YBCO crystals[97]. So far, the small splitting of the reflections and the limits of the available software for data processing prevented separate indexing and integration of the twin domains.

However, the ratio of the orthorhombic axes, b/a, can be estimated from the splitting of reflections in the hk0 plane shown in Figure 5.2. The splitting angle φ (shown in Figure 5.3) is related to b/a by the formula $\varphi = 90° - 2\arctan(b/a)$ and can be calculated from the distances of the reflections and their distance to the center. For $Ba_{0.82}K_{0.18}Fe_2As_2$ and a temperature of 20 K, this estimation yields $b/a = 0.9935(11)$. This value agrees with the values calculated from the reported lattice parameters of $Ba_{0.9}K_{0.1}Fe_2As_2$ and $Ba_{0.8}K_{0.2}Fe_2As_2$[98] ($b/a = 0.9931$ and 0.9951 at 10 K).

As a first approximation, the split reflections were integrated as one. This integration with a tetragonal unit cell gives $a_T = 394.94$ pm. From this value and the b/a ratio, the orthorhombic unit cell parameters for $Ba_{0.82}K_{0.18}Fe_2As_2$ were calculated. The data was corrected for absorption with sadabs (approximation of the Laue symmetry by use of $2/m$, c unique) and transformed to the orthorhombic cell with XPREP. If the twinning is included in the refinement, the results are improved. During the tetragonal integration, the splitting by the angle φ is negleced and the intensities are added up. With $\varphi = 0$, pairs of domains (black and green, or blue and red in Figure 5.3) differ only by inversion of two axes (for example b* and c*) and are not distinguishable from each other because of the orthorhombic symmetry. Thus two (instead of four) twin domains were used in the refinement. The results are summarized in Table 5.1. The structural data

Table 5.1.: Crystallographic data of Ba$_{0.82}$K$_{0.18}$Fe$_2$As$_2$

Crystal system, space group	Orthorhombic, *Fmmm*, No. 69
a, b, c (pm)	556.4(3), 553.8(3), 1302.74(8)
Cell volume (nm^3)	0.4014(3)
Calculated density (g/cm^3), Z	3.462, 4
Radiation type, λ (Å)	synchrotron, 0.15818
Temperature (K)	20
2θ range	1.21 - 13.16
ratio of Transmission (min/max)	0.4188
Absorption coefficent (mm^{-1})	8.787
Total number of reflections	10031
Independent reflections, R$_{int}$	1234, 0.0347
Reflections with $I > 2\sigma(I)$, R_σ	1234, 0.0216
Refined parameters, Goodness-of-fit on F^2	14, 0.367
R_1, $wR2$ $(I > 2\sigma(I))$	0.0141, 0.0703
Largest residual peak, hole $e^-/$Å^3	2.918, -2.78
twin fraction	0.489(4)
Extinction coefficient	0.07(3)

Atomic parameters:

Ba/K	4a	$(0,0,0)$	U$_{eq}$ = 0.00363(1))
Fe	8f	$(\frac{1}{4},\frac{1}{4},\frac{1}{4})$	U$_{eq}$ = 0.00324(1)
As	8i	$(0,0,z)$, $z = 0.353881(5)$	U$_{eq}$ = 0.00310(1)

Interatomic distances and angles

distance (pm)	Fe-As	238.39(6)
	Fe-Fe	276.90(15)
		278.18(15)
	Ba/K-As	336.02(12)
		337.07(12)
angle (°)	As-Fe-As	110.82(2)
		108.99(3)
		108.61(3)

confirmes the results from low temperature rietveld refinements[98].

For $Ba_{1-x}K_xFe_2As_2$-crystals with $x > 0.24$, the orthorhombic splitting becomes too small to resolve distinct reflections even at high diffraction angles, although a small distortion should still be present at this potassium content[32]. Since no spitting was observed, for $Ba_{0.75}K_{0.25}Fe_2As_2$ and $Ba_{0.76}K_{0.24}Fe_2As_2$ the data was integrated in the tetragonal unit cell. The results are summarized in Figure 5.4. For $x = 0.25$ (blue), a small decrease in both lattice parameters a and c is found above 25 K, while for $x = 0.24$ (black) c shows an increase and a stays almost constant. In sum, the variations of the lattice parameters in the temperature range 10 - 60 K are small. c varies by $\sim$1 pm (0.08 %) and a shows variations of about 0.2 pm (0.05 %) for $x = 0.25$ and 0.1 pm (0.025 %) for $x = 0.24$. This means that the magnitude of possible changes or anomalies around T_c must be smaller than 1 pm in c and smaller than 0.1 - 0.2 pm in a. For both crystals, a and c show two smaller bumps, one at 25 - 30 K and one at 15 - 20 K. Taking into account the temperature offset of -5 K revealed by the calibration, for $Ba_{0.76}K_{0.24}Fe_2As_2$ the first anomaly is close to the transistion temperature of 26 K. However, the data quality does not allow for final conclusions. Figure 5.4(c) shows how z(As) changes with temperature. Again, the observed changes are rather small ($<$0.00008) and follow no consistent trend for both crystals. As expected, the atomic displacement parameters of $Ba_{0.76}K_{0.24}Fe_2As_2$ increase with increasing temperature (Figure 5.4(d)).

For $x \geq 0.3$, the tetragonal to orthorhombic phase transition in $Ba_{1-x}K_xFe_2As_2$ is suppressed and the maximum transition temperature of 38 K is reached for $x = 0.4$. The structural data for a crystal of composition $Ba_{0.57}K_{0.43}Fe_2As_2$ in the temperature range 14 - 55 K is summarized in Figure 5.5. Some outliers are observed, probably due to unstable conditions during measurements (concerning for example the helium flow). In the investigated temperature range, the lattice parameters a and c (Figure 5.5(a)) show almost no changes, only for a a slight decrease with decreasing temperature is observed. In total, a changes by no more

(a)

(b)

(c)

(d)
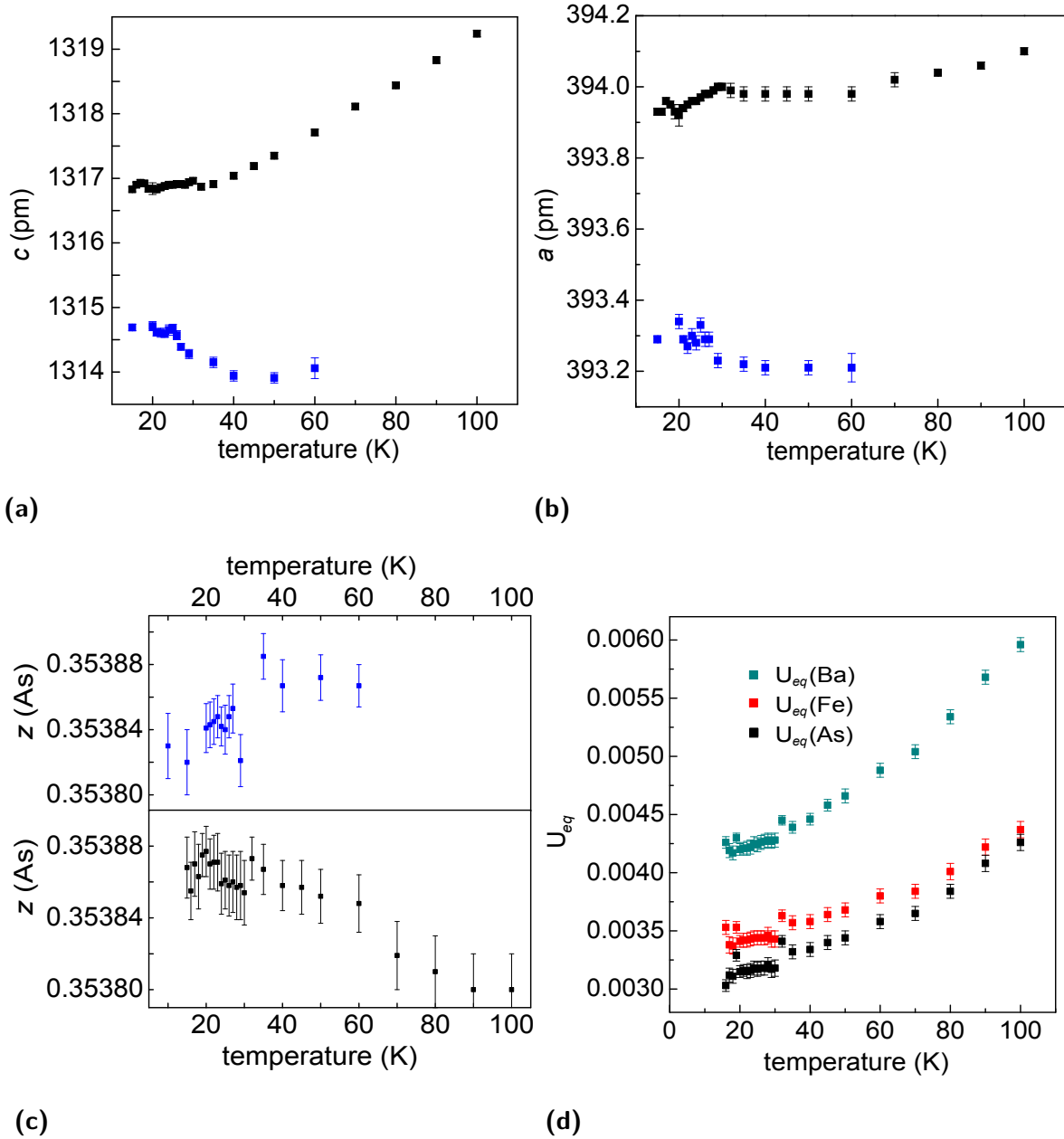
Fig. 5.4.: $Ba_{0.75}K_{0.25}Fe_2As_2$ (blue) and $Ba_{0.76}K_{0.24}Fe_2As_2$ ($T_c = 26$ K, black): top: variation of the lattice parameters c (a) and a (b) in the temperature range 10 - 60 K / 10 - 100 K. (c): temperature dependence of the positional parameter z(As). (c): Change of the atomic displacement parameters of $Ba_{0.76}K_{0.24}Fe_2As_2$ in the temperature range 15 - 100 K, U_{eq}(Ba/K): cyan, U_{eq}(Fe): red and U_{eq}(As): black.
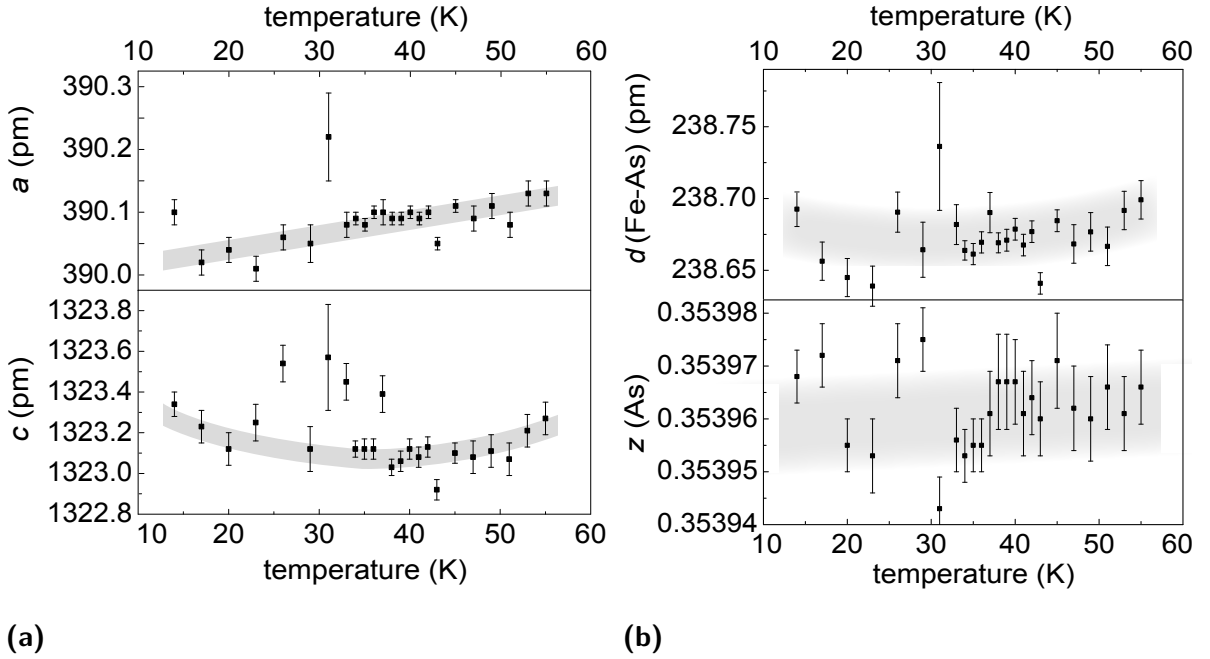
Fig. 5.5.: $Ba_{0.57}K_{0.43}Fe_2As_2$: (a) lattice parameters a (top) and c (bottom) and their variation in the temperature range 14 - 55K. (b) Variation of the FeAs distance d (top) and $z(As)$ (bottom).

than 0.1 pm (0.026 %) and c by no more than 0.6 pm (0.045 %). Similar observations are made for $z(As)$ and the Fe-As distance (Figure 5.5(b)). $z(As)$ varies by less than 0.00004 and the Fe-As distance by no more than 0.05 pm (0.02 %). No convincing trends or anomalies near T_c are observed. Thus it can be concluded that if structural anomalies exist near T_c for optimally doped $Ba_{1-x}K_xFe_2As_2$, they are very small and probably not accessible within the resolution of X-ray diffraction experiments.

To summarize, small high quality single crystals of $Ba_{1-x}K_xFe_2As_2$ ($x = 0$ - 0.43) were prepared and studied with low temperature single crystal diffraction at ID11, ESRF Grenoble. For $x < 0.24$, a splitting of reflections in agreement with the low temperature orthorhombic phase is found. Although the orthorhombic distortion and thus the splitting is minute, separate reflections are observed at h, k = 10 for $Ba_{0.845}K_{0.155}Fe_2As_2$. A closer inspection of the diffraction pattern reveals four twin domains (in agreement with literature[89]) caused by the loss of

the four-fold rotational symmetry and the $(100)_T$ mirror plane.

From the splitting angle φ the b/a ratio is estimated to be 0.9935(11) for a crystal with the composition Ba$_{0.82}$K$_{0.18}$Fe$_2$As$_2$. This allows an estimation of the orthorhombic cell parameters and - in combination with a joined integration of the split reflections - a complete structure refinement. The results of this first single crystal refinement of the low temperature *Fmmm* phase agree well with results from powder data[98].

For $x \sim 0.24$ and 0.25, no separate reflections are resolved. Analysis with a tetragonal treatment of the data show hardly any changes of the structural parameters from 10 to 60 K. Smaller anomalies of the lattice parameters might exist around 25 - 30 K, but the data quality does not permit any definite conclusions. For Ba$_{0.57}$K$_{0.43}$Fe$_2$As$_2$, where the phase transition is suppressed, the structural parameters vary by less than 0.05 % in the temperature range 14 - 55 K. No distinct anomalies or changes of structural parameters around T_c are observed.

6. Local structural studies of Ba$_{1-x}$K$_x$Fe$_2$As$_2$ using atomic pair distribution function

6.1. Introduction

It is highly desirable to better understand mutual relationships of structure and superconductivity in the iron pnictides. To investigate possible correlations between structure and properties, however, detailed structural information is necessary. In this context, the role of the local structure, that can deviate considerably from the averaged structure obtained by x-ray diffraction, should not be negleced. One way to get information about the local structure is the analysis of the atomic pair distribution function (PDF), the PDF being a measure of the probability of finding two atoms separated by a distance r(Å) in real space. Up to now, few PDF studies on iron-based superconductors have been carried out, but those with interesting results. PDF studies on SmFeAsO$_{1-x}$F$_x$ indicate that the local structure differs significantly from the average structure and is better described with lower symmetry; especially the arsenic atoms tend to be shifted from the positions defined by space group symmetry of the average structure[99]. In FeSe$_{1-x}$Te$_x$, a

PDF study first revealed that the selenium and tellurium atoms have different z-coordinates because the Fe-Se bond is shorter than the Fe-Te bond[100], a fact later confirmed by single crystal data[101]. This shows the importance of closer investigations of the local structure of the iron-based superconductors. Here, a study of the local structure of Ba$_{1-x}$K$_x$Fe$_2$As$_2$ is presented.

6.2. Experimental Methods

BaFe$_2$As$_2$ was synthesized by heating stoichiometric mixtures of the elements in a glassy carbon crucible to 1373 K at a rate of 50 K/h, keeping this temperature for 5 h, cooling slowly to 1123 K (5 K/h) and quickly to room temperature. Polycrystalline Ba$_{1-x}$K$_x$Fe$_2$As$_2$ samples were prepared as described in[12]. The finely ground samples were packed in 0.6 mm quartz capillaries. Total scattering x-ray measurements were carried out at the beamline ID 31 of the European synchrotron radiation facility, Grenoble at the temperatures 297 K and at 5 K with $\lambda = 0.4008$ Å in the 2θ-range 0 - 110°. Data of an empty capillary was also collected. For rietveld refinements, only the data range 0 - 30° 2θ was used. The refinements were performed with the Topas suite of programs[74] and a full Voigt function was used to describe the peak shape (appendix A.3). The corrected total scattering structure function, S(Q) was obtained using the standard corrections[102] utilizing the PDFgetX2 program. From the S(Q), the PDF data G(r) was obtained by the Fourier transformation according to G(r) = 2/π ∫ Q[S(Q) − 1]sin(Qr) dQ, where Q is the magnitude of the scattering vector. Modeling of the PDF data was carried out using the PDFgui and PDFfit2 packages[103].

(a)   **(b)**
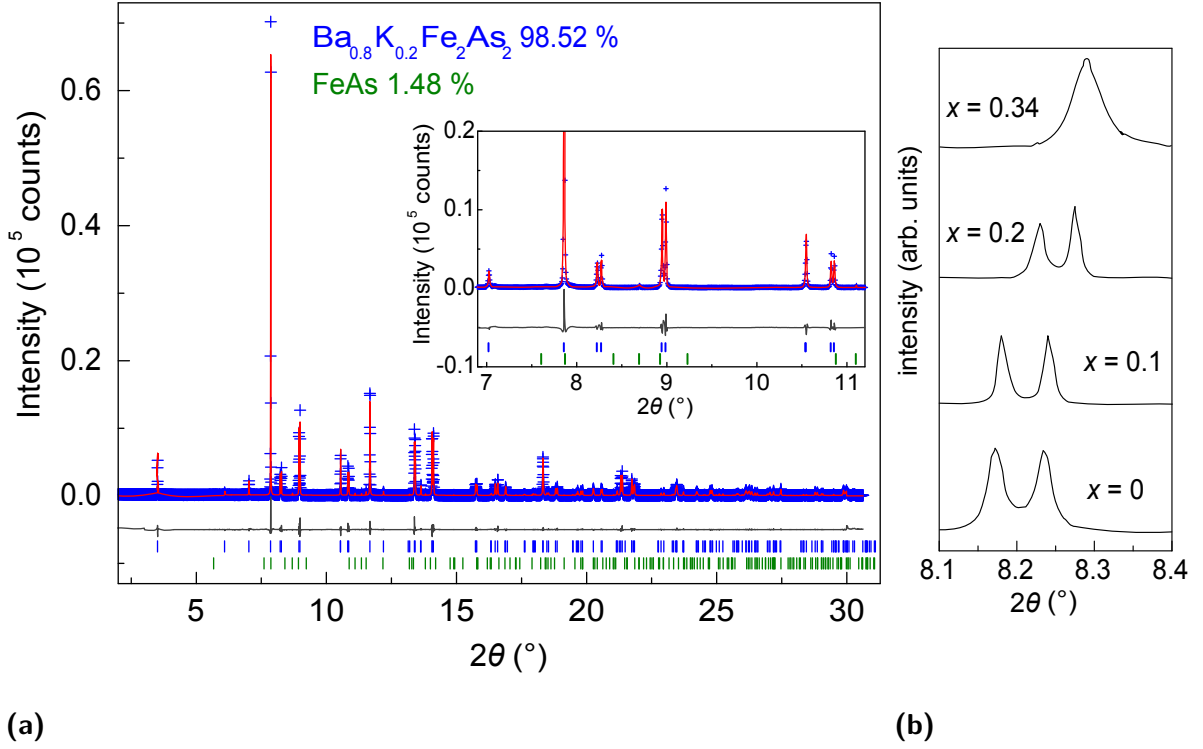
Fig. 6.1.: (a) X-ray pattern of $Ba_{0.8}K_{0.2}Fe_2As_2$ collected at 5 K (blue), rietveld fit (red) and difference curve (gray). Insert: Section of the plot, the small linewidth and the splitting of reflections are visible. (b) Splitting of the (110) reflection at 5 K for $x = 0 - 0.34$.

6.3. Results and Discussion

All x-ray patterns could be refined in the tetragonal space group $I4/mmm$ at room temperature and in the orthorhombic space group $Fmmm$ ($x = 0$ - 0.2) or tetragonal $I4/mmm$ ($x = 0.34$) at low temperature in agreement with literature[12]. Figure 6.1(a) presents the diffraction pattern and rietveld refinement of $Ba_{0.8}K_{0.2}Fe_2As_2$ at 5 K. The diffraction pattern shows very sharp reflections, which is a sign for good homogenity of the sample. A variation of the potassium content would change the unit cell dimensions, which would lead to a distribution of the values of a and c for an inhomogeneous sample, causing a broadening of the reflections. In Figure 6.1(b), the (110) reflection at 5 K is shown for $x = 0$ - 0.34, note the sharpness of the peaks for all compositions. The synchrotron
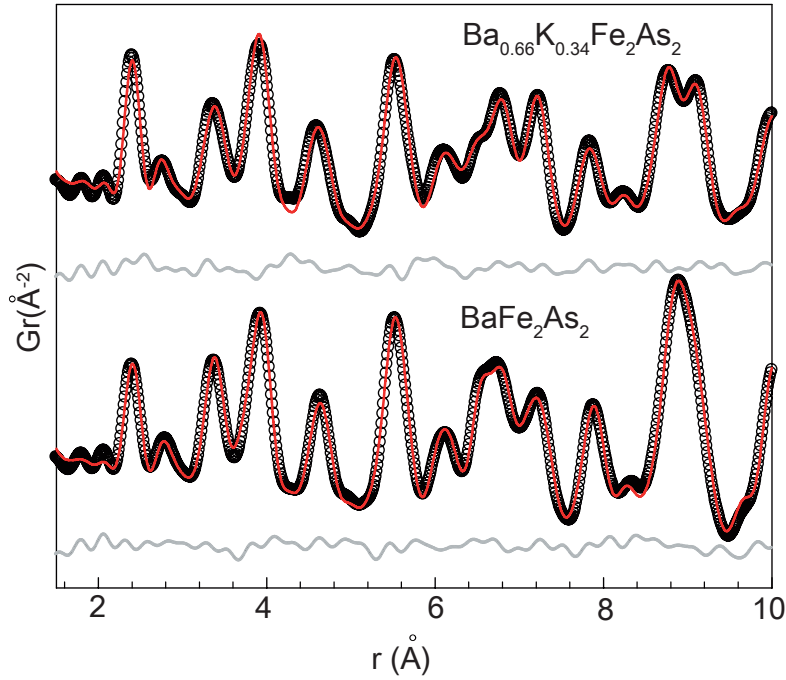
Fig. 6.2.: PDF data at room temperature and refinement results of $BaFe_2As_2$ and $Ba_{0.66}K_{0.34}Fe_2As_2$.[104]

radiation permits us to observe distinctly splitted relections for $x = 0.2$ (insert Figure 6.1(a) and Figure 6.1(b)), where only a broadening is observed with a lab diffractometer.

The rietveld refinement results were used as starting parameters for the PDF analysis of the data performed by B. Joseph from the group of L. Malavasi at the University of Pavia. PDF data at room temperature and the refinement results for $BaFe_2As_2$ and $Ba_{0.66}K_{0.34}Fe_2As_2$ are depicted in Figure 6.2. Although the PDF data is rather similar for both samples, some differences, like the splitting of the peak around 9 Å in the spectra of the hole doped sample are observed. It is found that the average structure from diffraction results gives a reasonable fit of the PDF data, which means that no significant structural deviations exist on the local scale. However, for a good description of the local structure, anisotropic thermal factors are necessary, where $U_{33} > U_{11} = U_{22}$ is found for the barium and iron atoms.

To summarize, high quality x-ray data of $Ba_{1-x}K_xFe_2As_2$ (x=0 - 0.34) with small reflection line widths could be collected at ID 31 (ESRF). PDF analysis of the data shows no significant structure deviations on the local scale.

7. $K(Fe_{1-y}Co_y)_2As_2$

7.1. Introduction

Since the discovery of superconductivity in hole doped $BaFe_2As_2$, KFe_2As_2 as the endpoint of the series $Ba_{1-x}K_xFe_2As_2$ attracted much research interest. Known since 1981[105], KFe_2As_2 was now found to be a superconductor with $T_c \approx 3$ K[9] and rather unconventional properties. Recent results point towards a nodal superconducting gap[106,107], and although no interband nesting is observed, nuclear magnetic resonance measurements as well as neutron scattering indicate the existance of incommensurate spin fluctuations[108,109], suggesting that magnetism plays some role for the superconductivity. Furthermore, a large Sommerfeld constant hints at strong electron correlation in KFe_2As_2[109].

Potassium carries one electron less than barium, making KFe_2As_2 "extremely hole doped" in comparison to $BaFe_2As_2$. This hole doping could - in theory - be compensated by the introduction of electrons, for example by exchanging iron subsequently by cobalt in a mixed crystal series $K(Fe_{1-y}Co_y)_2As_2$. The same valence count as in $BaFe_2As_2$ would be achieved for $y = 0.5$, that is in $KFeCoAs_2$. Density functional calculations on $KFeCoAs_2$ using the virtual crystal approximation show that indeed both the density of states (Figure 7.1(a)) and the Fermi surface (Figure 7.1(b), upper row, right) are very similar to $BaFe_2As_2$[110]. However, $KFeCoAs_2$ seems to have less tendency towards magnetism than $BaFe_2As_2$.

Figure 7.1(b) shows how the Fermi surface is assumed to change with varying y in $K(Fe_{1-y}Co_y)_2As_2$. On the "hole doped" side, disconnected hole and electron Fermi surface cylinders exist for $0 \leq y \leq 0.5$, but the hole type sheet around Γ
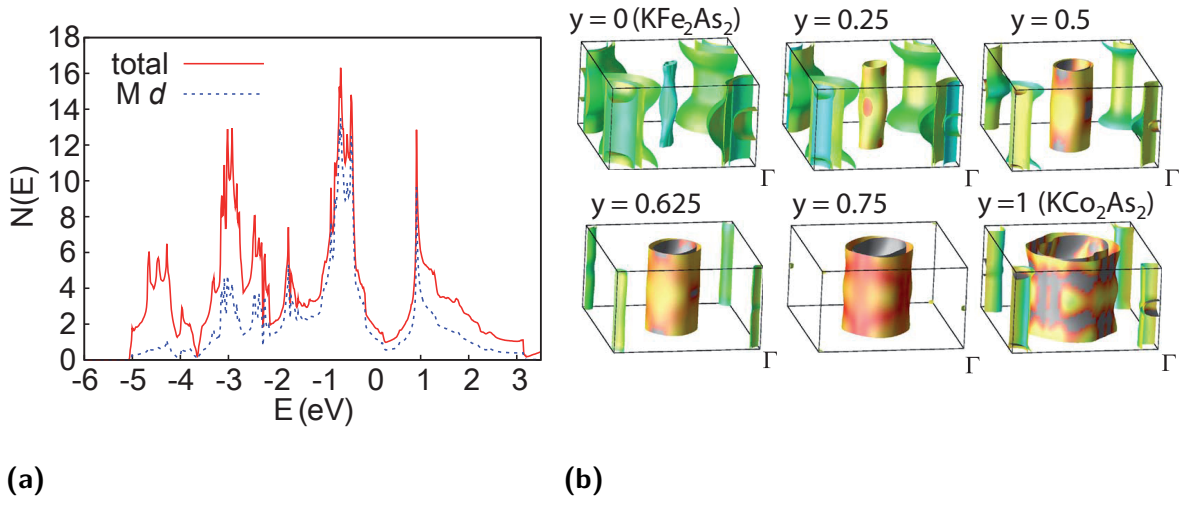
Fig. 7.1.: (a) Calculated density of states for KFeCoAs$_2$ obtained with the virtual crystal approximation. (b) Calculated Fermi surface of K(Fe$_{1-y}$Co$_y$)$_2$As$_2$ for various values of y. Both figures taken from Ref.[110].

vanishes rather quickly for $y > 0.625$ on the "electron doped" side. Close to $y = 0.5$, nesting of hole and electron Fermi surface sheets is observed, which places the material near a spin density wave instability and makes K(Fe$_{1-y}$Co$_y$)$_2$As$_2$ a possible candidate for superconductivity.

Since both KFe$_2$As$_2$ and KCo$_2$As$_2$ exist (KCo$_2$As$_2$ was reported in literature[105], but the properties of the compound were not investigated so far) and crystallize in the same structure type, the ThCr$_2$Si$_2$-type structure, it should be possible to synthesize K(Fe$_{1-y}$Co$_y$)$_2$As$_2$ and check wether the similarities to BaFe$_2$As$_2$ suffice to enable superconductivity in these compounds.

7.2. Experimental Methods

It is difficult to obtain homogenous samples of K(Fe$_{1-y}$Co$_y$)$_2$As$_2$ by direct synthesis starting from the elements. Therefore, the mixed iron-cobalt arsenide Fe$_{1-y}$Co$_y$As was prepared as starting material. Stoichiometric mixtures of iron,

cobalt and arsenic were sealed in silica ampoules, heated to 1013 K for 10 h, homogenized and annealed at least twice at 1163 K. EDX measurements on several samples show that this yields rather homogenous samples. Potassium was added, the sample placed in an alumina crucible, and heated to 813 K for 15 h. Fine, gray metallic powders, sensitive to air, were obtained as reaction products. For some samples, a small quantity of the mixed iron-cobalt arsenide remained as impurity phase. Resistivity was measured using the four probe method in the temperature range 10 K - 320 K on polycrystallinic samples that had been cold-pressed to pellets and annealed at 773 K. Powder diffraction data was measured using a Huber G670 diffractometer (Cu-Kα_1-radiation) with guinier geometry and for rietveld refinements the TOPAS package[74]was used. Magnetic properties were determined utilizing a SQUID magnetometer (MPMS-XL Quantum Design Inc.).
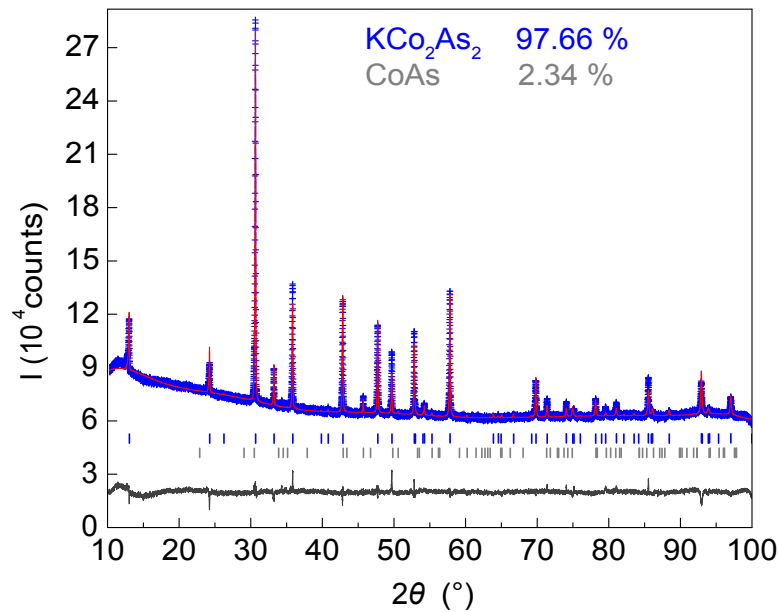
Fig. 7.2.: X-ray powder pattern (blue), Rietveld fit (red) and difference curve of KCo$_2$As$_2$.

(a)   **(b)**
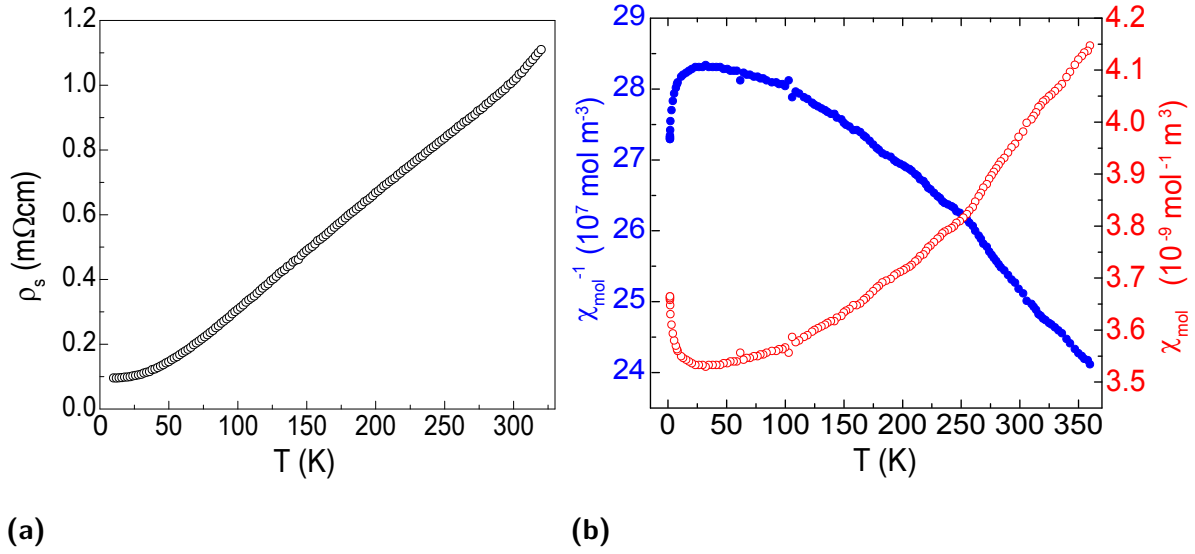
Fig. 7.3.: (a) Electrical resistances ρ_s of KCo$_2$As$_2$. (b) Molar susceptibility χ_{mol} (red, open symbols) and inverse molar susceptibility (blue, filled symbols) of KCo$_2$As$_2$.

7.3. Results and Discussion

First, the properties of KCo$_2$As$_2$ were investigated. Powder pattern and rietveld fit of KCo$_2$As$_2$ are displayed in Figure 7.2. The electrical resistance, molar susceptibility and inverse molar susceptibility are shown in Figure 7.3. The resistance of KCo$_2$As$_2$ (Figure 7.3(a)) decreases linearly at higher temperature and shows some saturation at low temperatures, as it is typical for a normal metal, no anomalies are observed. For the susceptibility, values typical for a Pauli paramagnetic metal and only a very small variation with temperature (3.5-4.15 $\cdot$ 10^{-9} mol^{-1} m^3) are observed (Figure 7.3(b)). Low temperature powder diffraction gives no indication of a phase transition at low temperatures. To summarize, KCo$_2$As$_2$ is non superconducting above 1.8 K, has the properties of a metal and shows no anomalies or phase transitions at low temperatures.

Figure 7.4(a) shows the influence of Co substitution on the structural parameters in K(Fe$_{1-y}$Co$_y$)$_2$As$_2$. With increasing cobalt content y, both a (Figure 7.4(a), top left) and c (Figure 7.4(a), bottom left) undergo a more or less linear decrease.

In total, a decreases by 1% and c by 2 %. Also, the z coordinate of arsenic shows a trend to smaller values. All the above mentioned structural changes result in an increase of the value of the As-Fe-As bond angle ε from $\sim 107°$ to $\sim 110.5°$, a value close to the ideal tetrahedral angle of $109.47°$ occuring for $y \approx 0.6$. Due to the decrease of the lattice parameter a, the Fe-Fe distances decrease from 272 pm in KFe_2As_2 to 269 pm in KCo_2As_2 (for comparison: in $BaFe_2As_2$ the Fe-Fe distance is 277 pm). Compared to $BaFe_2As_2$ with $a = 396$ pm and $c = 1302$ pm, the unit cell in $K(Fe_{1-y}Co_y)_2As_2$ is stretched along c and shortened along a.

The electrical resistance was measured to check for superconductivity or possible spin density anomalies expected due to the fermi surface nesting in $K(Fe_{1-y}Co_y)_2As_2$ around $y = 0.5$. The results are depicted in Figure 7.5 (a) ($0 \leq y \leq 0.5$) and (b) ($0.5 \leq y \leq 1$). Unlike doped $BaFe_2As_2$, $K(Fe_{1-y}Co_y)_2As_2$ shows no superconductivity above 10 K (the superconducting transition of KFe_2As_2 at 3 K is not visible here). Contrary to $BaFe_2As_2$, no SDW-type anomaly is observed for $y = 0.5$. This result is however in agreement with the calculations, where, despite the Fermi surface nesting in $KFeCoAs_2$, no SDW ground state was found[110].

For KFe_2As_2, the resistivity versus temperature curve shows a convex shape at higher temperatures and a T^2 dependence at low temperatures (Figure 7.5(a) and 7.6, light green) as described in literature[111]. With increasing cobalt content of the samples the convex shape becomes less pronounced and the negative curvature disappears between $y = 0.2$ and $y = 0.4$. For higher cobalt concentrations, the resistivity shows a linear temperature dependence above ~ 70 K, like it is observed in KCo_2As_2. For low temperatures (10 K - 50 K), all samples show the T^2 dependence reported for KFe_2As_2 (Figure 7.6), indicating fermi liquid behaviour. Only on the Co rich side, small deviations at low temperature are found. If we take a look at the residual resistivity ratio RRR, the ratio of resistance at 300 K and at 10 K (RRR $= \rho_{300K}/ \rho_{10K}$) we find a value of 38 for KFe_2As_2, that decreases to $1.6 - 1.4$ for $y = 0.5 - 0.7$ and then increases again to 10 for
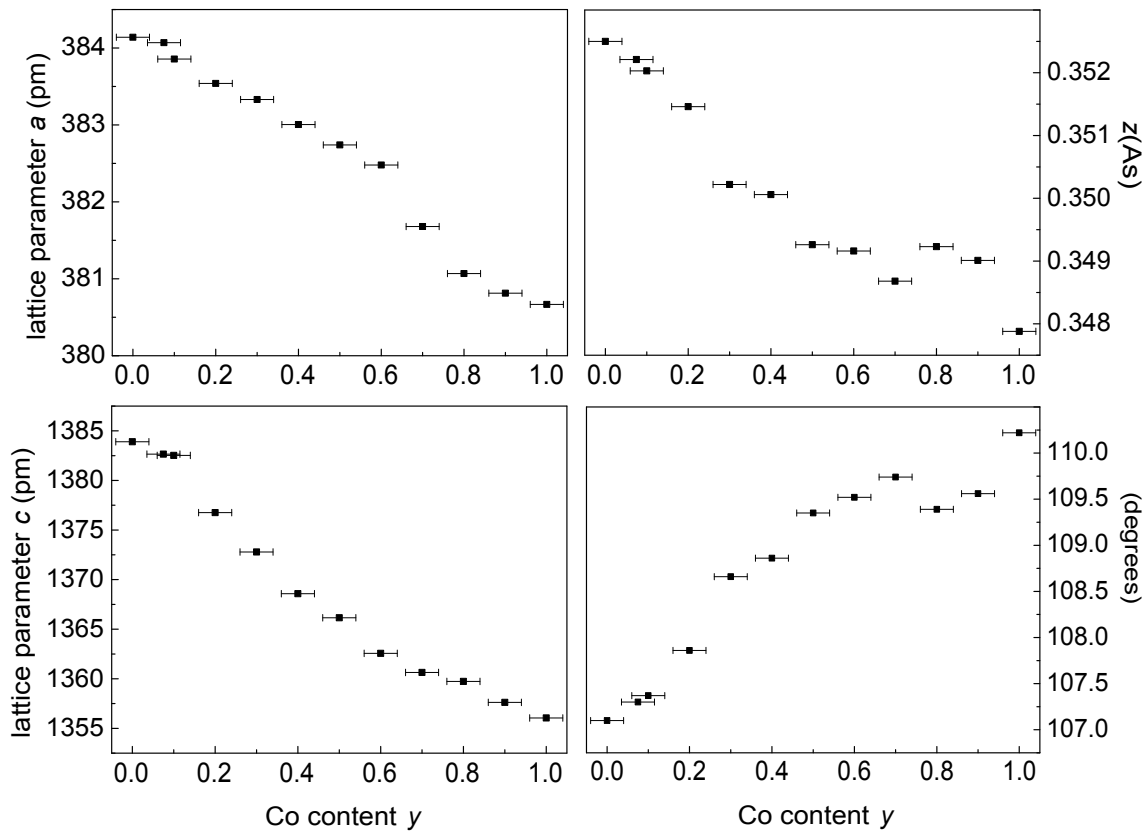
(a)
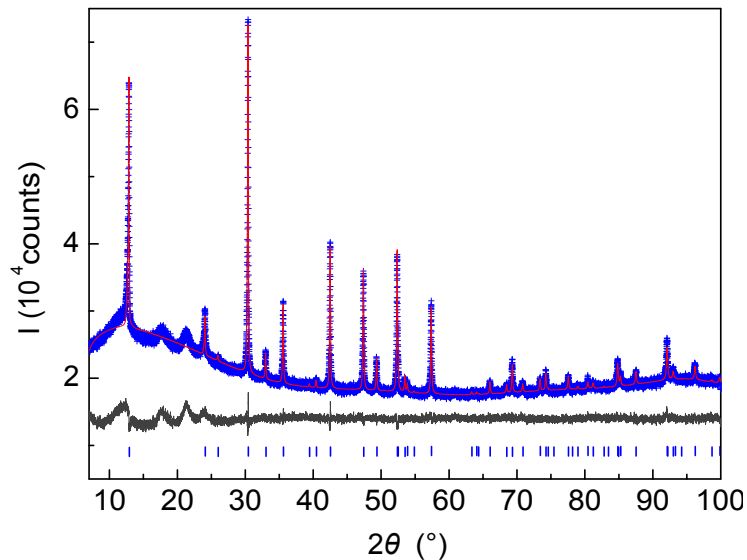
(b)

Fig. 7.4.: (a) Variation of structural parameters in $K(Fe_{1-y}Co_y)_2As_2$: lattice parameter a (top left), lattice parameter c (bottom left), z coordinate of arsenic (top right) and As-Fe-As angle ε (bottom right). (b) X-ray powder pattern (blue), Rietveld fit (red) and difference curve of $K(Fe_{0.6}Co_{0.4})_2As_2$.
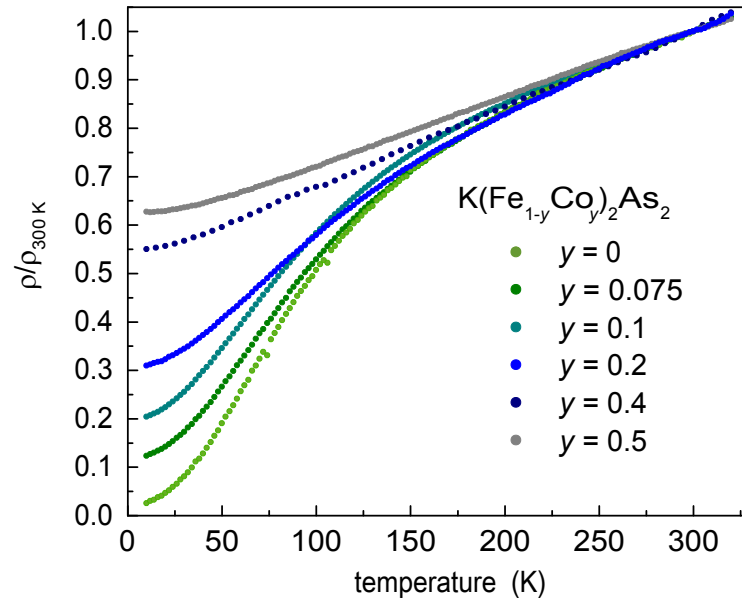
(a)
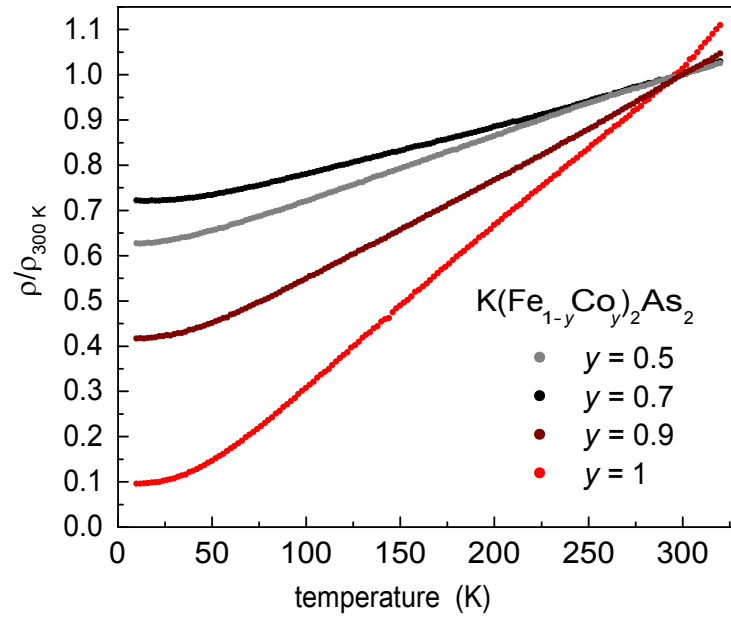
(b)

Fig. 7.5.: Normalized electrical resistances ρ/ρ_{300K} of K(Fe$_{1-y}$Co$_y$)$_2$As$_2$ for $0 \leq y \leq 0.5$ (a) (green- gray) and $0.5 \leq y \leq 1$ (b) (gray- red).
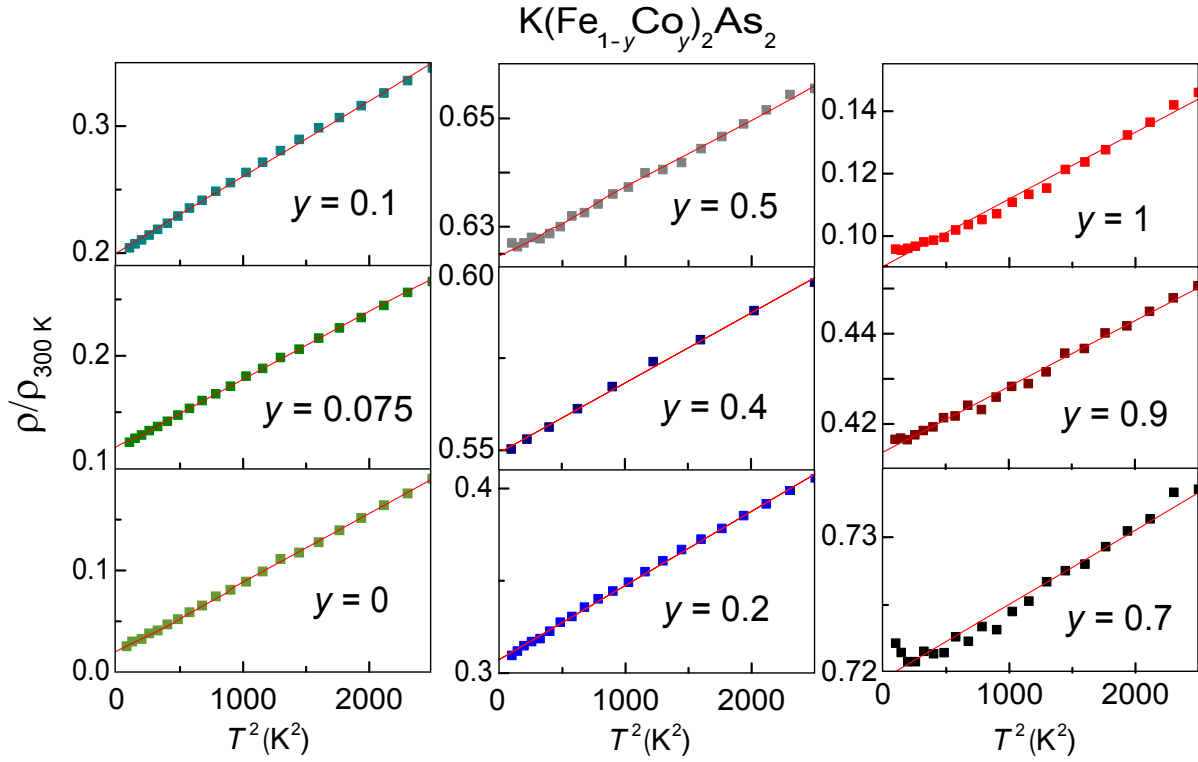
Fig. 7.6.: T^2-behaviour of K(Fe$_{1-y}$Co$_y$)$_2$As$_2$ at low temperatures: Normalized electrical resistances ρ/ρ_{300K} versus T^2 (K^2) for 10-50 K.

KCo$_2$As$_2$. For single crystals the residual resistivity ratio is used as an indicator of crystal purity, as it drops in the presence of impurity scattering. The decrease of this ratio in the mixed compounds could indicate disorder induced scattering, although the quality of the pills pressed from the polycrystallinic samples might vary and influence the values.

Magnetic measurements on K(Fe$_{0.4}$Co$_{0.6}$)$_2$As$_2$ show no superconductivity above 1.8 K; susceptibility values in the range 0.59-0.67· 10^{-6} mol^{-1} m^3 and a close to paramagnetic curve shape were found, but an exact determination of the magnetic properties was hampered by ferromagnetic impurities.

To summarize, polycrystallinic samples of K(Fe$_{1-y}$Co$_y$)$_2$As$_2$ can be synthesized using the mixed iron cobalt arsenide as starting material. Structural investigations show that although the unit cell proportions are different than in BaFe$_2$As$_2$ (the unit cell is elongated along *c* and compressed along *a*), a value close to the

ideal tetrahedra angle (discussed to be an important parameter for the occurrence of hight T_c's in the iron arsenide superconductors) is reached for $y = 0.6$. Despite similarities to $BaFe_2As_2$, like identical valence count and similar Fermi surface, $KFeCoAs_2$ ($y = 0.5$) shows no indication of a spin density anomaly like in $BaFe_2As_2$. Consistently, no anomalies or high temperature superconductivity are observed for $K(Fe_{1-y}Co_y)_2As_2$ for the whole substitution range $y = 0 - 1$. Giving no evidence of superconductivity above 10 K, resistivity versus temperature plots of $K(Fe_{1-y}Co_y)_2As_2$ show a decrease of the convex curvature observed in KFe_2As_2, until linear behaviour is found for $y > 0.4$. The absence of high temperature superconductivity in $K(Fe_{1-y}Co_y)_2As_2$ could be linked to lacking magnetic interactions, since both experiments and theory indicate a close connection between magnetism and superconductivity in the iron-based superconductors. Experiments show the existance of AFM spin fluctuations in the iron pnictides[51] and theoretical studies suggest that these spin fluctuations (appearing in proximity to a quantum critical point) are important for uperconductivity[112]. Inelastic neutron scattering revealed magnetic excitations with a particular wavevector Q_m in all cases investigated[112,113]. Also, a spin resonance appearing below T_c is observed. Especially the latter suggests a "direct interplay between magnetism and superconductivity"[113] in the iron-based superconductors. In $K(Fe_{1-y}Co_y)_2As_2$, the antiferromagnetism frequently observed in iron pnictide superconductors and their parent compounds, is absent. While incommensurate spin fluctuations are discussed for KFe_2As_2[109], KCo_2As_2 shows Pauli-paramagnetic behaviour and for the mixed compounds, no indications for spin density wave anomalies and/or antiferromagnetic transitions are found. This is in agreement with the calculations, where no SDW ground state was found for $KFeCoAs_2$[110]. The reason for the weakening of magnetism could be the reduction of the lattice parameter a and the Fe-Fe distance leading to a reduction of the density of states at the Fermi level in $KFeCoAs_2$ compared to $BaFe_2As_2$[110]. Another possible reason for the absence of magnetism in $KFeCoAs_2$ could be the Co/Fe disorder in the mixed

compounds.

All in all, the absence of high temperature superconductivity in $K(Fe_{1-y}Co_y)_2As_2$ is likely due to lacking magnetic interactions and emphasizes the importance of magnetism for superconductivity in the iron arsenides.

8. Recovery of a parent-like state in $\mathbf{Ba_{1-x}K_x(Fe_{1-y}Co_y)_2As_2}$

8.1. Introduction

The case of $K(Fe_{1-y}Co_y)_2As_2$ shows that it is not possible to compensate the holes in "extremely hole doped" KFe_2As_2 by introducing electrons into the $FeAs_{4/4}$-layer and obtain a material with similar properties as $BaFe_2As_2$, at least not with the substitution of Fe by Co. However, this raises the question what effects electron plus hole doping have at low doping levels. Both hole-doping - by substitution of potassium for barium[9,12] - and electron-doping - by substitution of cobalt for iron[20] - induce superconductivity in $BaFe_2As_2$. The phase diagrams of $Ba_{1-x}K_xFe_2As_2$ and $Ba(Fe_{1-y}Co_y)_2As_2$ are plotted in Figure 8.1 against the charge Δe^- introduced into the $FeAs_{4/4}$-layer by electron or hole doping. With hole-doping, the onset of superconductivity is at about -0.05 e^-/FeAs and the highest T_c is 38 K at -0.2 e^-/FeAs, while by electron-doping the onset is at $+0.03$ e^- and the highest T_c is 25 K at $+0.07$ e^-/FeAs. Furthermore, the superconducting dome spans 0.45 e^- by hole-doping but only 0.11 e^- in the case of electron-doping.
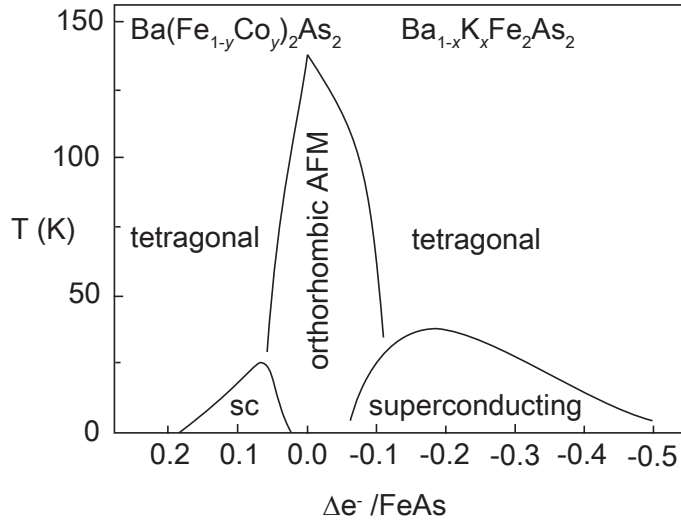
Fig. 8.1.: Phase diagrams of hole- and electron-doped $BaFe_2As_2$. Data from Refs.[108] and[12]. AFM = antiferromagnetic metal, sc = superconducting

This asymmetry may indicate that excess positive or negative charges act differently on the electronic system of $BaFe_2As_2$, but the true relationships are not clear. A DFT study of the Co-doped system suggests the extra electron to remain located at the cobalt atom, the latter acting as scattering centre only[114]. This contradicts to the fact that nickel-doping gives the same phase diagram at half of the concentration. Recent photoemission results are also indicative for filling of rigid bands by doping[115]. However, the direct comparison of electron- and hole-doping is flawed by the fact, that cobalt-substitution adds disorder into the FeAs plane where superconductivity emerges, while the layers remain clean by hole-doping with potassium at the barium-site. Unfortunately, substitutions with electron-poorer 3d-metals (Mn, Cr) do not induce superconductivity[18]. Electron-doping was also achieved in $Sr_{1-x}La_xFe_2As_2$ giving critical temperatures up to 22 K[116], but the sample quality still allows no clear relation between the La-concentration and T_c.

In order to shed more light on the effect of charge modifications in the $(FeAs)^{\delta-}$-layers of $BaFe_2As_2$, the solid solution $Ba_{1-x}K_xFe_{1.86}Co_{0.14}As_2$ was studied. Thus

we gradually compensate the optimal electron doping in $BaFe_{1.86}Co_{0.14}As_2$ by holes created from additional potassium substitution. The effects on the crystal structure, superconductivity and magnetism are determined and discussed.

8.2. Experimental Methods

$Ba_{1-x}K_xFe_{1.86}Co_{0.14}As_2$ samples were prepared from stoichiometric mixtures of Ba, K and $Fe_{0.93}Co_{0.07}As$ in alumina crucibles, sealed in silica tubes and heated to 913 K. The samples were homogenized as far as possible (Ba doesn't react at this temperature, but this first step prevents the sample from getting stuck in the crucible), annealed at 983 K for 10 h, homogenized to a fine powder and annealed at 1063 K two times for 10 h (annealing at lower temperatures gave Fe_2As as impurity phase). $KFe_{1.86}Co_{0.14}As_2$ was synthesised by heating K and $Fe_{0.93}Co_{0.07}As$ to 773 K for 15 h. Resistivities were measured with cold pressed and annealed pellets (at 773 K for $KFe_{1.86}Co_{0.14}As_2$ and 873 K for all other samples) using the four probe method. Bulk superconductivity was confirmed by AC susceptibility measurements. Room temperature powder diffraction data were measured using a Huber G670 diffractometer (Cu-Kα_1 -radiation) and low temperature powder diffraction data using a Huber G670 diffractometer (Co-Kα_1) with guinier geometry, equipped with a closed cycle He-cryostat. At low temperatures, the reflections show a zero shift of 0.4 2θ due to justage. Rietveld refinements were performed with the TOPAS package using the fundamental parameter approach and an empirical 2θ-dependent intensity correction for Guinier geometry. The Fe:Co ratio was held constant and the Ba:K ratios refined. The results agree well with EDX measurements that show variations of the potassium content by no more than $\pm$ 4 % and variations of the Co content by no more than $\pm$ 1 % (results listed in appendix A.4). For some samples small amounts of the mixed cobalt-iron arsenide were observed as side phase. [57]Fe-Mößbauer spectra of $Ba_{0.8}K_{0.2}Fe_{1.86}Co_{0.14}As_2$ were recorded in transmission geometry using

(a)   **(b)**
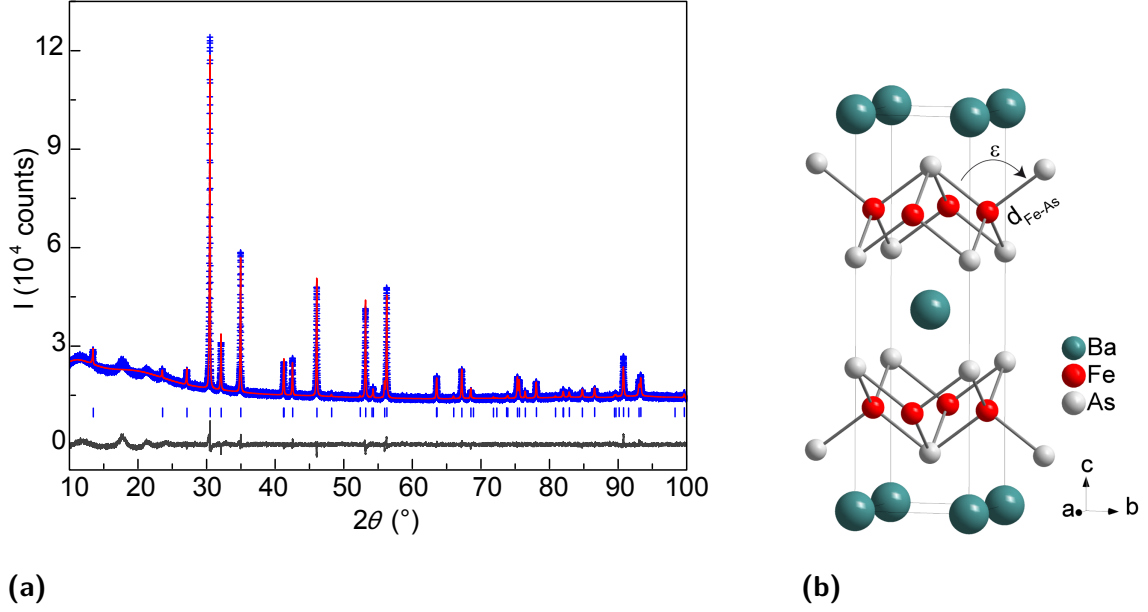
Fig. 8.2.: (a) X-ray powder pattern (top, blue), Rietveld fit (top, red) and difference curve (bottom, gray) of $Ba_{1-x}K_x(Fe_{1-y}Co_y)_2As_2$ with $x = 0.2$. (b) Crystal structure with Fe-As bond length d_{Fe-As} and bond angle ε.

a ^{57}Co/Rh source. The spectrometer was calibrated with a 8μm thin α-Fe foil.

8.3. Results and Discussion

Phase homogeneity and crystal structure parameters were determined by Rietveld refinements of X-ray powder patters. A typical example is shown in Figure 8.2(a). The structure is completely described by the lattice parameters and the z-coordinate of arsenic at the $4e$-site that determines the Fe-As bond length (d_{Fe-As}) and the As-Fe-As bond angle ε (Figure 8.2(b)). As can be seen in Figure 8.3(a), the lattice parameters a and c in $Ba_{1-x}K_xFe_{1.86}Co_{0.14}As_2$ (red) vary linearly with the potassium concentration, very similar to the cobalt-free $Ba_{1-x}K_xFe_2As_2$ (blue). In comparison to $Ba_{1-x}K_xFe_2As_2$, the c-axis in $Ba_{1-x}K_xFe_{1.86}Co_{0.14}As_2$ is slightly reduced (~ 0.7 %).

Figure 8.3(b) shows the normalized changes of the structure parameters against

(a)   **(b)**
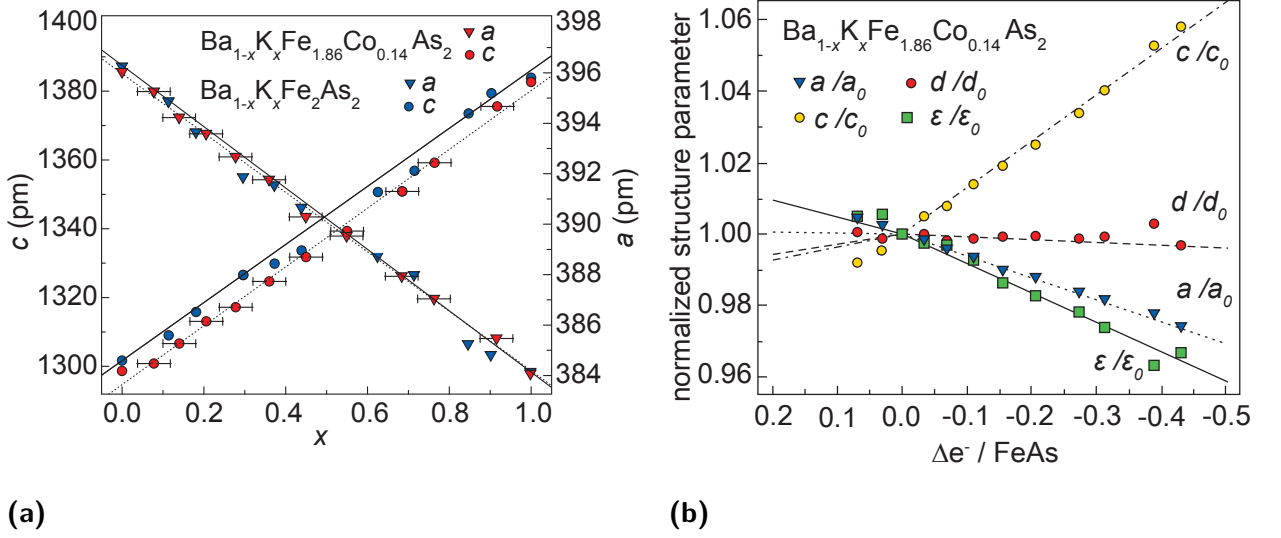
Fig. 8.3.: (a) Structural changes of $Ba_{1-x}K_xFe_{1.86}Co_{0.14}As_2$ (red, open symbols) with varying potassium content in comparison to $Ba_{1-x}K_xFe_2As_2$ (blue, filled symbols)[12]. (b) Normalized structure parameters (lattice parameters a, c, Fe-As bond length d and As-Fe-As angle ε) of $Ba_{1-x}K_xFe_{1.86}Co_{0.14}As_2$ plotted against the electron transfer per FeAs. Lines are fits to literature data of $Ba(Fe_{1-y}Co_y)_2As_2$[117] and $Ba_{1-x}K_xFe_2As_2$[12].

the variation of the electron count Δe^- per FeAs-layer. Lines are fits to literature data of electron-doped $Ba(Fe_{1-y}Co_y)_2As_2$[117] and hole-doped $Ba_{1-x}K_xFe_2As_2$[12]. We find an almost exact coincidence of all parameters in the hole-doped area. The lattice parameters in the electron-doped area do not agree with those of $Ba(Fe_{1-y}Co_y)_2As_2$, but continue increasing (a) and decreasing (c) and rather follow the lines of the potassium-substituted compounds extrapolated into the electron-doped area. The Fe-As bond lengths and As-Fe-As bond angles are close to the expected values also in the electron-doped area, however, the changes are very small and the extrapolations from the hole-doped part are also close to the fits for electron-doping. From these data we conclude that the crystal structure is mainly dominated by the potassium substitution in terms of atom size requirements. The increased charge alone cannot recover the crystal structures of electron-doped $Ba(Fe_{1-y}Co_y)_2As_2$ in $Ba_{1-x}K_xFe_{1.86}Co_{0.14}As_2$.

The undoped parent compound $BaFe_2As_2$ undergoes a structural and magne-

Table 8.1.: Crystallographic data of Ba$_{1-x}$K$_x$Fe$_{1.86}$Co$_{0.14}$As$_2$ ($x = 0.2$) at 293 K and 10 K.

Temperature (K)	293	10
Empirical formula	Ba$_{0.8}$K$_{0.2}$Fe$_{1.86}$Co$_{0.14}$As$_2$	Ba$_{0.8}$K$_{0.2}$Fe$_{1.86}$Co$_{0.14}$As$_2$
Crystal system, space group	Tetragonal, *I*4/*mmm*	Orthorhombic *Fmmm*
a, *c* (pm)	393.584(2), 1313.092(13)	554.614(15), 556.96(2)
		1306.60(6)
Cell volume (nm^3), *Z*	0.203409(3), 2	0.403606(25), 4
Radiation type, λ (Å)	Cu-Kα_1, 1.45	Co-Kα_1, 1.78890
2θ range	5.5 -100	5.5 -100
Number of data points	18901	18901
Total number of reflections	46	50
Refined parameters	35	60
Goodness-of-fit on F^2	0.979	0.605
R_p, R_{wp},	0.01748, 0.02354	0.01218, 0.01617
R_{exp}, $R(F^2)$	0.02407, 0.01919	0.02673, 0.006445
Atomic positions:	Ba/K 2*a* (0 0 0)	Ba/K 2*a* (0 0 0)
	Fe/Co 4*d* (0.5 0 0.25)	Fe/Co 8*f* (0.25 0.25 0.25)
	As 4*e* (0 0 0.353574(78))	As 8*i* (0 0 0.351602(94))

tic phase transition at 140 K[8]. We checked our samples for the orthorhombic distortion by structure determinations at low temperatures. Figure 8.4(a) shows the temperature dependence of the (110) reflections for $x = 0$, 0.08, 0.13, 0.2 and 0.35 and Figure 8.4(b) the lattice parameters a and b at low temperatures. In Ba$_{1-x}$K$_x$Fe$_{1.86}$Co$_{0.14}$As$_2$ ($x = 0$), no splitting of the (110) reflection is observed, the transition is absent as known from the literature[20]. When the electron-doping becomes gradually compensated by potassium-doping, we again observe the splitting of the (110) reflection (Figure 8.4(a)) that indicates the structural transition. For $x = 0.08$ a distinct broadening and for $x = 0.13$ a splitting of the (110) reflection is observed. The orthorhombic distortion becomes stronger and the phase transition shifts to higher temperatures (Figure 8.4(b)) up to the
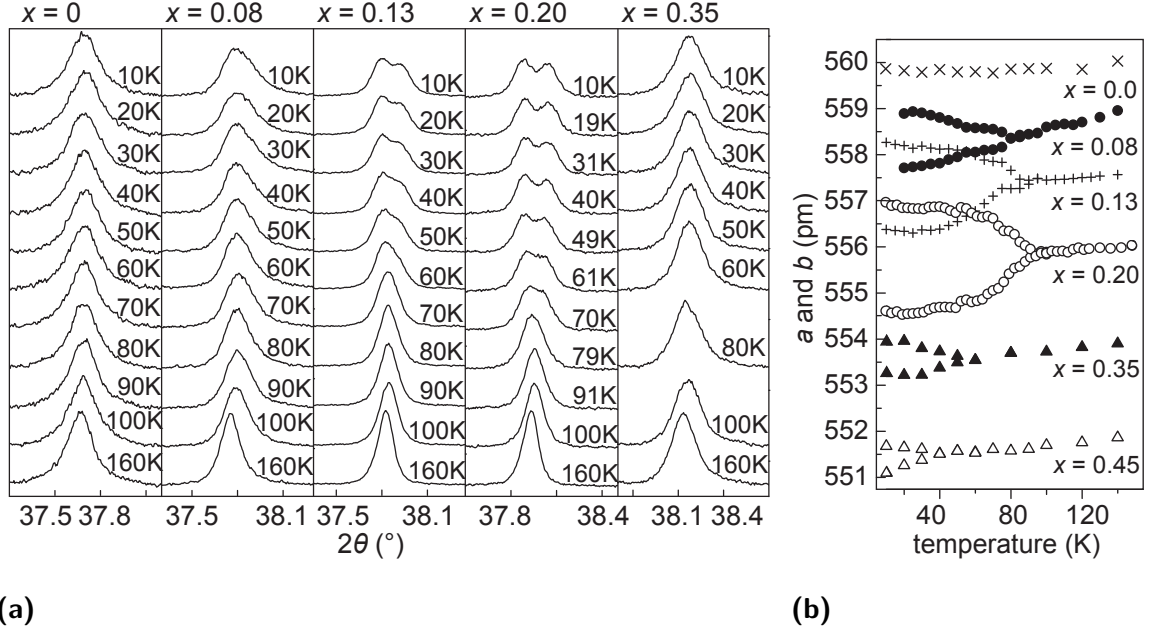
Fig. 8.4.: (a) Temperature dependence of the (110) reflection in $Ba_{1-x}K_xFe_{1.86}Co_{0.14}As_2$ with $x = 0$, 0.08, 0.13, 0.2 and 0.35. (b) Lattice parameters showing the orthorhombic distortion of $Ba_{1-x}K_x(Fe_{1-y}Co_y)_2As_2$ at low temperatures. The tetragonal parameters were multiplied by $\sqrt{2}$ for comparison.

nominal potassium-concentration of $x = 0.2$, where the electron doping has just been completely compensated. Structural data for $Ba_{1-x}K_xFe_{1.86}Co_{0.14}As_2$ ($x = 0.2$) at room temperature and 10 K are summarized in Table 8.1. The orthorhombic distortion observed here ($\Delta = b - a = 2.3$ pm) is weaker than in $BaFe_2As_2(\Delta = 4$ pm). With further increased hole-doping, the distortion becomes smaller again and is finally absent at $x > 0.5$. This result emphasizes the important effect of the charge concentration on the structural instability, which has its origin in the nested Fermi surface. As soon as we restore the charge balance, thus the nesting condition, the instability returns immediately, despite of the structural disorder induced by the simultaneous doping at the iron- and barium-sites.

The recovered structural transition of $Ba_{1-x}K_xFe_{1.86}Co_{0.14}As_2$ at $x = 0.2$ is accompanied by antiferromagnetic ordering as known from the parent compound

(a)

(b)
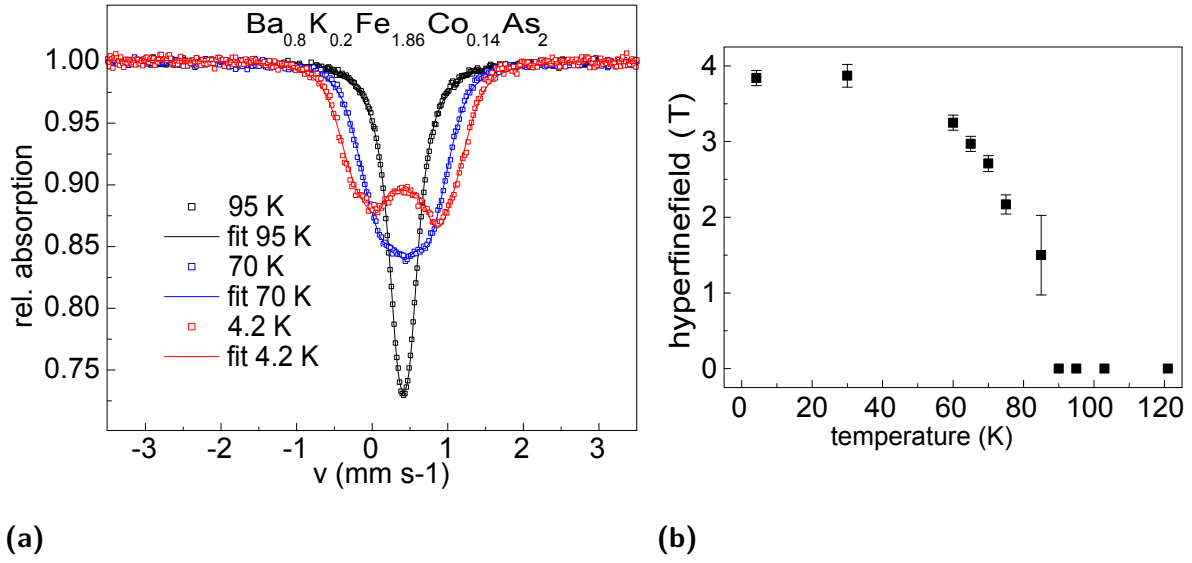
Fig. 8.5.: (a)[57]Fe-Mößbauer spectra of $Ba_{0.8}K_{0.2}Fe_{1.86}Co_{0.14}As_2$. (b) Temperature dependence of the magnetic hyperfine field.

$BaFe_2As_2$[8]. In Figure 8.5(a), temperature-dependent [57]Fe-Mößbauer spectra of $Ba_{0.8}K_{0.2}Fe_{1.86}Co_{0.14}As_2$ are shown. The single absorption line is subject to magnetic hyperfine field splitting at low temperatures that proves static magnetic ordering. The magnetic order parameter (Figure 8.5(b)) shows the onset at about 85 K, close to the splitting of the lattice parameters at about 92 K (Figure 8.4(b)). The hyperfine field converges at 3.9 T at low temperatures, which is smaller than the value of 5.7 T measured in $BaFe_2As_2$[8]. Since the orthorhombic splitting is also reduced in comparison to $BaFe_2As_2$, the strong correlation between magnetic and structural order parameters generally observed in the Ba- and Sr- based iron-pnictides with $ThCr_2Si_2$ structure is maintained[118].

The normalized electrical resistances R/R_{300K} of $Ba_{1-x}K_xFe_{1.86}Co_{0.14}As_2$ are shown in Figure 8.6, and Figure 8.7(a)-(c) displays plots of the AC susceptibility. The superconducting transition temperatures T_c (onset) were extracted as the intersection of two lines fitting the steepest descent and the normal-state susceptibility. $BaFe_{1.86}Co_{0.14}As_2$ ($x = 0$) is superconducting below 25 K as reported in the literature. Potassium-doping decreases the critical temperature to
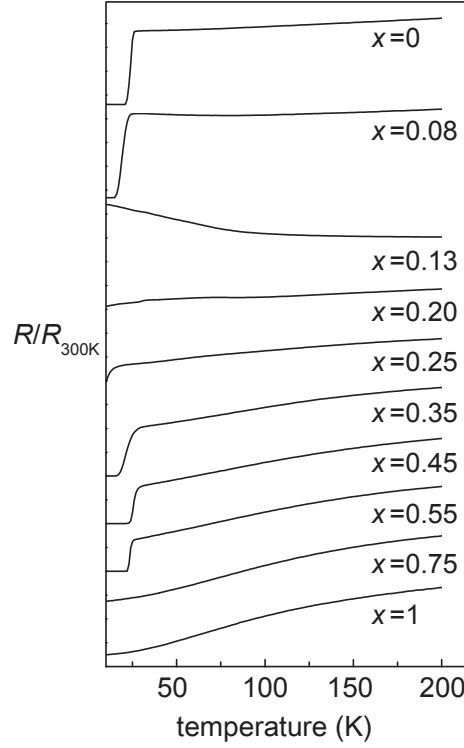
Fig. 8.6.: Normalized electrical resistances R/R_{300K} of $Ba_{1-x}K_xFe_{1.86}Co_{0.14}As_2$.

23 K at $x = 0.08$ until superconductivity is absent in the samples with $x = 0.13$ and 0.2, where the excess electrons are compensated by the holes introduced by potassium substitution. When the hole-doping outweighs in the samples with $x > 0.25$, superconductivity appears again and reaches the highest T_c of 28.6 K at $x = 0.45$. Thus the emergence of superconductivity is controlled by the charge concentration and shows the same behaviour as known from the only-cobalt- and only-potassium- substituted systems, but with smaller T_c in the hole-doped domain. ($T_{c,max} = 28.6$ K compared to 38 K for $Ba_{1-x}K_xFe_2As_2$). Also the ordered magnetic moment (3.9 T compared to 5.7 T) and the orthorhombicity parameter $\delta_o = $ (a-b)/(a+b) near the compensated concentration are smaller than in $BaFe_2As_2$. The phase diagram that arises from our data is presented in Figure 8.8. We note that the series $Ba_{1-x}K_x(Fe_{1-y}Co_y)_2As_2$ has been published recently by Suzuki et al.[119], but their diagram has no data points in the range that is of interest here.
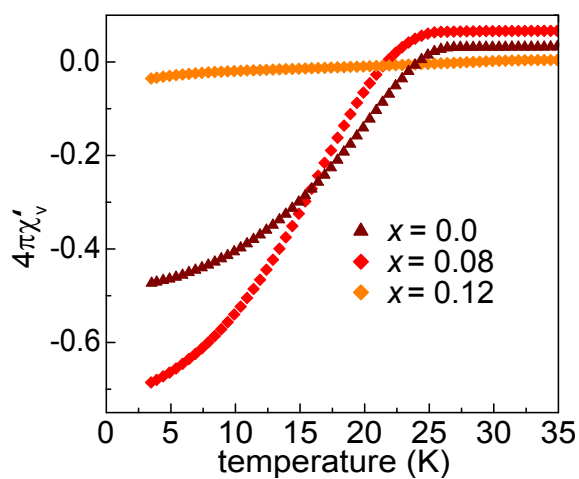
(a)
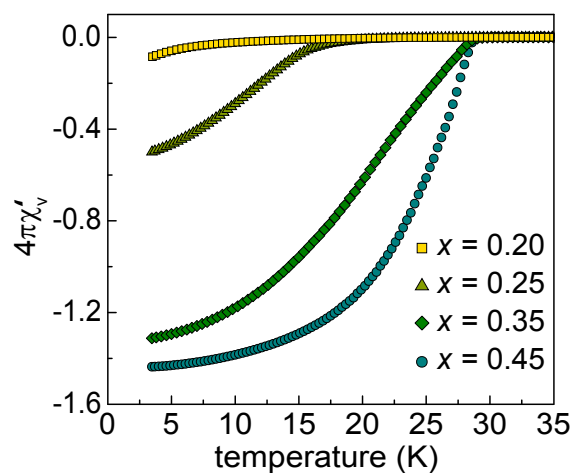
(b)
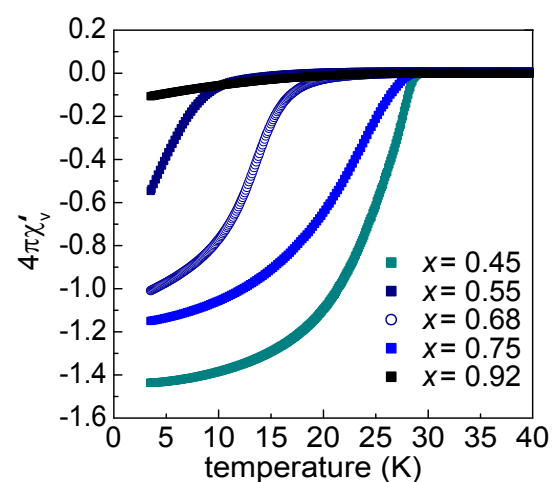
(c)

Fig. 8.7.: AC-susceptibility plots of $Ba_{1-x}K_xFe_{1.86}Co_{0.14}As_2$ for (a) $x = 0$ - 0.12, (b) $x = 0.2$ - 0.45 and (c) $x = 0.45$ - 0.92.
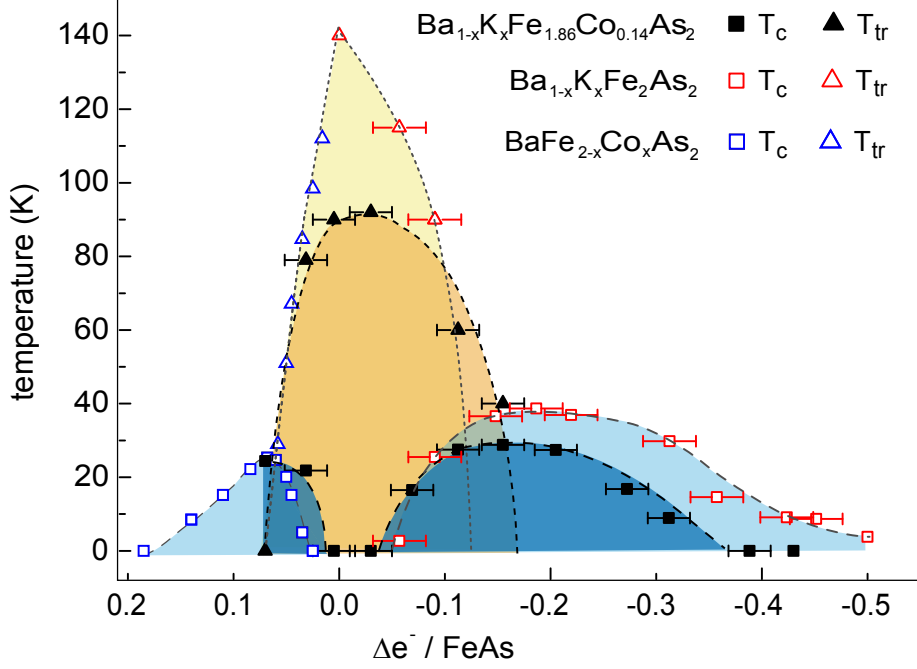
Fig. 8.8.: Phase diagram of $Ba_{1-x}K_xFe_{1.86}Co_{0.14}As_2$ (dark blue/orange) compared to the phase diagrams of $Ba_{1-x}K_xFe_2As_2$ and $Ba(Fe_{1-y}Co_y)_2As_2$ (light blue/ yellow). T_{tr} is the structural phase transition temperature.

The phase diagram of $Ba_{1-x}K_xFe_{1.86}Co_{0.14}As_2$ comprises those of $Ba_{1-x}K_xFe_2As_2$ ($x = 0$ - 1) and $Ba(Fe_{1-y}Co_y)_2As_2$ ($x = 0$ - 0.185) by varying only one parameter. The superconducting domes (dark blue shaded areas in Figure 8.8) are similar to those of the only-cobalt- and only-potassium doped phases (light blue), and also the areas of the orthorhombically distorted magnetic parent-like phases (dark and light yellow) are comparable. The lower phase transition temperatures and magnetic moments of the charge compensated phases around $\Delta e^- = 0$ may be due to the disorder induced by the Co-substitution in the iron layer. This could also be the reason for the lower T_c in the hole-doped area and the earlier vanishing of superconductivity at -0.38 e^-.

The results show that the charge concentration is the crucial parameter that controls magnetism, lattice distortion and the onset of superconductivity in electron- and hole-doped $BaFe_2As_2$. Especially the onset of superconductivity at

the same hole-concentration than in the cobalt-free phase ($-0.05\ e^-$) is striking and underlines the impact of the charge. The crystal structure itself in terms of lattice parameters, Fe-As bond lengths and bond angles appears to be less affected by the charge variation, but rather controlled by atom size requirements. The latter is most obvious for the c-axis, which shrinks much stronger with electron doping ($\Delta e^- = 0$ - 0.1) by decreasing the K-content in $Ba_{1-x}K_xFe_{1.86}Co_{0.14}As_2$ than in $Ba(Fe_{1-y}Co_y)_2As_2$ (Figure 8.3(b)). The results presented here are also in good agreement with the photoemission data suggesting a rigid band-like filling or depleting of the electronic states near the Fermi level[115]. Even though the occurrence of superconductivity is clearly connected to the charge of the $(FeAs)^{\delta-}$-layer, the role of the crystal structure should not be underestimated. It was noticed early that the maximum T_c of 38 K in $Ba_{1-x}K_xFe_2As_2$ at $x \approx 0.4$ ($\Delta e^- \approx -0.2$) coincides with an As-Fe-As bond angle close to the ideal value of $109.47°$[12]. For $Ba_{1-x}K_xFe_{1.86}Co_{0.14}As_2$, the maximum T_c appears at $\Delta e^- = -0.16$ when the angle is $109.5°$, slightly shifted from the Cobalt-free phases that have the maximum at $\Delta e^- = -0.2$ (Figure 8.8).

In spite of the apparent relation to T_c, the true role of the bond angle is still unclear. Even its decrease from $111.1°$ in $BaFe_2As_2$ to $109.5°$ and lower by hole-doping cannot be well understood from atom sizes alone, because substitution of alkaline metals for barium always decreases the angle. Even if barium is replaced by much smaller sodium atoms in $Ba_{1-x}Na_xFe_2As_2$[120], the c-axis increases and the angle becomes smaller until it reaches $109.5°$ at $x \approx 0.4$, where again the T_c is the highest. This indicates that the angle may also be controlled by the electron count.

In summary, we have shown how the physical properties of doped $BaFe_2As_2$ are predominantly controlled by the charge of the $(FeAs)^{\delta-}$-layers. Continuous adjusting from electron- to hole-doping in the solid solution $Ba_{1-x}K_xFe_{1.86}Co_{0.14}As_2$ tunes the system from superconductivity to a magnetic state and back to superconductivity. This recovery of the magnetic phase similar to that of the parent

compound is unprecedented and emphasizes the role of the layer charge. Our results suggest that structural parameters like bond length or angles play a minor role with respect to the incurrence of superconductivity in electron- or hole doped systems, but are certainly important to achieve the highest possible critical temperatures.

9. $Ba_{1-x}K_x(Fe_{1-y}Co_y)_2As_2$ - the charge compensated state

9.1. Introduction

As we have seen in the last chapter, the combination of potassium and cobalt substitution in $Ba_{1-x}K_xFe_{1.86}Co_{0.14}As_2$ leads to a compensation of hole and electron doping. A non-superconducting, parent-like state is observed for $x = 0.13$ and $x = 0.2$, where the tetragonal to orthorhombic phase transition, well known fom the parent compound $BaFe_2As_2$, is found and antiferromagnetic ordering was evidenced for $x = 0.2$. But what would happen if both K and Co content in $Ba_{1-x}K_x(Fe_{1-y}Co_y)_2As_2$ were increased while staying in the charge compensated area ($x/2 \approx y$)? The endpoint of this series on the potassium-rich side is $KFeCoAs_2$ (already presented in chapter 7), where no SDW anomaly is observed, in spite of the great similarity of the calculated fermi surface to that of $BaFe_2As_2$. Instead, $KFeCoAs_2$ shows simple metallic behaviour. Thus the magnetism in $Ba_{1-x}K_x(Fe_{1-y}Co_y)_2As_2$ is expected to disappear at some point with increasing potassium and Co substitution, even in the compensated state. Furthermore, Suzuki et. al.[119], who investigated single crystals of $Ba_{1-x}K_x(Fe_{1-y}Co_y)_2As_2$, report superconductivity for several samples with $x/2 \approx y = 0.14$ - 0.22.

To verify these findings and to investigate more closely the influence of increased doping on structure, magnetism, phase transitions and superconductivity, polycrystalline samples of $Ba_{1-x}K_x(Fe_{1-y}Co_y)_2As_2$ with $x/2 \approx y = 0$ - 0.25 were synthesized. This chapter presents detailed studies of the structure and proper-

ties of these both potassium and cobalt doped, charge compensated samples at room and low temperatures.

9.2. Experimental Methods

For the study of Ba$_{1-x}$K$_x$(Fe$_{1-y}$Co$_y$)$_2$As$_2$, polycrystallinic samples were synthesized, since this gives better homogenity of the potassium content than the synthesis of single crystals. The synthesis method and temperature program described in chapter 8 were used, but to compensate the loss of potassium during synthesis, 3 - 5 % additional potassium was added. Nevertheless, the composition of some of the samples deviates slightly from $x/2 \approx y$. Resistivity was measured on cold pressed and annealed (873 K) pellets in the temperature range 10 K - 320 K or 3.5 - 320 K using the four probe technique. The data was complemented by AC susceptibility measurements. Powder diffraction data were collected on a Huber G670 diffractometer with Co-K$_{\alpha 1}$ or Cu-K$_{\alpha 1}$-radiation, equipped with a closed cycle He cryostat. Mößbauer spectra were recorded in transmission geometry using a ^{57}Co/Rh source. The spectrometer was calibrated with a 8μm thin α-Fe foil at room temperature. The powdered sample was mixed with methanol in a PA6.6 container to ensure a homogeneous surface thickness of 8.2 mg Fe/cm^2. A CryoVac Konti IT cryostat with He or N$_2$ as exchange gas was used to stabilize temperatures between 4.2 K and 300 K.

9.3. Results and Discussion

While for Ba$_{1-x}$K$_x$Fe$_{1.86}$Co$_{0.14}$As$_2$ the structural changes were dominated by the potassium substitution, the influence of the additional cobalt substitution on the structure becomes visible at higher Co contents. Figure 9.1 depicts the structural changes upon substitution in charge compensated Ba$_{1-x}$K$_x$(Fe$_{1-y}$Co$_y$)$_2$As$_2$ (red) compared to hole doped Ba$_{1-x}$K$_x$Fe$_2$As$_2$ (blue) (plots against $x/2$ are shown;
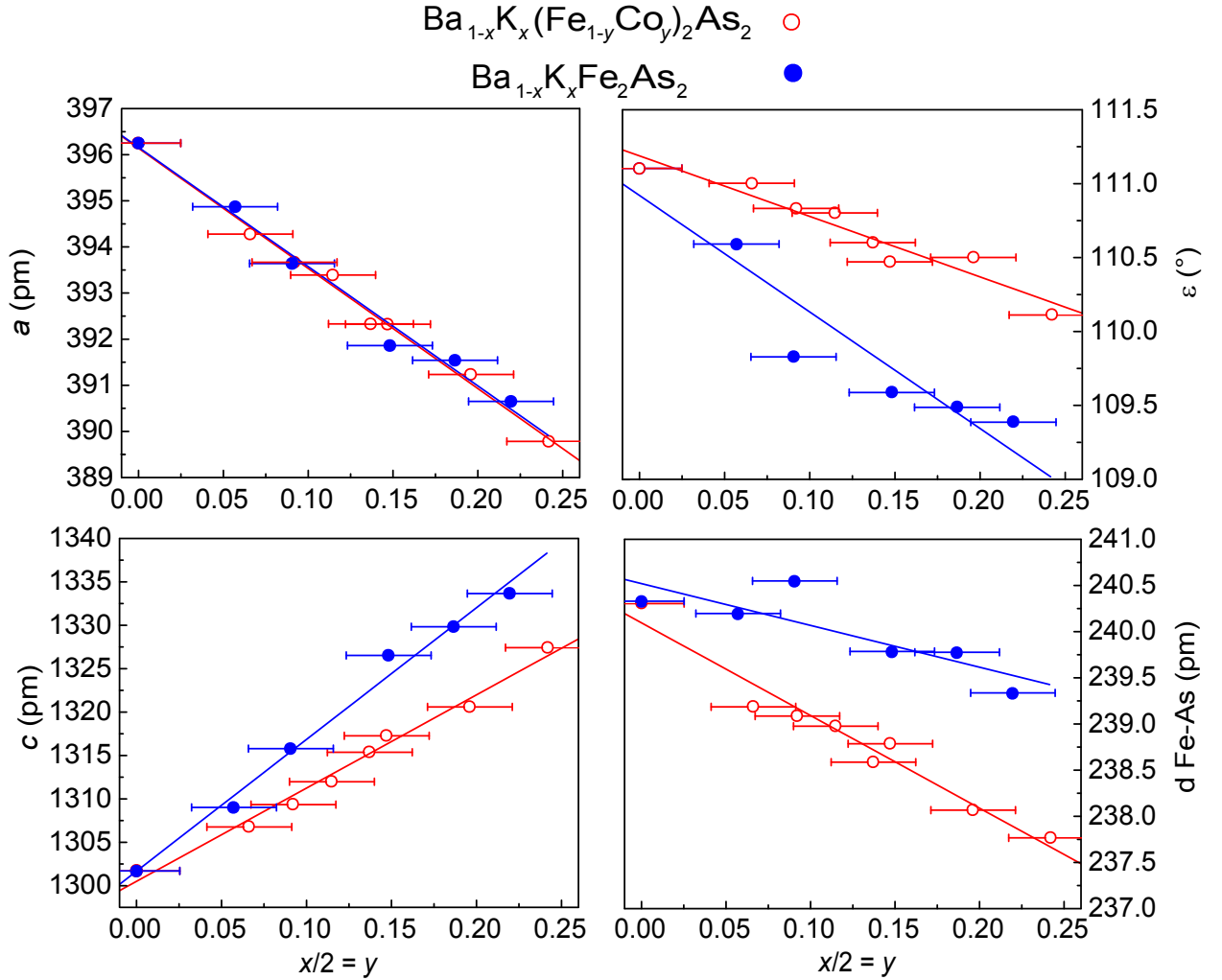
Fig. 9.1.: Structural changes in charge compensated $Ba_{1-x}K_x(Fe_{1-y}Co_y)_2As_2$ (red, unfilled symbols) compared to $Ba_{1-x}K_xFe_2As_2$ (blue, filled symbols) with increasing potassium content per FeAs-layer ($x/2$). Lattice parameter a (top left) and c (bottom left), As-Fe-As angle ε (top right) and Fe-As distance d (bottom right). Note that $x/2 \approx y$. Data for $Ba_{1-x}K_xFe_2As_2$ taken from [12].
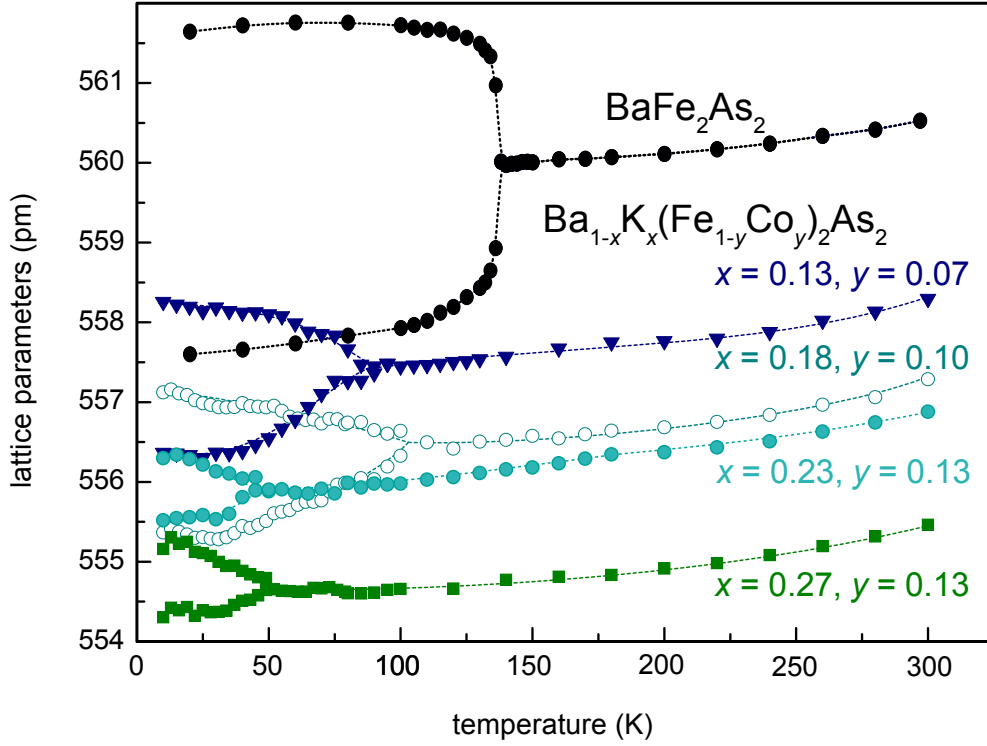
Fig. 9.2.: Lattice parameters of Ba$_{1-x}$K$_x$(Fe$_{1-y}$Co$_y$)$_2$As$_2$ $x/2 \approx y = 0$ - 0.13, showing the orthorhombic distortion at low temperatures. Data for BaFe$_2$As$_2$ from [98].

note that $x/2 \approx y$ for the Ba$_{1-x}$K$_x$(Fe$_{1-y}$Co$_y$)$_2$As$_2$ samples). While a is not affected by the additional cobalt substitution and decreases at the same rate as in Ba$_{1-x}$K$_x$Fe$_2$As$_2$, the increase of c is clearly reduced in Ba$_{1-x}$K$_x$(Fe$_{1-y}$Co$_y$)$_2$As$_2$. Consequently, the value of the As-Fe-As angle ε changes less for Ba$_{1-x}$K$_x$(Fe$_{1-y}$Co$_y$)$_2$As$_2$ than reported for Ba$_{1-x}$K$_x$Fe$_2$As$_2$ and reaches only $\sim$110.5° at $x/2 = 0.2$, where the ideal tetrahedral angle of 109.47° is found in Ba$_{1-x}$K$_x$Fe$_2$As$_2$. Interestingly, Co doping also leads to a decrease of the Fe-As distance d; a reduction of $\sim$1 % is found for $x/2 = 0.25$ compared to only $\sim$0.3 % in Ba$_{1-x}$K$_x$Fe$_2$As$_2$. All in all, we conclude that for higher doping levels in Ba$_{1-x}$K$_x$(Fe$_{1-y}$Co$_y$)$_2$As$_2$, both potassium and cobalt doping influence the structure significantly.

As we have seen in chapter 8, charge compensated Ba$_{0.87}$K$_{0.13}$Fe$_{1.86}$Co$_{0.14}$As$_2$ shows the tetragonal to orthorhombic phase transition, but with a reduced or-

thorhombic distortion compared to $BaFe_2As_2$. To check how this phase transition is influenced by increased cobalt and potassium doping in the compensated state, low temperature powder diffraction was performed. The results, depicted in Figure 9.2, show that the splitting of the lattice parameters becomes weaker with increasing doping level. The splitting is significantly reduced from $\Delta = b - a$ = 4 pm in $BaFe_2As_2$ to $\sim$ 2 pm for $x/2 \approx y \approx 0.07$ and 0.09 and further to $\sim$ 0.8 pm for $x/2 \approx y \approx 0.13$, where only a broadening of reflections at low temperatures is observed. Due to the diminutive size of the splitting it is difficult to determine the exact phase transition temperatures by the rietveld method, but the general trend - a decrease of the structural phase transition temperature T_s - is clearly visible. Thus we observe a decrease of both orthorhombic distortion and phase transition temperatures with increasing substitution level $x/2 \approx y$ in charge compensated $Ba_{1-x}K_x(Fe_{1-y}Co_y)_2As_2$, which means that the structural phase transition is subsequently suppressed.

Temperature dependent Mößbauer spectra were recorded to check how the magnetic phase transition temperature and the magnetic hyperfine field at low temperatures are influenced by the increasing cobalt and potassium content. For $Ba_{0.8}K_{0.2}Fe_{1.86}Co_{0.14}As_2$, Mößbauer data was already presented in chapter 8 (Figure 8.5) showing an onset of magnetic ordering close to 85 K and a magnetic hyperfine field of 3.9 T at 4.2 K. Figure 9.3 displays ^{57}Fe Mößbauer spectra of $Ba_{1-x}K_x(Fe_{1-y}Co_y)_2As_2$ with $x/2 \approx y = 0.1$ (a) and $x/2 \approx y = 0.13$ (b) for several temperatures above and below the magnetic phase transition. At low temperatures, hyperfine field splitting is found for both samples, which indicates long range magnetic ordering. The splitting is less pronounced than in $Ba_{0.8}K_{0.2}Fe_{1.86}Co_{0.14}As_2$. For $Ba_{1-x}K_x(Fe_{1-y}Co_y)_2As_2$ with $x/2 \approx y = 0.1$, the temperature dependence of the magnetic hyperfine field is plotted in Figure 9.3(c) (cyan, filled circles). In the temperature range 60 - 80 K line broadening is observed, but the effect is too small to assign a finite value for the hyperfine field. The broadening could originate from magnetic ordering in part of the sample,

(a)

(b)

(c)
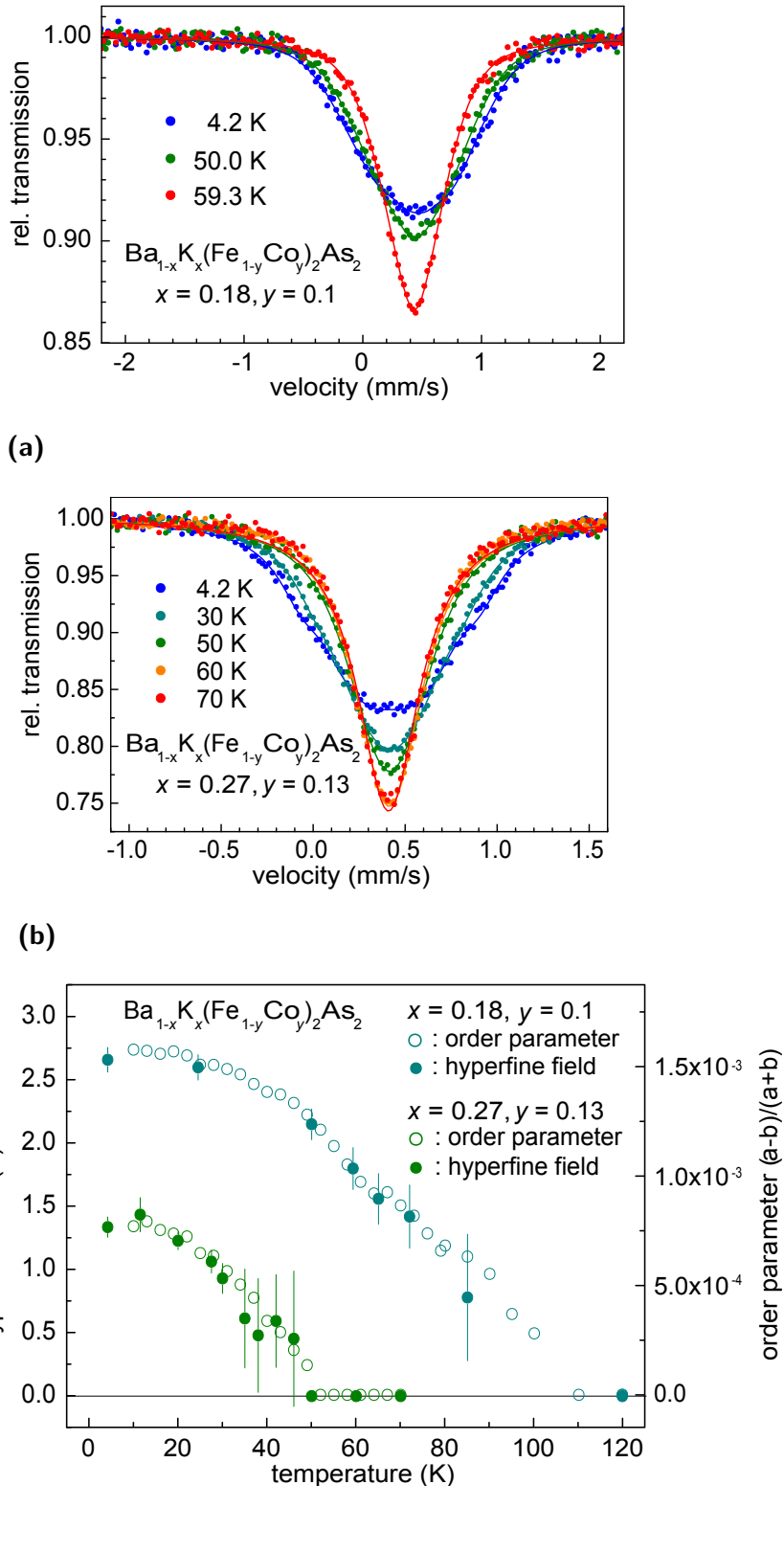
Fig. 9.3.: ^{57}Fe Mößbauer spectra of $Ba_{1-x}K_x(Fe_{1-y}Co_y)_2As_2$ for (a) $x/2 \approx y = 0.1$ and (b) $x/2 \approx y = 0.13$. (c) Temperature dependence of the hyperfine field /weighted hyperfine field in comparison to the orthorhombic order parameter $(a - b)/(a + b)$.

but might also be caused by fluctuations of the lattice. Below 62 K however, long range static magnetic ordering is observed and at 4.2 K a saturation value of 2.7 T is found for the magnetic hyperfine field. For $Ba_{1-x}K_x(Fe_{1-y}Co_y)_2As_2$ with $x/2 \approx y = 0.13$ (b) the hyperfine field (Figure 8.5, green, filled circles) converges to 1.5 T at 4.2 K. Similar to $Ba_{1-x}K_x(Fe_{1-y}Co_y)_2As_2$ ($x/2 \approx y = 0.1$), some line broadening is observed in a transition region between 40 and 50 K.

For a comparison of the development of structural distortion and magnetic ordering at low temperatures, plots of the structural order parameter $(a-b)/(a+b)$ and the magnetic order parameter (mößbauer hyperfine field) against the temperature are shown in Figure 9.3(c). Data for $Ba_{1-x}K_x(Fe_{1-y}Co_y)_2As_2$ with $x/2 \approx y = 0.1$ is depicted in cyan and for $x/2 \approx y = 0.13$ in green (open circles). For both compositions, the curves of the structural and the magnetic order parameter show no differences within the error bars, although for $x/2 \approx y = 0.1$ few data points near the transition were measured. Still, the data is in better agreement with a magnetic phase transition very close to the temperature of the structural phase transition as reported for $Ba_{1-x}K_xFe_2As_2$[98], in contrast to a separation of both transition temperatures as it is well kown from $Ba(Fe_{1-y}Co_y)_2As_2$[21] and was proposed for $Ba_{1-x}K_x(Fe_{1-y}Co_y)_2As_2$[119].

To summarize, the magnetic hyperfine field is reduced from 5.7 T at 4.2 K in $BaFe_2As_2$[12] to 3.9 T in $Ba_{0.8}K_{0.2}Fe_{1.86}Co_{0.14}As_2$, to 2.7 T for $x/2 \approx y = 0.1$ and to 1.5 T for $x/2 \approx y = 0.13$ in $Ba_{1-x}K_x(Fe_{1-y}Co_y)_2As_2$. A decrease of both Neel temperature and magnetic hyperfine field is observed with increasing Co and K content $x/2 \approx y$. This demonstrates that a weakening of magnetism takes place with increasing doping level - even in the charge compensated case.

For single crystals of $Ba(Fe_{1-y}Co_y)_2As_2$, the resistivity ususally shows an upturn at T_s and saturates close to the magnetic phase transition temperature T_N. Powder samples of $Ba_{1-x}K_x(Fe_{1-y}Co_y)_2As_2$ with $x/2 \approx y \approx 0.07$ and 0.1 show a similar upturn of the resistivity near the temperature of the structural phase transition (Figure 9.4(a)). For $x = 0.23$ and $y = 0.13$, the upturn has disappeared,
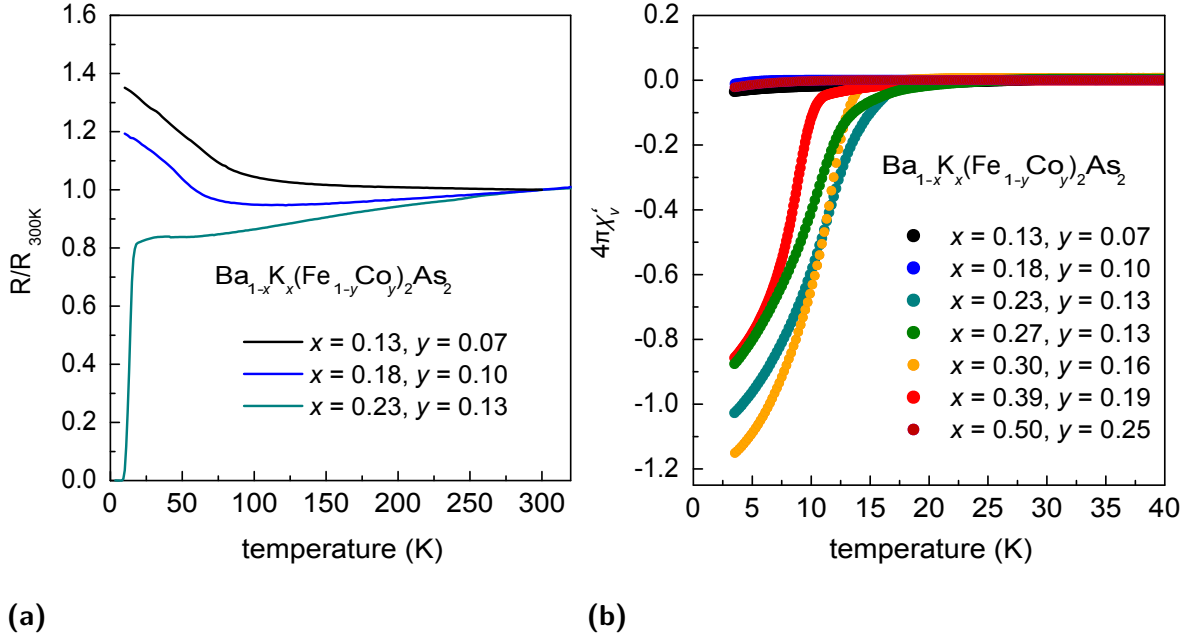
Fig. 9.4.: (a) Normalized electrical resistances R/R$_{300K}$ of $Ba_{1-x}K_x(Fe_{1-y}Co_y)_2As_2$ for $x/2 \approx y = 0.07$ - 0.13. (b) AC susceptibility plots for $x/2 \approx y = 0.07$ - 0.25.

instead the resistance drops to zero below T_c(onset) = 16 K. Measurements of the AC susceptibility confirm bulk superconductivity for $Ba_{1-x}K_x(Fe_{1-y}Co_y)_2As_2$ with $x/2 \approx y = 0.13$-0.19 (Figure 9.4(b)). At $x/2 \approx y = 0.25$ (dark red), no bulk superconductivity is observed, which shows the superconducting dome only spans about 10 % in the cobalt content.

The data for $Ba_{1-x}K_x(Fe_{1-y}Co_y)_2As_2$ ($x/2 \approx y$) is summarized in a phase diagram in Figure 9.5, combined with the data for $Ba_{1-x}K_xFe_{1.86}Co_{0.14}As_2$ from chapter 8. The phase diagram is colour coded: non-superconducting regions are depicted in blue and the superconducting dome is shown in yellow (for $T_c \approx$ 10 K) to dark red ($T_c = 38$ K). Data points from this work are marked by black squares and the respective transition temperatures (T_c(onset) in AC susceptibility) are given. The measurements add to the data on $Ba_{1-x}K_x(Fe_{1-y}Co_y)_2As_2$ published by Suzuki et. al.[119] (grey squares) and confirm their reports on superconductivity in charge compensated samples. The data of both series agree reasonably well. However, Suzuki et. al. present only two data points with $x/2$
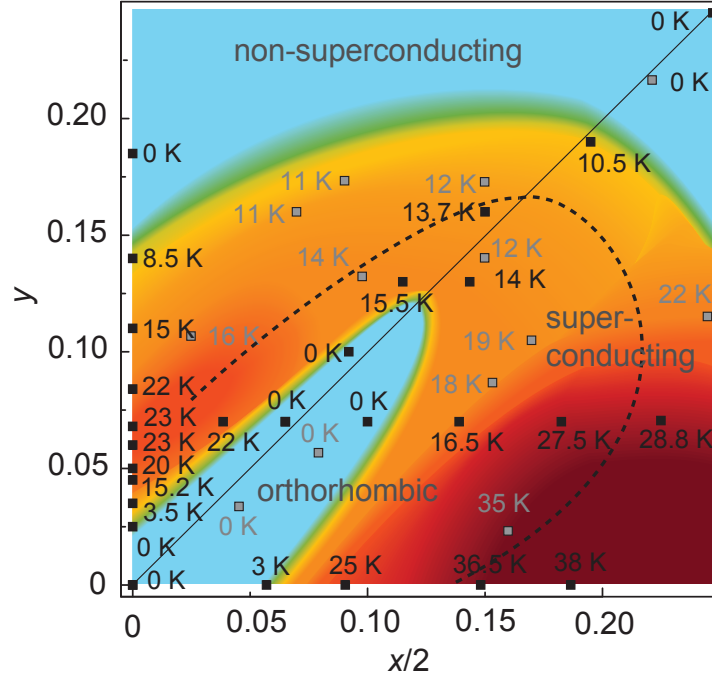
Fig. 9.5.: Phase diagram of $Ba_{1-x}K_x(Fe_{1-y}Co_y)_2As_2$ for $x/2$ and $y \leq 0.25$. Black squares: Data points with corresponding superconducting transition temperatures. Grey squares: data from [119]. Blue: non-superconducting, red-yellow: superconducting, highest T_c's depicted in dark red. Dashed line: tentative border for the existance of the orthorhombic phase. Data for $Ba_{1-x}K_xFe_2As_2$ from [12] and for $Ba(Fe_{1-y}Co_y)_2As_2$ from [121].

$\approx y \leq 0.05$ in the underdoped, non-superconducting region of the phase diagram. Thus they missed the recovered parent-like state in charge compensated $Ba_{1-x}K_x(Fe_{1-y}Co_y)_2As_2$ in the region of the phase diagram where the concentration of each dopant alone would induce superconductivity (for $x/2 > 0.05$[12] and $y > 0.037$[122]). The non-superconducting area extends beyond $x/2 \approx y = 0.1$. For 0.13, superconductivity is found, but a reduced superconducting volume fraction for samples close to the ideal $x/2 = y = 0.13$ suggests this concentration to be close to the border of the superconducting dome. The highest T_c's are found for hole doped $Ba_{1-x}K_xFe_2As_2$ and throughout the whole phase diagram, the transition temperatures on the hole-doped side are higher than those at the same Co content on the electron-doped side. The disorder in the $FeAs_{4/4}$ layers by Co doping is often used as an argument to explain the lower T_c's in $Ba(Fe_{1-y}Co_y)_2As_2$

compared to Ba$_{1-x}$K$_x$Fe$_2$As$_2$. Our results suggest however, that even at the same degree of distortion within the tetrahedra layers, hole doping of BaFe$_2$As$_2$ gives higher transition temperatures. Also, the superconducting area spreads further on the hole doped side. For charge compensated Ba$_{1-x}$K$_x$(Fe$_{1-y}$Co$_y$)$_2$As$_2$, the superconducting dome is extended to higher Co contents than for electron doped Ba(Fe$_{1-y}$Co$_y$)$_2$As$_2$. This shows that the "charge" is likely to play a role in the suppression of superconductivity in Ba(Fe$_{1-y}$Co$_y$)$_2$As$_2$.

Because electron doping is compensated by hole doping for $x/2 = y$, the occurrence of superconductivity can not be explained by charge doping. Therefore, a comparison with isoelectronic doping suggests itself. Here, Ba(Fe$_{1-y}$Ru$_y$)$_2$As$_2$ seems to be the best candidate, since in both cases the substitution (or part of it) takes place in the iron layer. For Ba(Fe$_{1-y}$Ru$_y$)$_2$As$_2$, a suppression of the SDW transition upon Ru substitution is found, superconductivity sets in at y = 0.2 and transition temperatures up to 19 K are observed[123]. Recent ARPES measurements show no significant changes of the shape of the fermi surface or the chemical potential upon Ru substitution[124]. This rules out charge doping by a different ruthenium valence as the reason for the occurrence of superconductivity. Thus Ba(Fe$_{1-y}$Ru$_y$)$_2$As$_2$ and Ba$_{1-x}$K$_x$(Fe$_{1-y}$Co$_y$)$_2$As$_2$ ($x/2 = y$) are expected to show similar properties.

Figure 9.6 compares the phase diagrams of Ba(Fe$_{1-y}$Ru$_y$)$_2$As$_2$ and compensated Ba$_{1-x}$K$_x$(Fe$_{1-y}$Co$_y$)$_2$As$_2$ (T_s and T_c versus y are shown). While the superconducting transition temperatures are similar, both phase diagrams show a number of differences otherwise: For Ba$_{1-x}$K$_x$(Fe$_{1-y}$Co$_y$)$_2$As$_2$ ($x/2 \approx y$), superconductivity is observed at $y = 0.13$, for Ba(Fe$_{1-y}$Ru$_y$)$_2$As$_2$ it sets in only at $y \approx 0.2$. The superconducting dome extends to $y > 0.4$ in the case of Ru substitution, while Ba$_{1-x}$K$_x$(Fe$_{1-y}$Co$_y$)$_2$As$_2$ is already non-superconducting at $x/2 \approx y = 0.25$. A similar trend is seen for the suppression of the structural phase transition, that happens at a much lower Co than Ru content. The differences might be explained by the fact that potassium doping introduces additional disorder and that the
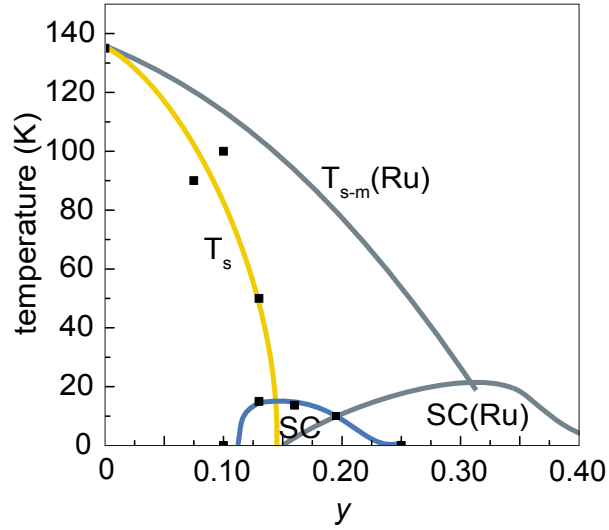
Fig. 9.6.: Comparison of the phase diagrams of $Ba_{1-x}K_x(Fe_{1-y}Co_y)_2As_2$ and $Ba(Fe_{1-y}Ru_y)_2As_2$ [123] (plot against y).

phase diagram should be scaled with $x/2 + y$. However, indirect substitution should have less effect on the $FeAs_{4/4}$- layer and the superconducting properties. Co may also be a more effective scattering center than Ru (for example because of a local charge or magnetic moment on the Co atom) and thus introduce more disorder. A comparison of the structural changes reveals further differences for both substitution series: In $Ba_{1-x}K_x(Fe_{1-y}Co_y)_2As_2$ ($x/2 = y$) a decrease of the lattice parameter a and an increase in c is observed (as shown in Figure 9.1), in contrast to an increase in a and a decrease of c in $Ba(Fe_{1-y}Ru_y)_2As_2$.

The differences of the phase diagrams suggest different mechanisms for the suppression of magnetism and the induction of superconductivity in charge compensated $Ba_{1-x}K_x(Fe_{1-y}Co_y)_2As_2$ and $Ba(Fe_{1-y}Ru_y)_2As_2$. In $Ba(Fe_{1-y}Ru_y)_2As_2$, one explanation for these effects is magnetic dilution [124]: As a $4d$ element, Ru has a smaller stoner enhancement parameter than Fe. Thus ruthenium substiution can reduce the effective stoner enhancement parameter resulting in the suppression of magnetism. But what possible explanation can be found for $Ba_{1-x}K_x(Fe_{1-y}Co_y)_2As_2$ ($x/2 = y$)?

As mentioned in chapter 7, DFT calculations on $KFeCoAs_2$ show a reduced

N(E$_F$) due to a decrease of the lattice parameter a[110]. However, this reduction seems to be too small (for Ba$_{1-x}$K$_x$(Fe$_{1-y}$Co$_y$)$_2$As$_2$ with $x/2 = y \approx 0.13$) to destabilize the magnetic order[119]. Otherwise, the structural parameters (depicted in Figure 9.1) are not likely to explain the properties of Ba$_{1-x}$K$_x$(Fe$_{1-y}$Co$_y$)$_2$As$_2$ ($x/2 = y$). The only interesting feature is the reduction of the Fe-As-distance (-1 % at $x/2 \approx y = 0.25$). Since for BaFe$_2$(As$_{1-x}$P$_x$)$_2$, d(FeAs) was found to be a gauge for the magnetic moment, its decrease might cause the suppression of the magnetism[28]. However, the change in d(FeAs) is less pronounced in Ba$_{1-x}$K$_x$(Fe$_{1-y}$Co$_y$)$_2$As$_2$ ($x/2 = y$) than in BaFe$_2$(As$_{1-x}$P$_x$)$_2$, where a reduction of $\sim$ 1.3 % was found at T$_{c,max}$.

Recent PDF studies show local distortions that introduce disorder in Ba(Fe$_{1-y}$Co$_y$)$_2$As$_2$, resulting in a clear deviation of the local from the average structure at $y = 0.2$[125]. A model with Fe atoms displaced towards Co is proposed for the local structure. Theory suggests that non-magnetic impurities introduced by doping can damage the spin density wave order more than the s$^\pm$-superconductivity, because "both intra- and interband scattering is destructive for SDW, but only inter-band scattering is pair-breaking for an s$^\pm$-superconductor"[126]. This scenario, where doping introduces disorder but does not affect the band structure, could explain a phase diagram as shown in Figure 9.6[126] and seems to be fulfilled in Ba$_{1-x}$K$_x$(Fe$_{1-y}$Co$_y$)$_2$As$_2$ ($x/2 = y$). For Ba$_{1-x}$K$_x$(Fe$_{1-y}$Co$_y$)$_2$As$_2$, the topology of the Fermi surface is not expected to change much with increasing $x/2 = y$, because the fermi surface of KFeCoAs$_2$, the endpoint of the series, is still very similar to BaFe$_2$As$_2$[110]. Also, it seems reasonable that Co can act as non-magnetic impurity, since NMR measurements on BaFe$_{1.8}$Co$_{0.2}$As$_2$ gave no evidence for magnetic moments induced by the Co doping[127]. Thus, the suppression of the SDW and the emerging of superconductivity in charge compensated Ba$_{1-x}$K$_x$(Fe$_{1-y}$Co$_y$)$_2$As$_2$ could be explained by disorder effects due to Co doping.

To summarize, Ba$_{1-x}$K$_x$(Fe$_{1-y}$Co$_y$)$_2$As$_2$ with $x/2 \approx y = 0$ - 0.25 was synthe-

sized and investigated. The additional cobalt doping results in a slower increase of the lattice parameter c compared to potassium doping alone. For $x/2 \approx y = 0$ - 0.13, the tetragonal to orthorhombic phase transition was observed by low temperature powder diffraction, with decreasing transition temperatures and orthorhombic splitting at higher doping levels. AC susceptibility and resistivity measurements show bulk superconductivity for $x/2 \approx y = 0.13$ - 0.19, but is absent for 0.25. A maximum T_c of ~ 15 K is found. The data agrees with results by Suzuki et. al.[119]. A $x/2$-y phase diagram visualizes the various intriguing effects found in $Ba_{1-x}K_x(Fe_{1-y}Co_y)_2As_2$: charge compensation resulting in an extension of the non-superconducting area at low temperatures, the emerging of superconductivity at higher doping levels ($x/2 = y > 0.13$) even for $x/2 = y$, connected with the suppression of the SDW-state, and the different shape of the superconducting dome for electron and hole doped $Ba_{1-x}K_x(Fe_{1-y}Co_y)_2As_2$. The phase diagram of $Ba_{1-x}K_x(Fe_{1-y}Co_y)_2As_2$ with $x/2 \approx y$ is compared to that of $Ba(Fe_{1-y}Ru_y)_2As_2$. While the maximum T_c is similar, a different dependency on y makes it unlikely that a similar mechanism is responsible for the suppression of magnetism and the occurrence of superconductivity in both cases. It has been shown that Co doping introduces disorder because of local distortions[125] and that doping acting as disorder can explain a phase diagram like the one observed for $Ba_{1-x}K_x(Fe_{1-y}Co_y)_2As_2$ ($x/2 \approx y$)[126]. Thus, is seems that disorder introduced by Co doping can explain both the suppression of the SDW-wave and the occurrence of superconductivity in charge compensated $Ba_{1-x}K_x(Fe_{1-y}Co_y)_2As_2$.

10. The interplay of electron doping and chemical pressure in Ba(Fe$_{1-y}$Co$_y$)$_2$(As$_{1-x}$P$_x$)$_2$

10.1. Introduction

In the last two chapters it has been shown that simultaneous hole and electron doping leads to a number of surprising results. At low doping levels, hole and electron doping seem to cancel each other out, resulting in a non-superconducting, parent-like state if the number of holes equals the number of electrons introduced into the FeAs$_{4/4}$-layer by charge doping. At higher doping levels, superconductivity appears even in the compensated state (although at lower temperatures), possibly due to a weakening of the magnetism and the disorder induced by doping. In any case, the example of Ba$_{1-x}$K$_x$(Fe$_{1-y}$Co$_y$)$_2$As$_2$ shows that simultaneous double substitution in BaFe$_2$As$_2$ gives unpredictable results.

In this chapter the effects of simultaneous isoelectronic and charge doping in the series Ba(Fe$_{1-y}$Co$_y$)$_2$(As$_{1-x}$P$_x$)$_2$ are investigated. Because phosphorus is isoelectronic to arsenic, no charge doping is involved in the case of BaFe$_2$(As$_{1-x}$P$_x$)$_2$ (phase diagram presented in Figure 1.4), and other effects should be responsible

for the suppression of the SDW state and the occurrence of superconductivity with a maximum T_c of 30 K. Since the atomic radius of P is smaller than that of As (introducing so-called "chemical pressure"), an analogy to superconductivity in BaFe$_2$As$_2$ under pressure is seen, although the appearance of superconductivity in BaFe$_2$(As$_{1-x}$P$_x$)$_2$ can not be attributed to cell volume effects alone[28]. Another difference to electron doping in BaFe$_2$As$_2$ is the occurrence of a nodal gap in BaFe$_2$(As$_{1-x}$P$_x$)$_2$, strongly suggested by penetration depth and heat transport measurements, NMR and ARPES experiments[106,128,129]. What will happen if phosphorus doping is combined with electron doping? Will the effects of each component add up or cancel out? What maximal T_c's will be reached for the mixed system? To answer these questions, Ba(Fe$_{1-y}$Co$_y$)$_2$(As$_{1-x}$P$_x$)$_2$ with $y \sim$ 0.03, 0.05 and 0.07 and varying phosphorus content was prepared and the structural and physical properties investigated.

10.2. Experimental Methods

Fe$_{1-y}$Co$_y$As$_{1-x}$P$_x$ was prepared by heating stoichiometric mixtures of iron, cobalt, arsenic and phosphorus in sealed silica ampoules under an atmosphere of purified argon to 973 K for 10 h, homogenizing and sintering two times at 1123 K for 30 h. A stoichiometric amount of Ba was added, the mixture placed in an alumina crucible, heated to 943 K at a rate of 100 K/h and kept at this temperature for 10 h. The reaction product was homogenized, sintered at 1273 K for 30 h, again homogenized and sintered at 1373 K for another 30 h. For conductivity measurements pellets were cold pressed and sintered at 1273 K for 10 h. Bulk superconductivity was confirmed by AC susceptibility measurements and the superconducting transition temperature extracted by fitting the steepest descent with a line and using the point of intersection with the normal-state susceptibility as T_c (onset). Powder diffraction data was measured using a Huber G670 diffractometer with Co-K$_{\alpha 1}$ or Cu-K$_{\alpha 1}$-radiation, equipped with a closed cycle He

cryostat for low temperature powder diffraction. To check the phase homogeneity and determine the structural parameters Rietveld refinements were performed using the TOPAS package[74]. The fundamental parameter approach was used for the reflection profiles and an empirical 2θ dependent intensity correction for Guinier geometry. The Fe:Co ratio was held constant and the As:P ratio was refined. Both Co and P content were checked by EDX measurements for most samples, revealing variations by no more than 1 % for the Co content and by no more than 2 - 4 % for the P content. In a few samples small percentages of Fe$_2$P were observed, while other contained traces of an unknown foreign phase with main reflection at $2\theta \approx 28$ °, which had also been reported for similar samples[130].

10.3. Results and Discussion

Figure 10.1 shows the variation of the lattice parameters a and c with increasing phosphorus substitution for phosphorus-only doped samples (black)[130] and samples with additional 3 % (blue) or 7 % cobalt (red). For all Co doping levels the lattice parameters decrease with increasing phosphorus substitution, as expected because of the so-called "chemical pressure" by the smaller ionic radius of phosphorus ($r(\text{P}^{3-}) = 166$ pm) compared to arsenic ($r(\text{As}^{3-}) = 176$ pm, see Appendix A.6). Co doping seems to decrease both lattice parameters slightly, but the effect is small compared to the decrease due to phosphorus substitution. Thus all structural parameters are dominated by effects of the phosphorus content and hardly influenced by Co doping.

Although the effect of Co doping on the structure is small compared to phosphorus substitution, a distinct effect of additional Co doping can be observed for the physical properties. Figure 10.2 depicts resistivity versus temperature plots of the series Ba(Fe$_{1-y}$Co$_y$)$_2$(As$_{1-x}$P$_x$)$_2$ with 3 % cobalt doping and $x = 0.07$ - 0.40 while Figure 10.3 presents the results of AC susceptibility measurements confirming bulk superconductivity. 3 % Co doping is just outside the supercon-
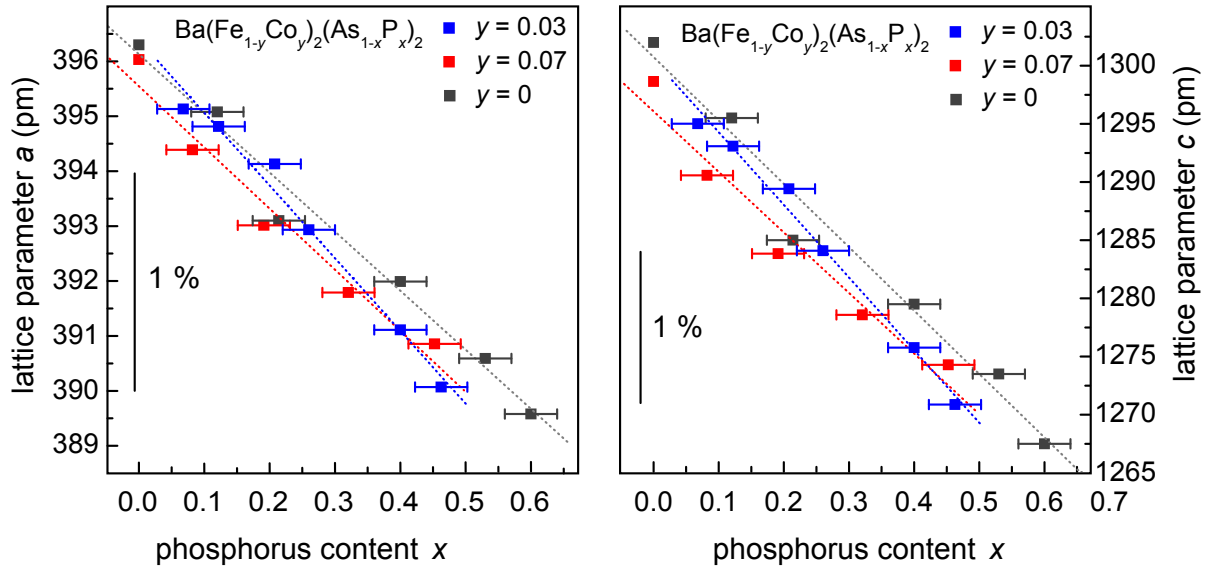
Fig. 10.1.: $Ba(Fe_{1-y}Co_y)_2(As_{1-x}P_x)_2$: lattice parameters a and c (pm) for $y = 0$ (black)[130], y = 0.03 (blue) and y = 0.05 (red).
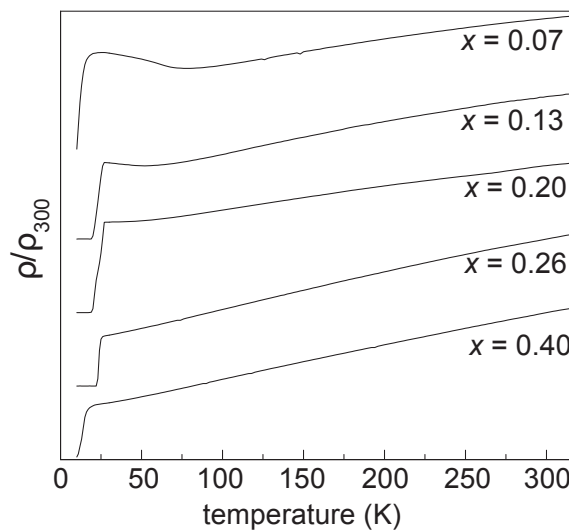
Fig. 10.2.: $Ba(Fe_{0.97}Co_{0.03})_2(As_{1-x}P_x)_2$: Normalized electrical resistances ρ/ρ_{300} for $x = 0.07$ - 0.4.
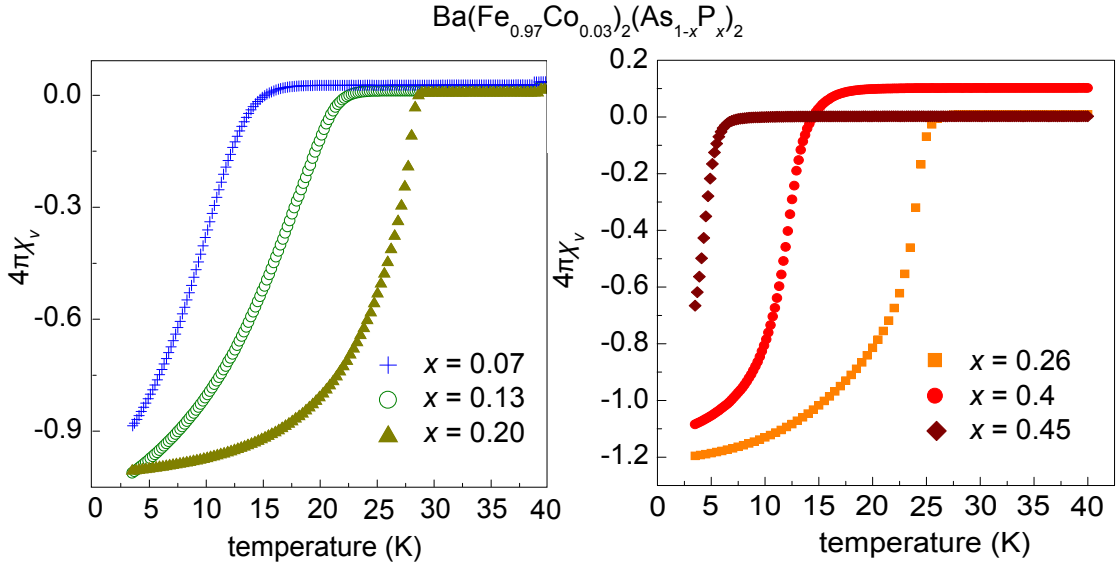
Fig. 10.3.: Ba(Fe$_{0.97}$Co$_{0.03}$)$_2$(As$_{1-x}$P$_x$)$_2$: AC volume susceptibility χ'_v for $x = 0.07$ - 0.20 (blue-green, left) and $x = 0.26$ - 0.45 (orange-red, right).

ducting dome: A superconducting volume fraction of only 3 % and a T_c(onset) = 3 K was observed for 3.15 %, while bulk superconductivity with $T_c = 7$ K was shown for 3.66 % Co[122]. Substituting only 7 % phosphorus for arsenic yields a superconductor with T$_c$= 14 K. EDX measurements show a Co concentration of about 3.22 % for this sample, but even if bulk superconductivity could be expected at this doping level, the transition temperature is much higher than expected for the Co doping alone. Further substitution of arsenic by phosphorus quickly leads to a rise of the superconducting transition temperature to a maximum of 28 K for $x = 0.2$ as shown in Figure 10.3 (left), followed by decreasing critical temperatures of 25 K at $x \approx 0.26$, 15 K at $x \approx 0.4$ and finally 5 K at $x \approx 0.45$ (Figure 10.3 (right)).

Samples with small phosphorus concentrations show resistivity anomalies around 90 K at $x = 0.07$ and 70 K at $x = 0.13$ (Figure 10.2). Reports about underdoped Ba(Fe$_{1-y}$Co$_y$)$_2$As$_2$ link an increase of the resistivity to the SDW-transition[131]. Although the effect is less pronounced here than reported for Ba(Fe$_{1-y}$Co$_y$)$_2$As$_2$ single crystals, low temperature powder diffraction reveals a small splitting of
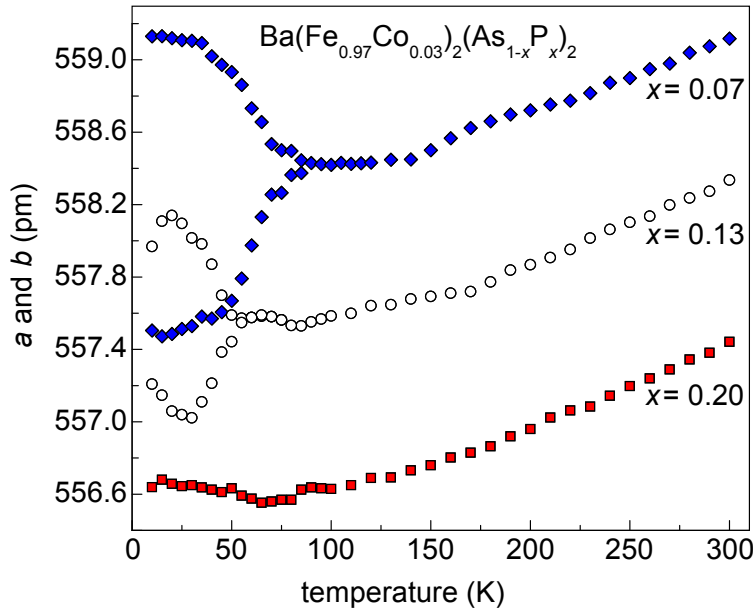
Fig. 10.4.: $Ba(Fe_{0.97}Co_{0.03})_2(As_{1-x}P_x)_2$: temperature dependency of lattice parameters a and b (pm); for $x = 0.07$ and 0.13 orthorombic distortion is observed.

reflections (for example the (110) reflection) for $x = 0.07$ and a broadening of reflections for $x = 0.13$. Figure 10.4 presents the results of rietveld refinements of the low temperature powder data. The splitting of the lattice parameters appears close to 85 K at $x = 0.07$ and near 60 K at $x = 0.13$. Exact determinations of the transition temperatures are difficult due to peak broadening, possible phosphorus inhomogeneities and the smallness of the splitting. At 10 K the orthorhombic lattice parameters differ by 1.6 pm for $x = 0.07$ and by 0.7 pm for $x = 0.13$ compared to 4 pm in $BaFe_2As_2$[8].

Next $Ba(Fe_{1-y}Co_y)_2(As_{1-x}P_x)_2$ samples with the higher Co doping levels $y = 0.05$ and 0.07 were studied, that are already superconducting without phosphorus substitution. Figure 10.5 presents susceptibility (left) and conductivity (right) measurements for $x = 0.16$ - 0.23. A transition temperature of 18 K was reported for $Ba(Fe_{0.95}Co_{0.05})_2As_2$[131] which increases to 24 K by phosphorus substitution at $x = 0.16$ before dropping slightly to 22 K at $x = 0.23$ and to 14.5 K at $x = 0.36$. These effects are similar to those observed for the samples at $y = 0.03$, though less pronounced.
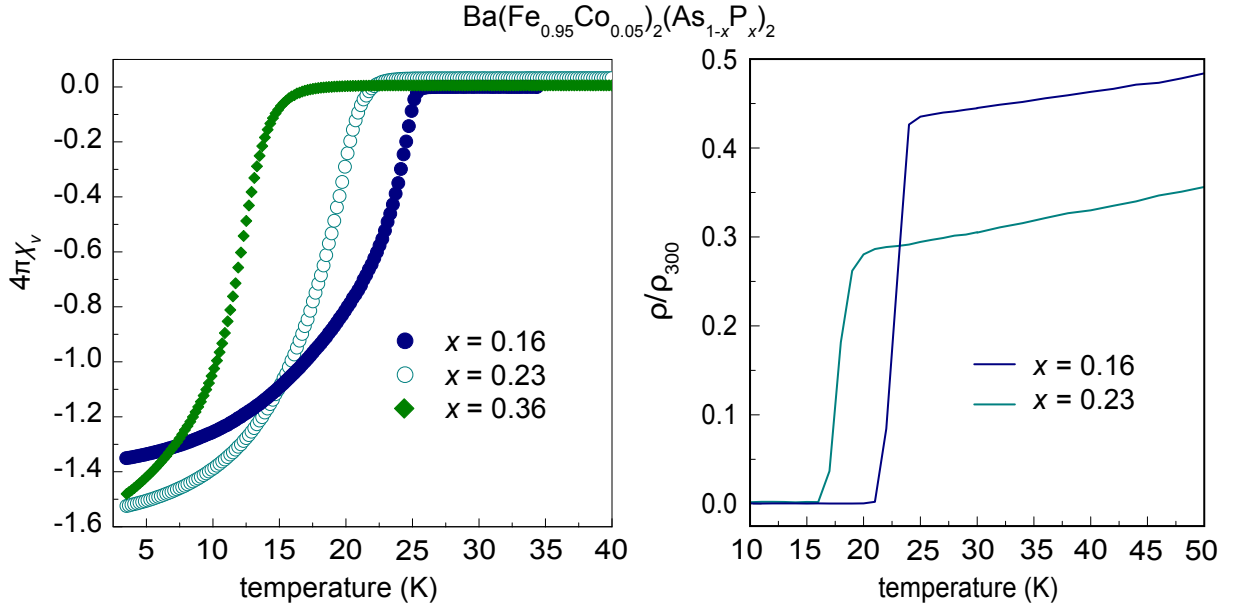
Fig. 10.5.: AC-susceptibility of $Ba(Fe_{0.95}Co_{0.05})_2(As_{1-x}P_x)_2$ with $x = 0.16$, 0.23 and 0.36 (left); relative resistance ρ/ρ_{300} for $x = 0.16$, 0.23 (right).

However once the Co doping level is increased to 7 %, the picture changes. From the normalized electrical resistances depicted in Figure 10.6(a) it becomes immediately clear that for $Ba(Fe_{0.93}Co_{0.07})_2As_2$ additional P substitution only diminishes T_c, until superconductivity is suppressed. This is supported by AC susceptibility measurements that show bulk superconductivity for $x = 0.08$ and $x = 0.20$ ($T_c = 21$ and 13 K) while for $x = 0.32$ only the onset of diamagnetism with a small superconducting volume fraction is detected.

To summarize the results presented so far, we find an increase followed by a decrease of T_c in cobalt-underdoped samples ($y = 0.03$ and 0.05, more pronounced in $y = 0.03$), and a decline of T_c for the optimally doped ($y = 0.07$) compounds upon phosphorus substitution. All data points (black squares) are collected in a phase diagram (Figure 10.7), where T_c is colour-coded: dark red means $T_c \sim 30$ K, yellow $T_c \sim 10$ K and non superconducting areas are depicted in light blue. The data for $Ba(Fe_{1-y}Co_y)_2As_2$ and $BaFe_2(As_{1-x}P_x)_2$ were taken from [121] and [26]. A shift of the whole superconducting dome to lower P contents is observed with
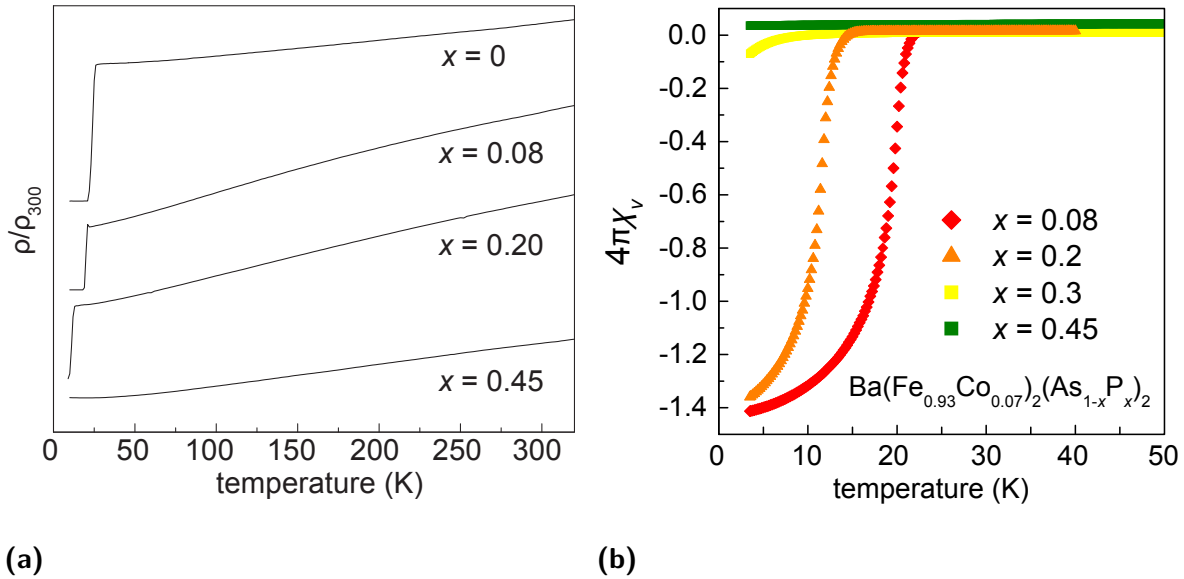
Fig. 10.6.: (a) Normalized electrical resistances ρ/ρ_{300} for $x = 0$ - 0.45. (b) AC-susceptibility of Ba(Fe$_{0.93}$Co$_{0.07}$)$_2$(As$_{1-x}$P$_x$)$_2$ with $x = 0.08$ - 0.45

inreasing Co doping. Co and P doping seem to work together at suppressing the SDW transition, inducing superconductivity and increasing the superconducting transition temperature in the respective underdoped areas, where neither one dopant alone could explain the observed T_c's. However, Co plus P doping can not surpass the maximum T_c of 30 K found for Ba(Fe$_{0.93}$Co$_{0.07}$)$_2$(As$_{1-x}$P$_x$)$_2$ with $x = 0.33$. The results suggest that the maximal transition temperature observed for each Co doping level is shifted along a line connecting $x = 0.33$ (P) and $y = 0.07$ (Co), gradually decreasing from 30 K to 25 K.

Recent ARPES results suggested that phosphorus substitution may act like hole doping in BaFe$_2$(As$_{1-x}$P$_x$)$_2$ with 0.3 holes per iron when one arsenic is replaced by phosphorus at $x = 0.5$[132]. If indeed holes are introduced by phosphorus substitution, the same number of holes and electrons should be present along the dashed line drawn in Figure 10.7. However, the results on Ba$_{1-x}$K$_x$(Fe$_{1-y}$Co$_y$)$_2$As$_2$ presented in chapter 8 show a compensation of hole and electron doping and the recovery of a parent-like phase for low cobalt doping levels[133]. As can be seen
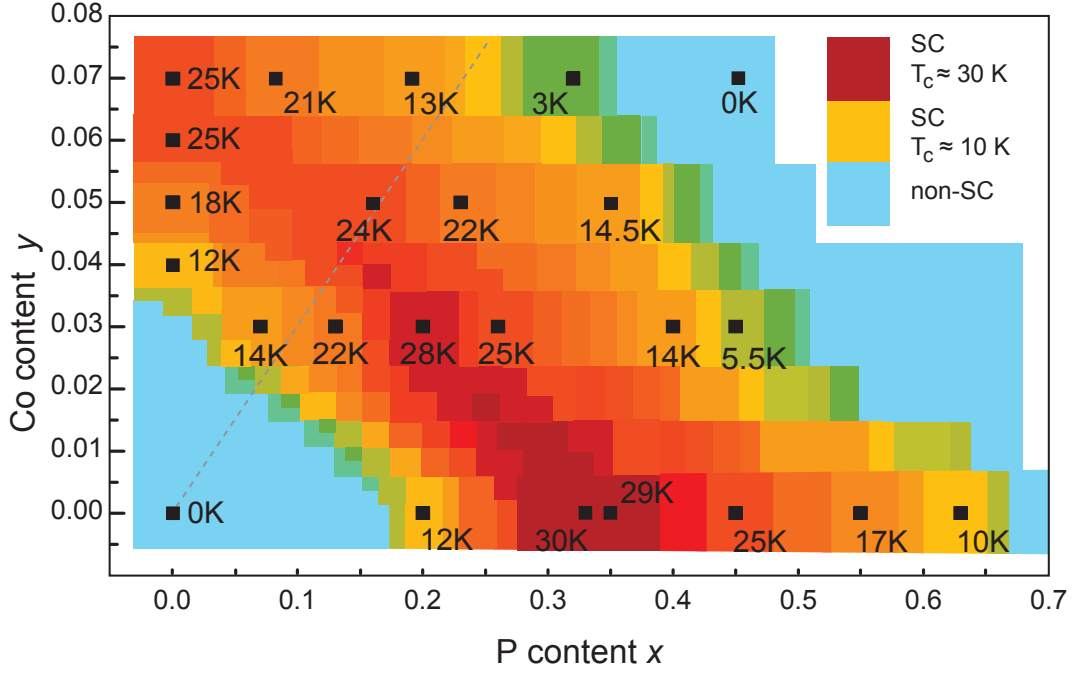
Fig. 10.7.: Phase diagram of $Ba(Fe_{1-y}Co_y)_2(As_{1-x}P_x)_2$, data points in black, T_c colour-coded: T_c $\sim$30 K (dark red), T_c $\sim$10 K (yellow), non superconducting (blue); data for $x = 0$ and $y = 0$ taken from [121] and [26]

from Figure 10.7, no such effect is found for $Ba(Fe_{1-y}Co_y)_2(As_{1-x}P_x)_2$.

Since the structure of $Ba(Fe_{1-y}Co_y)_2(As_{1-x}P_x)_2$ is dominated by the "chemical pressure" generated by phosphorus doping, a comparison to physical pressure suggests itself. Several studies on the effect of pressure on $Ba(Fe_{1-y}Co_y)_2As_2$ report an increase of T_c under pressure on the underdoped side and a small increase and/ or a decrease for optimally doped samples[117,131,134,135]. Especially uniaxial pressure effects seem to have a big influence, for example in the case of $Ba(Fe_{0.92}Co_{0.08})_2As_2$, where T_c rises slightly with increasing pressure under hydrostatic conditions while it is quickly diminished for pressures applied along the c-axis[135]. However, as phosphorus substitution intrinsically provides an uniaxial component[136], our data should agree better with high pressure studies preformed under less hydrostatic pressure conditions. For comparison, the phosphorus content was related to physical pressure via the cell volume (data

for $BaFe_2(As_{1-x}P_x)_2$ from[130], and for pressurized $BaFe_2As_2$ from[137], ratio of changes for c and a similar for both data sets) which gives 1 GPa $\hat{=}$ 13.12 % P. Plots for T_c versus phosphorus content (filled symbols) or physical pressure (open symbols and dashed lines) for different Co doping levels are displayed in Figure 10.8 a) ($y = 0$ (black), $y \approx 0.03$ (blue) and $y \approx 0.07$ (red)). Obviously, the general trend for each Co doping level is the same both for chemical and physical pressure. However, for physical pressure the superconducting domes are broadened, especially for the Co doped samples, and shifted to higher pressures than expected from the relation via volume. It appears as if chemical pressure is more efficient in pushing the system to the maximum T_c, emphasized by the large pressure difference of $\approx$ 3 GPa between $BaFe_2As_2$ under physical pressure and $BaFe_2(As_{1-x}P_x)_2$.

A closer look at the structure helps to understand these discrepancies. While the lattice parameters a and c vary similar under chemical and physical pressure, significant differences are found in the reduction of the Fe-As bond lengths. Figure 10.9 depicts the changes in the normalized Fe-As distances in $BaFe_2(As_{1-x}P_x)_2$ (red)[28] and $BaFe_2As_2$ under pressure (black)[137,139]. While the Fe-As bond in $BaFe_2As_2$ decreases linearly with increasing pressure, the Fe-As bond in $BaFe_2(As_{1-x}P_x)_2$ contracts rather strongly at low phosphorus doping levels and then converges[28].

The shortening of the Fe-As bond length is known to be connected with a broadening of the bandwidth and the suppression of the SDW-state upon P substitution in $BaFe_2(As_{1-x}P_x)_2$. Since also for $BaFe_2As_2$ under pressure, DFT calculations find a decrease of the Fe-As distance (its magnitude well in agreement with the data shown in Figure 10.9), correlated to a decrease of the magnetic moment[140], a similar state might be expected under chemical and physical pressure for similar Fe-As distances. For example in $BaFe_2As_2$ the Fe-As distance has been reduced by $\sim$1.35 % at $\sim$ 5.5 GPa, where $T_{c,max}$ is observed. Equal reduction of the bond is found for $x \approx 0.3$ in $BaFe_2(As_{1-x}P_x)_2$, again close to the
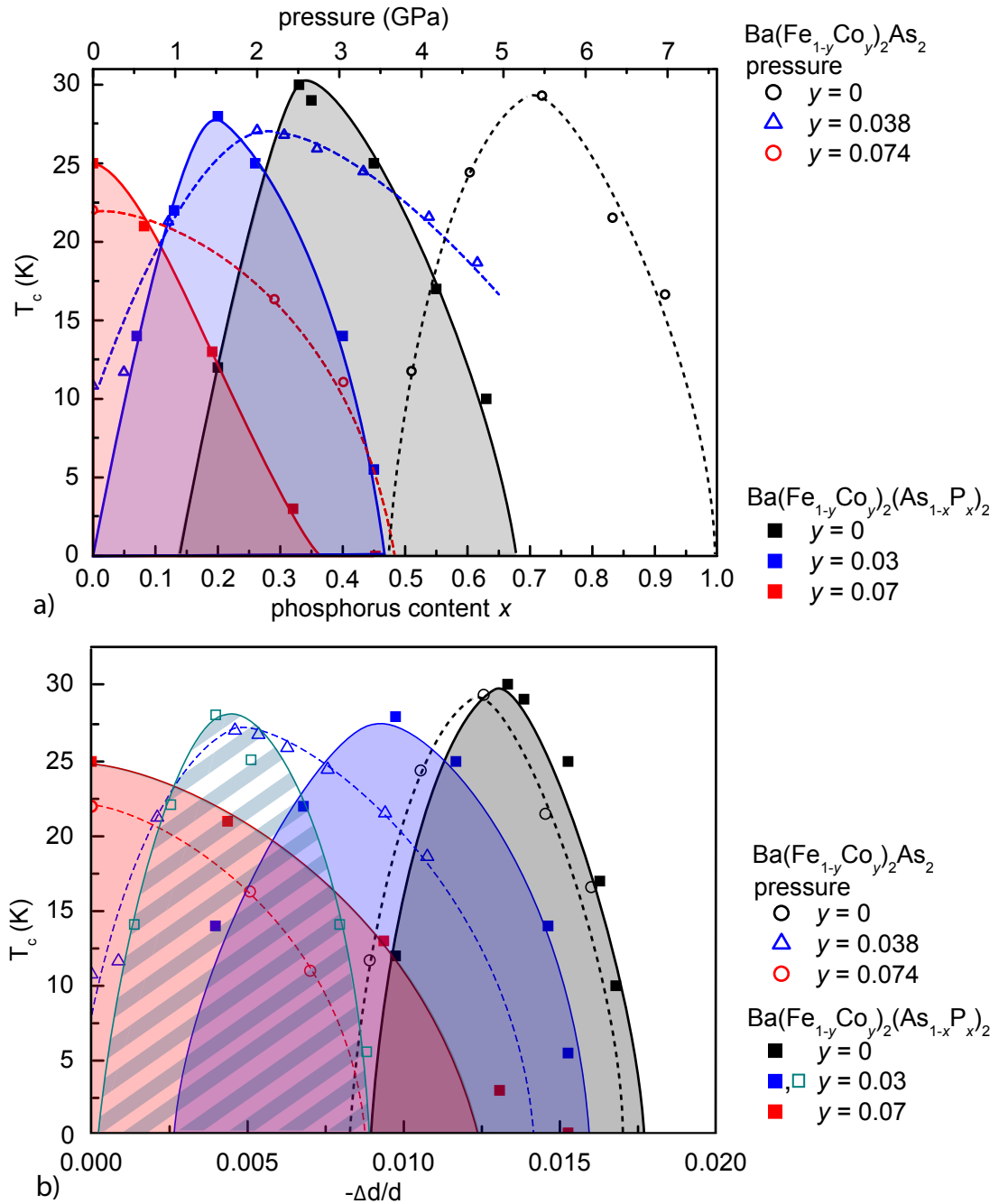
Fig. 10.8.: a) Comparison of the effects of physical pressure on $Ba(Fe_{1-y}Co_y)_2As_2$ and chemical pressure in $Ba(Fe_{1-y}Co_y)_2(As_{1-x}P_x)_2$; continuous lines, filled symbols and regions: $Ba(Fe_{1-y}Co_y)_2(As_{1-x}P_x)_2$ with $y = 0$ (black), $y = 0.03$ (blue) and $y = 0.07$ (red). open symbols and dashed lines: $Ba(Fe_{1-y}Co_y)_2As_2$, physical pressure: $y = 0$ (black)[138], $y = 0.038$ (blue) and $y = 0.074$ (red)[134]. b) plot of the same data relative to the change of the Fe-As distances taken from 10.9, cyan open symbols and banded dome: assumption of the linear decrease of the Fe-As bond length (as observed for physical pressure) for $Ba(Fe_{1-y}Co_y)_2(As_{1-x}P_x)_2$, $y = 0.03$.
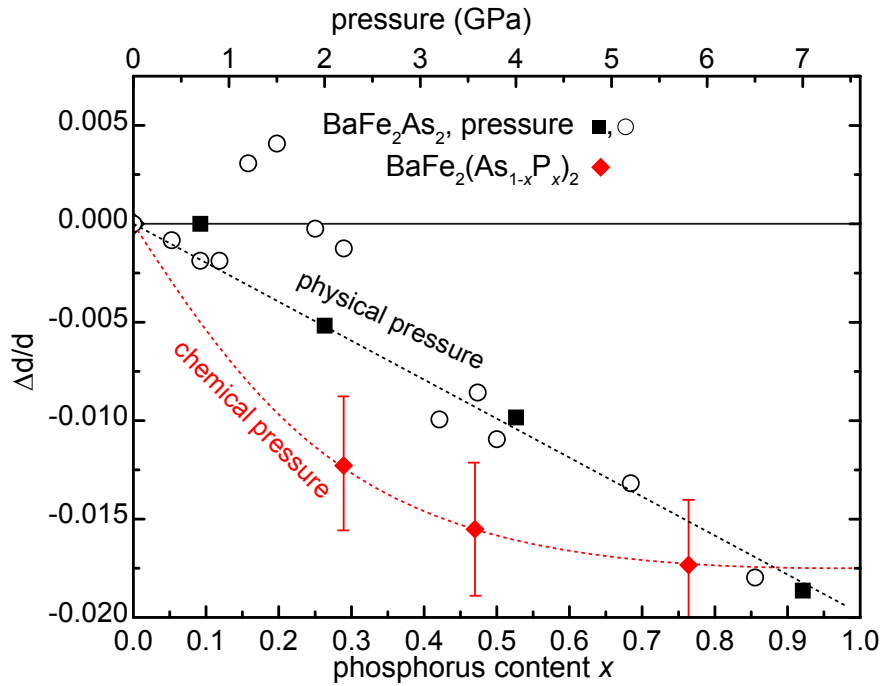
Fig. 10.9.: changes in the normalized Fe-As bond length in BaFe$_2$(As$_{1-x}$P$_x$)$_2$ [28] (red) and BaFe$_2$As$_2$ under pressure (black [137,139], lines as guide to the eye, chemical pressure related to physical pressure via cell volume.

maximum of the superconducting dome. Figure 10.8 b) shows a plot of T_c versus the changes in the normalized Fe-As distance for the data depicted in a), where a qualitative correlation of phosphorus content and physical pressure to the Fe-As distances was done by using the dashed lines in Figure 10.9. This shows very good agreement for BaFe$_2$As$_2$ under physical pressure and chemical pressure in BaFe$_2$(As$_{1-x}$P$_x$)$_2$, indicating that, regardless of chemical or physical pressure, the Fe-As bond length is the crucial factor that controls T_c if no Co doping is present.

For the Co underdoped sample ($y = 0.03$) the maximal T_c values for chemical and physical pressure coincide at the same value $-\Delta d/d \approx 0.005$ (green banded dome in Figure 10.8b) only if a linear bond shortening with phosphorus substitution is anticipated in both cases. This assumes that the steeper decrease of $-\Delta d/d$ at lower phosphorus concentrations (figure 10.9) is due to the suppression of the magnetism, which would be already weakened in the case of Co doping.

If it is alternatively anticipated that the bond length curve for chemical pressure is equally valid for the Co doped sample, the maximum T_c for chemical pressure is shifted to $-\Delta d/d \approx 0.01$ (blue filled dome in Figure 10.8b), but the shape of the dome is now more similar to that for physical pressure. A shift of the $T_{c,max}$ value for chemical pressure (filled blue) to higher $-\Delta d/d$ relative to $T_{c,max}$ for physical pressure (dashed blue) is expected due to the slightly different lower Co concentrations (chemical pressure: $y = 0.03$, physical pressure $y = 0.038$). However, the observed shift is bigger than estimated by assuming a linear dependency $-\Delta d/d(T_{c,max})$, but a more concrete analysis is still not possible due to the lack of sufficiently precise structural data.

10.4. Conclusion

In this chapter, the effects of simultaneous doping with cobalt and phosphorus $Ba(Fe_{1-y}Co_y)_2(As_{1-x}P_x)_2$ were studied and a detailed phase diagram was presented. The spin density wave can be suppressed and superconductivity induced by a combination of both dopants in such areas where the content of only one would not suffice, but a combination of both can also drive the system from the optimally doped to an overdoped state. The maximum T_c is not in the Co plus P doped area of the phase diagram, but occurs in $BaFe_2(As_{1-x}P_x)_2$ at $x = 0.33$. The phase diagram gives no evidence of holes in $BaFe_2(As_{1-x}P_x)_2$ as suggested by recent angle resoled photoemission experiments. Chemical and physical pressure act similarly in $Ba(Fe_{1-y}Co_y)_2As_2$, but the data strongly suggest that the most important parameter is the length of the Fe-As bond and not the unit cell volume. The different behaviour of the Fe-As distance under physical pressure (where a linear decrease is found) and in $BaFe_2(As_{1-x}P_x)_2$ (non-linear reduction) is the key to understanding the differences between physical and chemical pressure. The properties of both $Ba(Fe_{1-y}Co_y)_2(As_{1-x}P_x)_2$ and $Ba(Fe_{1-y}Co_y)_2As_2$ under physical pressure seem to be mainly controlled by two parameters: the

charge introduced by Co doping, which changes the filling of bands, and the FeAs distance that influences bandwidth and magnetism.

11. Summary

In this thesis, structure and properties of $ThCr_2Si_2$-type and related materials were investigated. The main focus was on the 122-phases of iron arsenide superconductors, more precisely on doped $BaFe_2As_2$. The structural details of $Ba_{1-x}K_xFe_2As_2$ at low temperatures were examined and several substitution series of $BaFe_2As_2$ were synthesized to study the influence of combinations of doping both on structure and properties. Apart from the iron arsenides, ternary rhodium arsenides with $ThCr_2Si_2$-type and related structures were studied in detail. The following chapter gives a brief summary of the key results presented in this thesis.

SrRh$_2$As$_2$

At first sight, $SrRh_2As_2$ seems to have similar properties as $BaFe_2As_2$, since both compounds undergo a similar tetragonal to orthorhombic phase transition. On closer inspection however, the similarities quickly end; in contrast to $BaFe_2As_2$, which is antiferromagnetic below the phase transition, $SrRh_2As_2$ turned out to be a Pauli-paramagnet. Additionally, it shows a richer structural chemistry, with the tetragonal γ-$SrRh_2As_2$ transforming to β-$SrRh_2As_2$ at 555 K and to α-$SrRh_2As_2$ at 463 K. For this work, single crystals and powder samples of $SrRh_2As_2$ were prepared and the structures of all three polymorphs were studied in detail. Despite the partially pseudo merohedric twinning, the so far unknown crystal structure of α-$SrRh_2As_2$ could be solved in the monoclinic space group $P2_1/c$ with $a = 421.2(1)$ pm, $b = 1105.6(2)$ pm, $c = 843.0(1)$ pm and $\beta = 95$ °. For β-$SrRh_2As_2$, a close inspection of the diffraction pattern revealed satellite reflections in agreement with a modulation vector $\mathbf{q} = (0.5, 0, 0.1655)$, where second order

satellites were much stronger than the first order satellites. Taking the strong satellites into account, the incommensurate structure was successfully refined in the (3+1) dimensional superspace group $Fmmm(10\gamma)\sigma00$ with the unit cell parameters $a = 1114.4(3)$ pm, $b = 574.4(2)$ pm and $c = 611.5(2)$ pm and a modulation vector $\mathbf{q} = (1, 0, 0.3311(4))$. The strong modulation of the Rh atom can be described by a crenel function and leads to a variation of the Rh-Rh distances along c from 287 pm to 358 pm. For the γ-phase, the presented high temperature single crystal data confirms the ThCr$_2$Si$_2$-type structure of γ-SrRh$_2$As$_2$ as reported in literature. Furthermore, DFT calculations with COHP bonding analysis show that the distortion and elongation of Rh-Rh bonds lead to lowering in energy of antibonding states in α-SrRh$_2$As$_2$ compared to tetragonal γ-SrRh$_2$As$_2$, thus the driving force of the lattice distortions comes from Rh-Rh bonding and has no magnetic origin as suggested for BaFe$_2$As$_2$.

CaRh$_2$As$_2$ and Sr$_{1-x}$Ca$_x$Rh$_2$As$_2$

The study of ternary rhodium arsenides also lead to the discovery of the new compound CaRh$_2$As$_2$. CaRh$_2$As$_2$ crystallizes in the ThCr$_2$Si$_2$-type structure, space group $I4/mmm$ with $a = 415.0(6)$ pm and $c = 1023(2)$ pm. With a distance of only 258 pm separating the arsenic atoms of neighbouring RhAs$_{4/4}$-layers, As-As bonding exists in CaRh$_2$As$_2$, in contrast to the other alkaline earth rhodium arsenides. CaRh$_2$As$_2$ is a Pauli-paramagnetic metal, and - contrary to SrRh$_2$As$_2$ - it undergoes no phase transitions. To find out how the structure and phase transitions in SrRh$_2$As$_2$ are influenced by a substitution of Sr for the smaller Ca, the solid solution Sr$_{1-x}$Ca$_x$Rh$_2$As$_2$ was prepared. For $x = 0.05$, the α-phase is stable at room temperature, replaced by the orthorhombic (and incommensurately modulated) β-phase for $0.2 \leq x \leq 0.6$ and the tetragonal (ThCr$_2$Si$_2$-type) γ-phase for $x \geq 0.8$. Due to the occurrence of the three different structure types, the lattice parameters show a non-linear variation with increasing Ca content. With the stabilization of the tetragonal phase, the interlayer As-As distance is

significantly reduced to 265 pm, enabling As-As bonding. For the modulated β-phase, the "chemical pressure" by Ca substitution influences both the **q**-vector and the amplitude of the modulation, thus decreasing the distortion within the $RhAs_{4/4}$-layer.

$Ba_{1-x}K_xFe_2As_2$

A special effort was made to gather detailed structural information on superconducting $Ba_{1-x}K_xFe_2As_2$ at low temperatures. High quality single crystals of $Ba_{1-x}K_xFe_2As_2$ ($x = 0$ - 0.43) were successfully prepared and studied with low temperature single crystal diffraction at the beamline ID11 (ESRF). A splitting of reflections in agreement with the low temperature orthorhombic phase is observed for $x < 0.24$. Although the orthorhombic distortion and thus the splitting is very small, for $Ba_{0.845}K_{0.155}Fe_2As_2$ separate reflections were recorded at high scattering angles. In agreement with literature[89], the diffraction pattern can be explained by four twin domains, that originate from the loss of the four-fold rotational symmetry and the $(100)_T$ mirror plane during the tetragonal to orthorhombic phase transition.

A determination of the splitting angle φ allows an estimation of the b/a ratio for $Ba_{0.82}K_{0.18}Fe_2As_2$. In combination with an integration using the tetragonal unit cell (split reflections were integrated together) this permits an estimation of the orthorhombic cell parameters and a complete structure refinement. The structural parameters determined with this first single crystal refinement in the low temperature orthorhombic phase agree well with results from powder data[98].

For $Ba_{0.57}K_{0.43}Fe_2As_2$ (phase transition suppressed completely, thus tetragonal at low temperatures), the structural parameters are found to vary less than 0.05 % from 14 to 55 K. No distinct anomalies or changes of structural parameters around T_c are observed. It can be concluded that if structural changes or anomalies occur close to the superconducting transition temperature, they are very small and probably not accessible within the resolution of X-ray experiments.

Furthermore, a study of the local structure of $Ba_{1-x}K_xFe_2As_2$ was carried out. High quality x-ray data of polycristalline samples of $Ba_{1-x}K_xFe_2As_2$ (x=0 - 0.34) were collected at ID 31 (ESRF). Analysis of the pair distribution function showed that for $Ba_{1-x}K_xFe_2As_2$, no significant structure deviations exist on the local scale. This is in contrast to $Ba(Fe_{1-y}Co_y)_2As_2$, where PDF studies revealed local distortions that introduce disorder[125].

$Ba_{1-x}K_x(Fe_{1-y}Co_y)_2As_2$ and $K(Fe_{1-y}Co_y)_2As_2$

It is well known that $BaFe_2As_2$ becomes superconducting both by substitution of Ba by K (hole doping) and Fe by Co (electron doping). Within the scope of this work, the effects of a combination of both types of doping (electron + hole doping) were studied in detail. Three substitution series with different degrees of hole and electron doping were prepared and investigated: $Ba_{1-x}K_xFe_{1.86}Co_{0.14}As_2$, $Ba_{1-x}K_x(Fe_{1-y}Co_y)_2As_2$ $(x/2 = y)$ and $K(Fe_{1-y}Co_y)_2As_2$. A new synthesis route via the mixed iron cobalt arsenides $Fe_{1-y}Co_yAs$, developed in this thesis, permitted the synthesis of homogeneous samples.

The effect of a small electron dopig level in combination with additional hole doping was examined with the solid solution $Ba_{1-x}K_xFe_{1.86}Co_{0.14}As_2$. With increasing potassium content x, $Ba_{1-x}K_xFe_{1.86}Co_{0.14}As_2$ is tuned from electron to hole doping, and the properties evolve from superconductivity to a magnetic state and back to superconductivity, as evidenced by resistance, susceptibility and Mößbauer measurements and low temperature powder diffraction. The recovery of the magnetic phase similar to that of the parent compound is unprecedented. It shows that the effects of hole and electron doping can compensate each other and the emergence of superconductivity is controlled by the concentration of the remaining charge. On the other hand, the crystal structures of $Ba_{1-x}K_xFe_{1.86}Co_{0.14}As_2$ are dominated by the potassium content and are hardly influenced by the 7 % Co substitution, which means that structural effects can not explain the differences to the phase diagram of $Ba_{1-x}K_xFe_2As_2$. These fasci-

nating results emphasize the role of the layer charge and suggest that structural parameters like bond length or angles play a minor role with respect to the incurrence of superconductivity in electron- or hole doped systems, although they seem to be important to achieve the highest possible critical temperatures.

To investigate whether the recovered magnetic state in the charge compensated case remains stable for all doping levels, $Ba_{1-x}K_x(Fe_{1-y}Co_y)_2As_2$ with $0 \leq x/2 = y \leq 0.25$ was synthesized. The magnetic and non-superconducting state was found to exist up to $x/2 = y < 0.13$. Low temperature powder diffraction and Mößbauer experiments show a decrease of the transition temperatures as well as the orthorhombic distortion and the magnetic hyperfine field splitting with increasing $x/2 = y$, which shows the SDW is gradually suppressed. For $0.13 \leq x/2 = y \leq 0.19$, bulk superconductivity with a maximum T_c of 15 K is observed in agreement with[119]. Again, the structural changes do not help to explain the emergence of superconductivity. The additional Co doping slows the increase of the lattice parameter c due to potassium doping and causes a ~ 1 % decrease of the Fe-As distance at $y = 0.25$.

A comparison of the phase diagram of $Ba_{1-x}K_x(Fe_{1-y}Co_y)_2As_2$ ($x/2 = y$) to that of $Ba(Fe_{1-y}Ru_y)_2As_2$ suggests that despite the (in sum) isoelectronic doping in both cases, a different mechanism is responsible for the suppression of magnetism and the appearence of superconductivity. For $Ba_{1-x}K_x(Fe_{1-y}Co_y)_2As_2$, the explanation may be the disorder introduced by the Co substitution, because Co has been shown to introduce structural disorder on the local scale[125] and doping acting as disorder might explain a phase diagram as the one observed[126].

Synthesis and characterization of $K(Fe_{1-y}Co_y)_2As_2$ completed the detailed investigation of combined hole and electron doping presented in this work with an exploration of the potassium rich side. DFT calculations on $KFeCoAs_2$ had shown a Fermi surface similar to that of $BaFe_2As_2$[110], suggesting a state close to a spin density wave instability, although a reduced tendency towards magnetism was reported. However, consistent with the observations for $Ba_{1-x}K_x(Fe_{1-y}Co_y)_2As_2$

$(x/2 = y)$ which show the suppression of the spin density wave, neither resistivity nor magnetic measurements of $K(Fe_{1-y}Co_y)_2As_2$ give a hint for a spin density wave anomaly. With the exception of KFe_2As_2, no superconductivity is found. The convex curvature of the resistivity observed for KFe_2As_2 gives way to an almost linear temperature dependence for $y > 0.5$. The Co-rich endpoint of the series, KCo_2As_2, is a Pauli-paramagnetic metal. The absence of high temperature superconductivity in $K(Fe_{1-y}Co_y)_2As_2$ again emphasizes the importance of magnetism and the proximity to a SDW for the superconductivity in iron arsenides.

$Ba(Fe_{1-y}Co_y)_2(As_{1-x}P_x)_2$

To study the effects of simultaneous isoelectronic and electron doping, the solid solution $Ba(Fe_{1-y}Co_y)_2(As_{1-x}P_x)_2$ was prepared. Polycrystalline samples with y = 0.03, 0.05 and 0.07 and x = 0 - 0.45 were successfully synthesized and characterized, which permitted the assembly of a detailed Co/P dependent phase diagram. Intriguingly, the effects of isoelectronic and electron doping are found to add up, since the suppression of the SDW as well as the occurrence of superconductivity are found at smaller Co and P concentrations than in $Ba(Fe_{1-y}Co_y)_2As_2$ and $BaFe_2(As_{1-x}P_x)_2$. Also the maximum T_c and the decrease of T_c on the overdoped side are shifted to lower Co or P contents. However, simultaneous Co and P doping cannot surpass the maximum transition temperature of 30 K found for $BaFe_2(As_{1-x}P_x)_2$ at x = 0.33. A qualitative comparison of $Ba(Fe_{1-y}Co_y)_2As_2$ and additional P doping (chemical pressure) with $Ba(Fe_{1-y}Co_y)_2As_2$ under physical pressure shows similarities, but a relation of both phase diagrams via the unit cell volume gives unconvincing results. As a closer look reveales, the key for understanding these differences lies in the different behaviour of the Fe-As distance under physical pressure (linear decrease) and chemical pressure (nonlinear reduction). For both $BaFe_2(As_{1-x}P_x)_2$ and $BaFe_2As_2$ under pressure, the Fe-As distance had been reported to be correlated to the magnetic mo-

ment[98,140]. The results presented in this thesis show that a relation of the phase diagrams of $Ba(Fe_{1-y}Co_y)_2As_2$ under physical and chemical pressure via the Fe-As distance gives a much better agreement, identifying the Fe-As distance as the key structural parameter linked to the magnetism. The properties of both $Ba(Fe_{1-y}Co_y)_2(As_{1-x}P_x)_2$ and $Ba(Fe_{1-y}Co_y)_2As_2$ under physical pressure seem to be controlled mainly by two parameters: the charge introduced by Co doping, which changes the filling of bands, and the Fe-As distance that influences bandwidth and magnetism. Both parameters work together in the suppression of the spin density wave and tune the superconducting properties.

Conclusion

From the results of this thesis, several conclusions concerning iron arsenide superconductors can be drawn or strengthened. Firstly, magnetism – more exactly the proximity to a spin density wave (SDW) – seems to be essential to enable high temperature superconductivity. Secondly, this magnetism must be weakened to a certain degree to allow the emergence of superconductivity, which is possible in (at least) three different ways: change of the "effective" charge, introduction of disorder or "pressure" (causing a decrease of the Fe-As distance). If several of these tools are applied, the effects add up in the suppression of the SDW, hastening the appearence of superconductivity, but also the decrease of T_c due to "overdoping". Thirdly, so far the T_c's achieved with a combination of doping could not surpass the T_c's achieved with the doping component with the higher T_c alone. The highest T_c's appear beyond (but close to) the point, where the SDW is completely suppressed. This is the case even if the structure is closer to an ideally tetrahedral $FeAs_{4/4}$ at another doping concentration. Although it cannot be ruled out that high T_c's are favoured by a close to ideal tetrahedra geometry, such a geometry alone is not enough to enable high T_c's or even superconductivity if the (right) proximity to a SDW is wanting. The changes of the structural parameters are only relevant for the emergence of superconductivity if

they are coupled to the magnetic properties, as is the case for the Fe-As distance.

While the suppression of the spin density wave by two of the "tools" named above – disorder and "pressure" – is fairly well understood, it remains a mystery why charge doping works. The results of this thesis strongly suggest that indeed the extra charge and not structural changes are responsible for the suppression of the magnetism and the emergence of superconductivity in the case of K and Co doping in $BaFe_2As_2$. However, since the iron arsenides are metallic, the charges should not remain localized. This raises the question, how such small changes of the band filling (for example as caused by only 4% of Co doping) can have such a strong influence on the physical properties. It is up to future research efforts to shed light on this matter – and this is not the only open question concerning iron arsenide superconductors. Understanding the high temperature superconductivity in iron pnictides remains a challenge, even after the tremendous research progress of the last four years.

A. Appendix

A.1. Crystallographic data of $Sr_{1-x}Ba_xRh_2As_2$

Table A.1.: Crystallographic data of $Sr_{1-x}Ba_xRh_2As_2$

Crystal system, space group		Monoclinic, P $2_1/c$, No. 14		
a, b, c (pm)		423.97(6), 1116.6(2), 843.3(1)		
$\beta°$		95.06(2)		
Cell volume (nm^3)		0.3977(2)		
Calculated density (g/cm^3), Z		7.82, 4		
Radiation type, λ (Å)		Mo-Kα, 0.71073		
2θ range		3.65 - 29.95		
Total number of reflections		5213		
Reflections with $I > 2\sigma(I)$, R_σ		3459, 0.0887		
Refined parameters, Goodness-of-fit on F^2		47, 0.992		
R_1, $wR2$ ($I > 2\sigma(I)$)		0.083, 0.1815		
R_1, $wR2$ (all data)		0.1165, 0.2003		
Largest residual peak, hole $e^-/Å^3$		3.832, -3.662		
Twin fraction		72 %		
Atomic parameters:				
	x	y	z	U_{eq}
Sr	4e	0.24935(2)	0.75362(6)	0.13454(9)	0.01181(13)
Rh1	4e	0.2232(2)	0.50668(5)	0.38101(7)	0.0121(1)
Rh2	4e	0.3114(2)	0.00963(6)	0.35233(7)	0.0123(1)
As1	4e	0.18507(2)	0.40816(8)	0.1118(1)	0.0125(2)
As2	4e	0.27697(2)	0.12244(7)	0.1105(1)	0.0125(2)

As the crystal of $Sr_{1-x}Ba_xRh_2As_2$ is a partial merohedral twin, a .hklf5 file, where no absoption correction had been applied and the reflections were not

merged was used for the structure refinement. The barium content on the strontium site could not be refined (probably due to the missing absorption correction), but the lattice parameters clearly show Ba was incorporated into the structure. The best refinement results were obtained in the monoclinic space group P $2_1/c$.

A.2. Temperature calibration for single crystal experiments at ID11

A helijet was used for low temperature single crystal diffraction at ID11. For the temperature calibration a powder sample of $TbAsO_4$ was used. $TbAsO_4$ undergoes a phase transition from tetragonal $I4_1/amd$ ($a = 709$ pm, $c = 632$ pm) to orthorhombic $Fddd$ ($a = 1008$ pm, $b = 995.7$ pm, $c = 632$ pm) at 26 K[141–143]. The powder was prepared on a fine mesh and measured at ID11 with the same setup as the single crystals. The data was transformed to powder diffractogramms and refined with the Topas suite of programs[74] where a full Voigt function was used to describe the peak shape (appendix A.3). For comparison, the measurement was repeated on a Huber G670 diffractometer (Co-Kα_1) with guinier geometry, equipped with a closed cycle He-cryostat and calibrated with $DyVO_4$. The Co data was refined with the Topas suite of programs[74] using the fundamental parameter approach. Careful inspection of the diffraction pattern revealed that even at 10 K the phase transition has not taken place completely and about 25-30 % of the sample remains in the tetragonal phase. Thus both tetragonal and orthorhombic phase were included in the rietveld refinement. The refinement results are shown in figure A.1. The Co data is depicted in red and the data collected at ID11 in black. Apart from a small offset of the lattice parameters, probably due to calibration differences, both datasets agree reasonably well if the synchrotron data is shifted to lower temperatures by 5 K. This shows the temperature measured by the helijet must have been approximately 5 K lower than displayed. Contrary to literature results[141] (gray lines in figure A.1), no

rapid narrowing of the orthorhombic distortion with $a = b$ at 26 K is found. This might be due to the broadness of reflections, that are probably better described by a combination of reflections in the rietveld refinement. Another explanation might be a hysteresis of the phase transition as mentioned in literature, its width varying with different sample preparation[141].
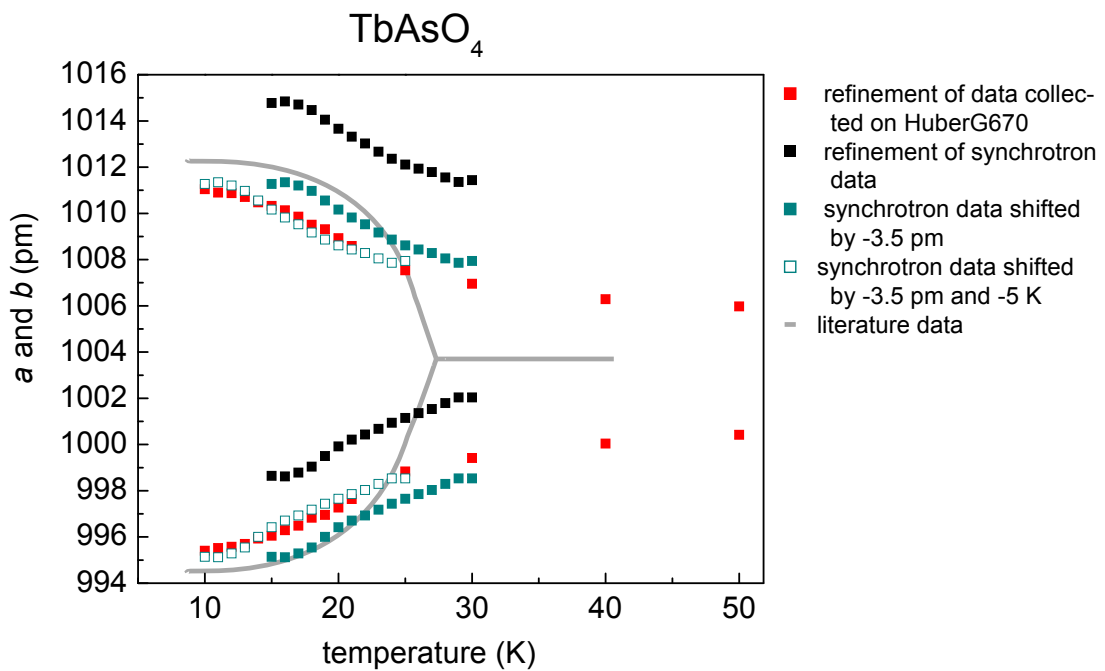
Fig. A.1.: Lattice parameters of the orthorhombic cell of TbAsO$_4$; rietveld refinement of lab data (red) and of synchrotron data (black, temperature as given by the temperature control of the Helijet), synchrotron data shifted by -3.5 pm for better comparison (cyan, filled symbols) and by -3.5 pm and 5 K (cyan, open symbol), literature data (gray line)[141].

A.3. Peak shape for rietveld refinement of synchrotron data

For rietveld refinements of the synchrotron radiation data measured at ID 31, the following function [*] was used to describe the peak shape (all parameters were refined freely).

prm pr1 0.00676' min 0
prm pr2 0.00682' min 0
prm pr3 0.00731' min 0
prm pr4 0.00809' min 0

lor_fwhm = pr1 Tan(Th) + pr2/Cos(Th) ;
gauss_fwhm = pr3 Tan(Th) + pr4/Cos(Th) ;

[*] from *http://www.dur.ac.uk/john.evans/topas_workshop/tutorial_synchy2o3.htm*

A.4. Rietveld refinement data of K(Fe$_{1-y}$Co$_y$)$_2$As$_2$

Table A.2.: Rietveld refinement data of K(Fe$_{1-y}$Co$_y$)$_2$As$_2$

Composition	Structural parameters		
y(Co)	a	c	z(As)
0	3.8414	13.839	0.3525
0.07	3.84069	13.82656	0.35221
0.1	3.83857(3)	13.8253(2)	0.35203(9)
0.2	3.83539(3)	13.7676(2)	0.35146(9)
0.3	3.8333(2)	13.7279(2)	0.35022(7)
0.4	3.83005(4)	13.6858(3)	0.35006(12)
0.5	3.8274(3)	13.6615(2)	0.34926(8)
0.6	3.82479(3)	13.6256(2)	0.34916(8)
0.7	3.81679(3)	13.6063(2)	0.34868(8)
0.8	3.81068(3)	13.5974(2)	0.34923(8)
0.9	3.80813(3)	13.5763(2)	0.34901(10)
1	3.80667	13.56047	0.34788

A.5. EDX and rietveld refinement data of $Ba_{1-x}K_xFe_{1.86}Co_{0.14}As_2$
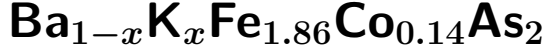
Table A.3.: EDX and rietveld refinement data of $Ba_{1-x}K_x(Fe_{1-y}Co_y)_2As_2$

Composition (EDX)		Structural parameters from rietveld refinements			
$x(K)$	$y(Co)$	$x(K)$	a	c	$z(As)$
0	0.069 ± 0.008	0	3.96031(3)	12.9865(13)	0.35370(8)
0.055 ± 0.02	0.076 ± 0.005	0.077(4)	3.95256(4)	13.00822(19)	0.35319(9)
0.132 ± 0.009	0.078 ± 0.007	0.126(4)	3.94224(3)	13.06619(14)	0.35365(8)
0.20 ± 0.02	0.074 ± 0.007	0.206(3)	3.93584(2)	13.13093(13)	0.35353(8)
0.26 ± 0.01	0.075 ± 0.002	0.278(4)	3.92669(9)	13.17179(26)	0.35322(15)
0.36 ± 0.04	0.075 ± 0.004	0.365(6)	3.91761(8)	13.24684(42)	0.35310(16)
0.43 ± 0.03	0.075 ± 0.004	0.449(3)	3.90286(4)	13.31763(24)	0.35354(8)
0.50 ± 0.04	0.069 ± 0.004	0.549(3)	3.89531(5)	13.39320(26)	0.35351(9)
-	-	0.685(2)	3.87933(4)	13.50853(25)	0.35323(7)
0.77 ± 0.04	0.064 ± 0.009	0.764(2)	3.87041(3)	13.59190(22)	0.35329(7)
-	-	0.917(2)	3.85468(6)	13.75556(45)	0.35381(11)
1	0.073 ± 0.003	1	3.84069(2)	13.82656(15)	0.35221(7)

A.6. Calculation of the ionic radius of As^{3-} and P^{3-}

The ionic radius of As^{3-} and P^{3-} was calculated from the shortest $M - X$ distance in the compounds $M_4X_{2.6}$ ($M =$ Ba, Eu and $X =$ As, P)[144–146]. The effective ionic radius (Shannon) of Ba^{2+} and Eu^{2+} was used[147]. The result (after averaging the values for the europium and barium compounds) is 176 pm for the ionic radius of As^{3-} and 166 pm for P^{3-}.

Table A.4.: Bonding distances and ionic radius

compound	$M - X$ distance (pm)	calculated ionic radius of X^{3-} (pm)
$Ba_4As_{2.6}$	329.26	180.26
$Eu_4As_{2.67}$	303.64	172.64
$Ba_4P_{2.67}$	318.87	169.05
$Eu_4P_{2.67}$	295.32	164.32

A.7. Synthesis and structure of Sr$_5$As$_4$

Sr$_5$As$_4$ was first obtained as impurity phase during the synthesis of ternary stron-
tium chromium arsenide. It can be synthesized by heating stoichiometric mix-
tures of Sr and As in an alumina crucible sealed in a silica ampoule under an
atmosphere of purified argon to 1273 K and keeping the temperature for 10 h.
After 1-2 annealing steps (10 h at 1273 K), a metallic reaction product, sensitive
to air and moisture, is obtained.

Table A.5.: Crystallographic data of Sr$_5$As$_4$

Crystal system, space group	Orthorhombic, *Cmce*, No. 64
a, b, c (pm)	1610.7(2), 813.3(3), 816.29(18)
Cell volume (nm^3)	1.0693(5)
Molar mass	737.8
Temperature (K)	293
Calculated density (g/cm^3), Z	4.583, 4
Radiation type, λ (Å)	Mo-Kα, 0.71073
2θ range	4.6 - 60.9
Transmission (min, max)	0.0778, 0.1730
Absorption coefficent (mm^{-1})	36.96
Total number of reflections	5595
Independent reflections, R_{int}	832, 0.1002
Reflections with $I > 2\sigma(I)$, R_σ	540, 0.0754
Refined parameters, Goodness-of-fit on F^2	25, 0.736
R_1, $wR2$ ($I > 2\sigma(I)$)	0.0478, 0.1169
R_1, $wR2$ (all data)	0.0753, 0.1293
Largest residual peak, hole $e^-/\text{Å}^3$	1.668, -2.626

Sr$_5$As$_4$ crystallizes in the orthorhombic space group *Cmce* with $a = 16.107(2)$,
$b = 8.133(3)$, $c = 8.1629(18)$ and is isotypic to Eu$_5$As$_4$[148]. The structure can

be refined with $R_1 = 0.0479$. Crystallographic data and an overview of distances and angles are given in table A.5 and A.6.

Figure A.2(a) shows the unit cell of Sr_5As_4 (anisotropic thermal displacement parameters with 90 % probability are shown) and figures A.2(b)-(d) illustrate the coordination sheres of the atoms. Two independent atomic positions exist each for strontium and arsenic. The structure can be described by two alternating layers or structural motivs, one planar (layer A, containing Sr1 and As2) and one buckled (layer B, containing As1 and Sr2). To gain a better overview, only the Sr-As bonds within these structural motivs are depicted in Figure A.2(a). One of the most intesting features of the structure is certainly the occurence of As-As dumbbells with d(As-As) = 257 pm. As figure A.2(b) (top) shows, the As1 atoms forming these dumbbells are each coordinated by nine strontium atoms plus one arsenic atom, with six strontium atoms forming a trigonal prism capped by two strontium and the other As atom of the dumbbell. A similar coordination sphere for As is found in Sr_4As_3[149], where [As−As]$^{4-}$ dumbbells occupy the centers of pairs of trigonal prisms with common square faces. [As−As]$^{4-}$ dumbbells with d(As-As) = 252 and 257 pm are also found in Sr_2As_2[150]. The first of the strontium atoms, Sr2, is 14- fold coordinated by six octahedrally (slightly distorted) arranged As atoms plus eight Sr1 atoms capping the faces. The coordination of the second Sr atom, Sr1, is 10- fold, an irregular polyhedron consisting of four strontium atoms arranged more or less tetrahedrally and six arsenic atoms is found, where the distances to the As atoms vary from ~ 311 to ~ 348 pm and the distances to the Sr atoms from ~ 362 to ~ 387 pm. Due to the As-As dumbbells, Sr_5As_4 can be described as a Zintl phase with Sr^{2+} cations and the anions As^{3-} and As_2^{4-}. In agreement with this concept is the structure of the compound $Na_2Sr_3As_4$[151], where two Sr atoms are exchanged by sodium. Because of the introduction of alkali metal, all arsenic atoms in this compound form dumbbells, wich leads to a distortion and shift of layer A relative to layer B.

Table A.6.: Atomic parameters of Sr$_5$As$_4$

Atomic parameters:					
		x	y	z	U_{eq}
Sr1	16g	0.14637(6)	0.33139(12)	0.16343(13)	0.0224(3)
Sr2	4a	0	0	0	0.0205(4)
As1	8f	0	0.1115(2)	0.3885(2)	0.0233(4)
As2	8d	0.19693(9)	0	0	0.0198(3)

Interatomic distances (pm):

Sr1	(CN = 10)		Sr2	(CN = 14)	
	As1	328.79(19)		- 2 x As1	328.8(2)
	As1	330.57(19)		- 2 x As1	329.83(19)
	As1	348.3(2)		- 2 x As2	317.19(15)
	As2	311.58(16)		- 4 x Sr1	382.13(16)
	As2	316.71(17)		- 4 x Sr1	387.12(16)
	As2	317.68(14)			
	Sr1	362.5(2)			
	Sr1	382.6(2)			
	Sr2	382.13(16)			
	Sr2	387.12(16)			
As1	(CN = 9)		As2	(CN = 7)	
	- 2 x Sr1	328.79(19)		- 1 x Sr1	311.58(16)
	- 2 x Sr1	330.57(19)		- 2 x Sr1	316.71(17)
	- 2 x Sr1	348.3(2)		- 2 x Sr1	317.68(14)
	- Sr2	328.8(2)		- 2 x Sr2	317.19(15)
	- Sr2	329.83(19)			
	- As1	257.0(4)			
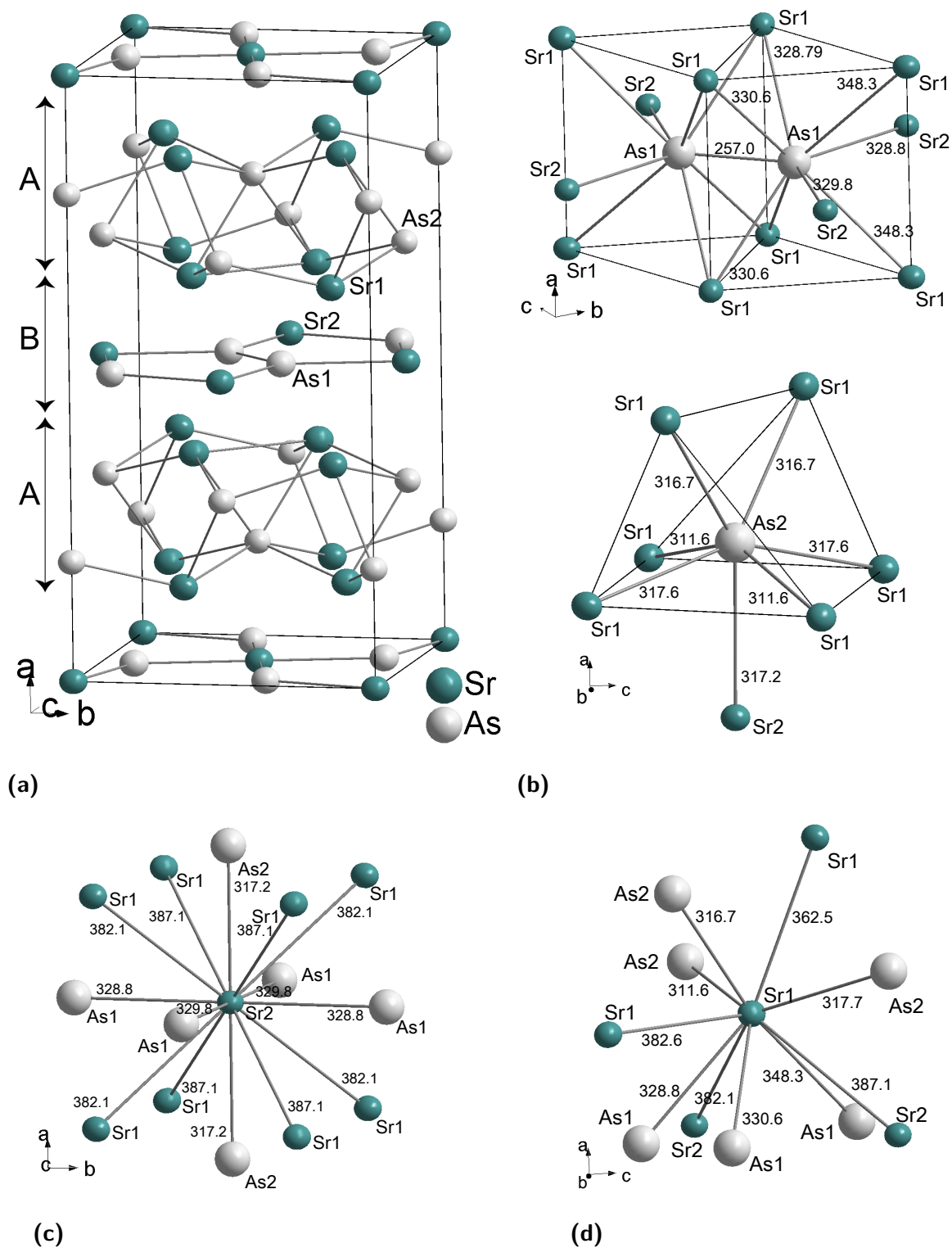
Fig. A.2.: (a) Unit cell of Sr_5As_4, illustration of the coordination of the As atoms (b), Sr2 (c) and Sr1 (d). Bond distances are given in pm.

List of Figures

List of Tables

Bibliography

[1] J. G. Bednorz, K. A. Müller, *Z. Phys. B: Condens. Matter* **1986**, *64* (2), 189–193. 1, 18

[2] M. K. Wu, J. R. Ashburn, C. J. Torng, P. H. Hor, R. L. Meng, L. Gao, Z. J. Huang, Y. Q. Wang, C. W. Chu, *Phys. Rev. Lett.* **1987**, *58*, 908. 1

[3] A. Schilling, M. Cantoni, J. D. Guo, H. R. Ott, *Nature (London, U. K.)* **1993**, *363*, 56. 1

[4] Y. Kamihara, H. Hiramatsu, M. Hirano, R. Kawamura, H. Yanagi, T. Kamiya, H. Hosono, *J. Am. Chem. Soc.* **2006**, *128* (31), 10012–10013. 2

[5] Y. Kamihara, T. Watanabe, M. Hirano, H. Hosono, *J. Am. Chem. Soc.* **2008**, *130*, 3296. 2, 18

[6] C. d. l. Cruz, Q. Huang, J. W. Lynn, J. Li, W. R. II, J. L. Zarestky, H. A. Mook, G. F. Chen, J. L. Luo, N. L. Wang, P. Dai, *Nature (London, U. K.)* **2008**, *453*, 899.

[7] T. Nomura, S. W. Kim, Y. Kamihara, M. Hirano, P. V. Sushko, K. Kato, M. Takata, A. L. Shluger, H.Hosono, *Supercond. Sci. Technol.* **2008**, *21*, 125028. 2

[8] M. Rotter, M. Tegel, I. Schellenberg, W. Hermes, R. Pöttgen, D. Johrendt, *Phys. Rev. B: Condens. Matter Mater. Phys.* **2008**, *78*, 020503(R). 2, 18, 86, 88, 114

[9] M. Rotter, M. Tegel, D. Johrendt, *Phys. Rev. Lett.* **2008**, *101*, 107006. 2, 18, 71, 81

[10] M. Pfisterer, G. Nagorsen, *Z. Naturforsch. B: J. Chem. Sci.* **1980**, *35*, 703. 2, 3, 18

[11] Q. Huang, Y. Qiu, W. Bao, M. A. Green, J. W. Lynn, Y. C. Gasparovic, T. Wu, G. Wu, X. H. Chen, *Phys. Rev. Lett.* **2008**, *101*, 257003. 3

[12] M. Rotter, M. Pangerl, M. Tegel, D. Johrendt, *Angew. Chem.* **2008**, *120*, 8067; Angew. Chem. Int. Ed., 2008, 47, 7949. 3, 5, 18, 56, 66, 67, 81, 82, 85, 92, 97, 101, 103, 141, 145, 146, 147

[13] G. Wu, H. Chen, T. Wu, Y. L. Xie, Y. J. Yan, R. H. Liu, X. F. Wang, J. J. Ying, X. H. Chen, *J. Phys.: Condens. Matter* **2008**, *20*, 422201. 3

[14] N. Ni, S. L. Bud'ko, A. Kreyssig, S. Nandi, G. E. Rustan, A. I. Goldman, S. Gupta, J. D. Corbett, A. Kracher, P. C. Canfield, *Phys. Rev. B: Condens. Matter Mater. Phys.* **2008**, *78*, 014507. 3

[15] Z. Bukowski, S. Weyeneth, R. Puzniak, P. Moll, S. Katrych, N. D. Zhigadlo, J. Karpinski, H. Keller, B. Batlogg, *Phys. Rev. B: Condens. Matter Mater. Phys.* **2009**, *79*(10), 104521. 3

[16] J. Karpinski, N. D. Zhigadlo, S. Katrych, Z. Bukowski, P. Moll, S. Weyeneth, H. Keller, R. Puzniak, M. Tortello, D. Daghero, R. Gonnelli, I. Maggio-Aprile, Y. Fasano, O. Fischer, K. Rogacki, B. Batlogg, *Physica C* **2009**, *469*(9-12), 370–380. 3

[17] R. Cortes-Gil, D. R. Parker, M. J. Pitcher, J. Hadermann, S. J. Clarke, *Chem. Mater.* **2010**, *22*(14), 4304–4311. 3

[18] A. S. Sefat, D. J. Singh, L. H. VanBebber, Y. Mozharivskyj, M. A. McGuire,

R. Y. Jin, B. C. Sales, V. Keppens, D. Mandrus, *Phys. Rev. B: Condens. Matter Mater. Phys.* **2009**, *79*(22), 224524. 3, 82

[19] M. G. Kim, A. Kreyssig, A. Thaler, D. K. Pratt, W. Tian, J. L. Zarestky, M. A. Green, S. L. Bud'ko, P. C. Canfield, R. J. McQueeney, A. I. Goldman, *Phys. Rev. B: Condens. Matter Mater. Phys.* **2010**, *82*(22), 220503(R). 3

[20] A. S. Sefat, R. Y. Jin, M. A. McGuire, B. C. Sales, D. J. Singh, D. Mandrus, *Phys. Rev. Lett.* **2008**, *101*, 117004. 3, 81, 86

[21] N. Ni, A. Thaler, A. Kracher, J. Q. Yan, S. L. Bud'ko, P. C. Canfield, *Phys. Rev. B: Condens. Matter Mater. Phys.* **2009**, *80*(2), 024511. 3, 4, 101

[22] X. F. Wang, T. Wu, G. Wu, H. Chen, Y. L. Xie, J. J. Ying, Y. J. Yan, R. H. Liu, X. H. Chen, *Phys. Rev. Lett.* **2009**, *102*, 117005.

[23] S. L. Li, C. Cruz, Q. Huang, G. F. Chen, T. L. Xia, J. L. Luo, N. L. Wang, P. Dai, *Phys. Rev. B: Condens. Matter Mater. Phys.* **2009**, *80*, 020504.

[24] S. R. Saha, T. Drye, K. Kirshenbaum, N. P. Butch, P. Y. Zavalij, J. Paglione, *J. Phys.: Condens. Matter* **2010**, *22*(7), 072204. 4, 9, 141

[25] P. C. Canfield, S. L. Bud'ko, in *Annual Review of Condensed Matter Physics, Vol 1*, Bd. 1 von *Annual Review of Condensed Matter Physics*, (Herausgegeben von J. S. Langer), Annual Reviews, Palo Alto, **2010**, S. 27–50. 4, 5, 141

[26] S. Jiang, H. Xing, G. Xuan, C. Wanng, Z. Ren, C. Feng, J. Dai, Z. Xu, G. Cao, *J. Phys.: Condens Matter* **2009**, *21*, 382203. 4, 5, 115, 117, 141, 147

[27] S. Sharma, A. Bharathi, S. Chandra, R. Reddy, S. Paulraj, A. T. Satya, V. S. Sastry, A. Gupta, C. S. Sundar, *Phys. Rev. B: Condens. Matter Mater. Phys.* **2010**, *81*, 174512. 4

[28] M. Rotter, C. Hieke, D. Johrendt, *Phys. Rev. B: Condens. Matter Mater. Phys.* **2010**, *82*, 014513. 4, 6, 106, 110, 118, 120, 148

[29] S. Nandi, M. G. Kim, A. Kreyssig, R. M. Fernandes, D. K. Pratt, A. Thaler, N. Ni, S. L. Bud'ko, P. C. Canfield, J. Schmalian, R. J. McQueeney, A. I. Goldman, *Phys. Rev. Lett.* **2009**, *104*, 057006. 5, 6, 141

[30] D. K. Pratt, W. Tian, A. Kreyssig, J. L. Zarestky, S. Nandi, N. Ni, S. L. Bud'ko, P. C. Canfield, A. I. Goldman, R. J. McQueeney, *Phys. Rev. Lett.* **2009**, *103*(8), 087001. 6

[31] A. Kreyssig, M. G. Kim, S. Nandi, D. K. Pratt, W. Tian, J. L. Zarestky, N. Ni, A. Thaler, S. L. Bud'ko, P. C. Canfield, R. J. McQueeney, A. I. Goldman, *Phys. Rev. B: Condens. Matter Mater. Phys.* **2010**, *81*(13), 134512. 6

[32] E. Wiesenmayer, H. Luetkens, G. Pascua, R. Khasanov, A. Amato, H. Potts, B. Banusch, H.-H. Klauss, D. Johrendt, *Phys. Rev. Lett.* **2011**, *107*(23), 237001. 6, 61

[33] D. R. Parker, M. J. Pitcher, P. J. Baker, I. Franke, T. Lancaster, S. J. Blundell, S. J. Clarke, *Chem. Commun. (Cambridge, U. K.)* **2009**, 2189. 7

[34] I. Todorov, D. Y. Chung, H. Claus, C. D. Malliakas, A. P. Douvalis, T. Bakas, J. Q. He, V. P. Dravid, M. G. Kanatzidis, *Chem. Mater.* **2010**, *22*(13), 3916–3925. 7

[35] J. H. Tapp, Z. Tang, B. Lv, K. Sasmal, B. Lorenz, P. C. W. Chu, A. M. Guloy, *Phys. Rev. B: Condens. Matter Mater. Phys.* **2008**, *78*(6), 060505. 7

[36] C. Wang, L. Li, S. Chi, Z. Zhu, Z. Ren, Y. Li, Y. Wang, X. Lin, Y. Luo, S. Jiang, X. Xu, G. Cao, Z. Xu, *Europhys. Lett.* **2008**, *83*, 67006.

[37] M. J. Pitcher, D. R. Parker, P. Adamson, S. J. C. Herkelrath, A. T. Boothroyd, R. M. Ibberson, M. Brunelli, S. J. Clarke, *Chem. Commun. (Cambridge, U. K.)* **2008**, *45*, 5918–5920. 7

[38] F. C. Hsu, J. Y. Luo, K. W. Yeh, T. K. Chen, T. W. Huang, P. M. Wu, Y. C. Lee, Y. L. Huang, Y. Y. Chu, D. C. Yan, M. K. Wu, *Proc. Natl. Acad. Sci. U.S.A.* **2008**, *105*, 14262. 7

[39] K. W. Yeh, T. W. Huang, Y. L. Huang, T. K. Chen, F. C. Hsu, P. M. Wu, Y. C. Lee, Y. Y. Chu, C. L. Chen, J. Y. Luo, D. C. Yan, M. K. Wu, *Europhys. Lett.* **2008**, *84*(3), 37002. 7

[40] X. Zhu, F. Han, G. Mu, B. Zeng, P. Cheng, B. Shen, H.-H. Wen, *Phys. Rev. B: Condens. Matter Mater. Phys.* **2009**, *79*, 024516. 7

[41] P. M. Shirage, K. Kihou, C. H. Lee, H. Kito, H. Eisaki, A. Iyo, *J. Am. Chem. Soc.* **2011**, *133*(25), 9630–9633. 7

[42] J. Guo, L. Sun, C. Zhang, G. Chen, J. He, X. Dong, W. Yi, Y. Li, X. Li, J. Liu, Z. Jiang, X. Wei, Y. Huang, Q. Wu, X. Dai, Z. Zhao, *arXiv:1008.2086v1* **2010**. 7

[43] A. L. Ivanovskii, *Physica C* **2011**, *471*(13-14), 409–427. 7

[44] S. Kakiya, K. Kudo, Y. Nishikubo, K. Oku, E. Nishibori, H. Sawa, T. Yamamoto, T. Nozaka, M. Nohara, *J. Phys. Soc. Jpn.* **2011**, *80*(9), 093704. 7

[45] C. Löhnert, T. Stürzer, M. Tegel, R. Frankovsky, G. Friederichs, D. Johrendt, *Angew. Chem. Int. Ed.* **2011**, *50*(39), 9195–9199.

[46] N. Ni, J. M. Allred, B. C. Chan, R. J. Cava, *Proc. Natl. Acad. Sci. U. S. A.* **2011**, *108*(45), E1019–E1026. 7

[47] G. Xu, H. J. Zhang, X. Dai, Z. Fang, *Europhys. Lett.* **2008**, *84*(6), 67015. 7, 141

[48] D. Johrendt, *J. Mater. Chem.* **2011**, *21*(36), 13726–13736. 7

[49] J. Dong, H. J. Zhang, G. Xu, Z. Li, G. Li, W. Z. Hu, D. Wu, G. F. Chen, X. Dai, J. L. Luo, Z. Fang, N. L. Wang, *Europhys. Lett.* **2008**, *83*(2), 27006. 7

[50] G. Grüner, *Density Waves in Solids*, Perseus Publishing, Cambrigde, MA, **1994**. 8, 17

[51] J. Paglione, R. L. Greene, *Nat. Phys.* **2010**, *6*(9), 645–658. 8, 79

[52] A. D. Christianson, E. A. Goremychkin, R. Osborn, S. Rosenkranz, M. D. Lumsden, C. D. Malliakas, I. S. Todorov, H. Claus, D. Y. Chung, M. G. Kanatzidis, R. I. Bewley, T. Guidi, *Nature* **2008**, *456*(7224), 930–932. 8

[53] H. Ding, P. Richard, K. Nakayama, K. Sugawara, T. Arakane, Y. Sekiba, A. Takayama, S. Souma, T. Sato, T. Takahashi, Z. Wang, X. Dai, Z. Fang, G. F. Chen, J. L. Luo, N. L. Wang, *Europhys. Lett.* **2008**, *83*(4), 47001. 8

[54] I. Mazin, D. J. Singh, M. D. Johannes, M. H. Du, *Phys. Rev. Lett.* **2008**, *101*(5), 057003. 8

[55] K. Kuroki, S. Onari, R. Arita, H. Usui, Y. Tanaka, H. Kontani, H. Aoki, *Phys. Rev. Lett.* **2008**, *101*(8), 087004. 8

[56] D. C. Johnston, *Adv. Phys.* **2010**, *59*(6), 803–1061. 9, 141

[57] M. Tegel, T. Schmid, T. Stürzer, M. Egawa, Y. X. Su, A. Senyshyn, D. Johrendt, *Phys. Rev. B: Condens. Matter Mater. Phys.* **2010**, *82*(14), 140507. 9, 141

[58] H. Ogino, Y. Matsumura, Y. Katsura, K. Ushiyama, S. Horii, K. Kishio, J.-J. Shimoyama, *Supercond. Sci. Technol.* **2009**, *22*, 075008. 9, 141

[59] C. H. Lee, A. Iyo, H. Eisaki, H. Kito, M. T. Fernandez-Diaz, T. Ito, K. Kihou, H. Matsuhata, M. Braden, K. Yamada, *J. Phys. Soc. Jpn.* **2008**, *77*(8), 083704. 8

[60] Y. Mizuguchi, Y. Hara, K. Deguchi, S. Tsuda, T. Yamaguchi, K. Takeda, H. Kotegawa, H. Tou, Y. Takano, *Supercond. Sci. Technol.* **2010**, *23*(5), 054013. 10

[61] K. Kuroki, H. Usui, S. Onari, R. Arita, H. Aoki, *Phys. Rev. B: Condens. Matter Mater. Phys.* **2009**, *79*(22), 224511. 10

[62] M. Tinkham, *Introduction to Superconductivity*, Dover Publications, Mineola, N. Y., **1996**. 17

[63] P. Monceau, N. P. Ong, A. M. Portis, A. Meerschaut, J. Rouxel, *Phys. Rev. Lett.* **1976**, *37*(10), 602–606. 17

[64] J. A. Wilson, F. J. Disalvo, S. Mahajan, *Adv. Phys.* **1975**, *24*(2), 117–201. 17

[65] E. Canadell, M. H. Whangbo, *Chem. Rev. (Washington, DC, U. S.)* **1991**, *91*(5), 965–1034. 17

[66] M. D. Johannes, I. I. Mazin, *Phys. Rev. B: Condens. Matter Mater. Phys.* **2008**, *77*(16), 165135. 18

[67] D. S. Inosov, V. B. Zabolotnyy, D. V. Evtushinsky, A. A. Kordyuk, B. Buchner, R. Follath, H. Berger, S. V. Borisenko, *New J. Phys.* **2008**, *10*, 12507. 18

[68] P. Quebe, L. J. Terbuchte, W. Jeitschko, *J. Alloys Compd.* **2000**, *302*(1-2), 70–74. 18

[69] C. de la Cruz, Q. Huang, J. W. Lynn, J. Y. Li, W. Ratcliff, J. L. Zarestky, H. A. Mook, G. F. Chen, J. L. Luo, N. L. Wang, P. C. Dai, *Nature* **2008**, *453*(7197), 899–902.   18

[70] I. I. Mazin, D. J. Singh, M. D. Johannes, M. H. Du, *Phys. Rev. Lett.* **2008**, *101*, 057003.   18

[71] A. Hellmann, A. Loehken, A. Wurth, A. Mewis, *Z. Naturforsch., B: Chem. Sci.* **2007**, *62*(2), 155–161.   18, 29, 33, 39

[72] M. Tegel, M. Rotter, V. Weiss, F. Schappacher, R. Pöttgen, D. Johrendt, *J. Phys.: Condens. Matter* **2008**, *20*, 452201.   18

[73] I. R. Shein, A. L. Ivanovskii, *Solid State Commun.* **2009**, *149*(41-42), 1860–1865.   18

[74] A. Coelho, TOPAS-Academic, **2007**, 4.1.   19, 40, 66, 73, 111, 132

[75] G. M. Sheldrick, *Acta Crystallogr., Sect. A: Found. Crystallogr.* **2008**, *64*, 112.   20, 55

[76] L. J. Farrugia, *J. Appl. Crystallogr.* **1999**, *32*, 837–838.   20, 55

[77] V. Petricek, M. Dusek, L. Palatinus, Jana2006, 1/07/2011.   20, 40

[78] R. Dronskowski, P. E. Blöchl, *J. Phys. Chem.* **1993**, *97*(33), 8617–24.   20, 34

[79] A. M. M. Schreurs, mergehklf5, Utrecht University, The Netherlands, **2003**.   21

[80] D. Johrendt, C. Felser, O. Jepsen, O. K. Andersen, A. Mewis, J. Rouxel, *J. Solid State Chem.* **1997**, *130*, 254.   35

[81] R. Madar, P. Chaudouet, J. P. Senateur, S. Zemni, D. Tranqui, *J. Less-Common Met.* **1987**, *133*(2), 303–311.   39

[82] Y. Singh, Y. Lee, S. Nandi, A. Kreyssig, A. Ellern, S. Das, R. Nath, B. N. Harmon, A. I. Goldman, D. C. Johnston, *Phys. Rev. B: Condens. Matter Mater. Phys.* **2008**, *78*(10), 104512. 39

[83] A. Imre, A. Hellmann, G. Wenski, J. Grap, D. Johrendt, A. Mewis, *Z. Anorg. Allg. Chem.* **2007**, *633*(11-12), 2037–2045. 39

[84] A. Wurth, V. Keimes, D. Johrendt, A. Mewis, *Z. Anorg. Allg. Chem.* **2001**, *627*(9), 2183–2190. 40

[85] A. Wurth, A. Mewis, *Z. Anorg. Allg. Chem.* **1999**, *625*(3), 449–452. 40

[86] S. van Smaalen, *Incommensurate Crystallography*, Oxford Science Publications, **2007**, S. 123. 50

[87] K. Gesi, *Ferroelectrics* **1985**, *64*(1-3), 413–422. 50

[88] A. G. Slivka, V. M. Kedyulich, E. I. Gerzanich, *Ferroelectrics* **2005**, *317*, 281–285. 50

[89] M. A. Tanatar, A. Kreyssig, S. Nandi, N. Ni, S. L. Bud'ko, P. C. Canfield, A. I. Goldman, R. Prozorov, *Phys. Rev. B: Condens. Matter Mater. Phys.* **2009**, *79*(18), 180508. 53, 59, 63, 125

[90] C. R. Rotundu, W. Tian, K. C. Rule, T. R. Forrest, J. Zhao, J. L. Zarestky, R. J. Birgeneau, *arXiv:1111.3329* **2011**. 53

[91] SMART, version 5.625, Bruker AXS, Madison, USA, **1997**. 55

[92] SAINT+, version 7.34A, Bruker AXS, Madison, USA, **1997**. 55

[93] SADABS, version 2.03, Bruker, AXS, Madison, USA, **1999**. 55

[94] XPREP, version 6.12, Siemens Analytical X-ray Instruments Inc., Madison, USA, **1996**. 55

[95] J. Wright, ImageD11, version 1.0, www.sourceforge.net/apps/trac/fable/wiki, **2005**. 55

[96] C. Ma, H. X. Yang, H. F. Tian, H. L. Shi, J. B. Lu, Z. W. Wang, L. J. Zeng, G. F. Chen, N. L. Wang, J. Q. Li, *Phys. Rev. B: Condens. Matter Mater. Phys.* **2009**, *79*(6), 060506. 59

[97] H. Schmid, E. Burkhardt, E. Walker, W. Brixel, M. Clin, J. P. Rivera, J. L. Jorda, M. Francois, K. Yvon, *Z. Phys. B: Condens. Matter* **1988**, *72*(3), 305–322. 59

[98] M. Rotter, M. Tegel, I. Schellenberg, F. M. Schappacher, R. Pöttgen, J. Deisenhofer, A. Günther, F. Schrettle, A. Loidl, D. Johrendt, *New J. Phys.* **2009**, *11*, 025014. 59, 61, 64, 98, 101, 125, 129, 146

[99] L. Malavasi, G. A. Artioli, H. Kim, B. Maroni, B. Joseph, Y. Ren, T. Proffen, S. J. L. Billinge, *J. Phys.: Condens. Matter* **2011**, *23*(27), 272201. 65

[100] D. Louca, K. Horigane, A. Llobet, R. Arita, S. Ji, N. Katayama, S. Konbu, K. Nakamura, T. Y. Koo, P. Tong, K. Yamada, *Phys. Rev. B: Condens. Matter Mater. Phys.* **2010**, *81*(13), 134524. 66

[101] M. Tegel, C. Löhnert, D. Johrendt, *Solid State Commun.* **2010**, *150*(9-10), 383–385. 66

[102] T. Egami, S. J. L. Billinge, *Underneath the Bragg Peaks: Structural Analysis of Complex Materials*, Bd. 16 von *Pergamon Materials Series*, Pergamon, Oxford, **2003**. 66

[103] C. L. Farrow, P. Juhas, J. W. Liu, D. Bryndin, E. S. Bozin, J. Bloch, T. Proffen, S. J. L. Billinge, *Journal of Physics-Condensed Matter* **2007**, *19*(33), 335219. 66

[104] B. Joseph, V. Zinth, M. Brunelli, B. Maroni, D. Johrendt, L. Malavasi, *Journal of Physics-Condensed Matter* **2011**, *23*(11), 112202. 68, 144

[105] S. Rosza, H. U. Schuster, *Z. Naturforsch. B: J. Chem. Sci.* **1981**, *36*, 1668. 71, 72

[106] K. Hashimoto, A. Serafin, S. Tonegawa, R. Katsumata, R. Okazaki, T. Saito, H. Fukazawa, Y. Kohori, K. Kihou, C. H. Lee, A. Iyo, H. Eisaki, H. Ikeda, Y. Matsuda, A. Carrington, T. Shibauchi, *Phys. Rev. B: Condens. Matter Mater. Phys.* **2010**, *82*(1), 014526. 71, 110

[107] J. K. Dong, S. Y. Zhou, T. Y. Guan, H. Zhang, Y. F. Dai, X. Qiu, X. F. Wang, Y. He, X. H. Chen, S. Y. Li, *Phys. Rev. Lett.* **2010**, *104*(8), 087005. 71

[108] S. W. Zhang, L. Ma, Y. D. Hou, J. Zhang, T. L. Xia, G. F. Chen, J. P. Hu, G. M. Luke, W. Yu, *Phys. Rev. B: Condens. Matter Mater. Phys.* **2010**, *81*, 012503. 71, 82, 145

[109] C. H. Lee, K. Kihou, H. Kawano-Furukawa, T. Saito, A. Iyo, H. Eisaki, H. Fukazawa, Y. Kohori, K. Suzuki, H. Usui, K. Kuroki, K. Yamada, *Phys. Rev. Lett.* **2011**, *106*(6), 067003. 71, 79

[110] D. J. Singh, *Phys. Rev. B: Condens. Matter Mater. Phys.* **2009**, *79*(17), 174520. 71, 72, 75, 79, 106, 127, 144

[111] T. Terashima, M. Kimata, H. Satsukawa, A. Harada, K. Hazama, S. Uji, H. Harima, G. F. Chen, J. L. Luo, N. L. Wang, *J. Phys. Soc. Jpn.* **2009**, *78*(6), 063702. 75

[112] I. Mazin, *Nature* **2010**, *464*(7286), 183–186. 79

[113] M. D. Lumsden, A. D. Christianson, *J. Phys.: Condens. Matter* **2010**, *22*(20), 203203. 79

[114] H. Wadati, I. Elfimov, G. A. Sawatzky, *Phys. Rev. Lett.* **2010**, *105*(15), 157004. 82

[115] M. Neupane, P. Richard, Y. M. Xu, K. Nakayama, T. Sato, T. Takahashi, A. V. Federov, G. Xu, X. Dai, Z. Fang, Z. Wang, G. F. Chen, N. L. Wang, H. H. Wen, H. Ding, *Phys. Rev. B: Condens. Matter Mater. Phys.* **2011**, *83*(9), 094522. 82, 92

[116] Y. Muraba, S. Matsuishi, S.-W. Kim, T. Atou, O. Fukunaga, H. Hosono, *arXiv:1005.0528v2* **2010**. 82

[117] S. Drotziger, P. Schweiss, K. Grube, T. Wolf, P. Adelmann, C. Meingast, H. von Lohneysen, *J. Phys. Soc. Jpn.* **2010**, *79*(12), 124705. 85, 117, 145

[118] A. Jesche, N. Caroca-Canales, H. Rosner, H. Borrmann, A. Ormeci, D. Kasinathan, H. H. Klauss, H. Luetkens, R. Khasanov, A. Amato, A. Hoser, K. Kaneko, C. Krellner, C. Geibel, *Phys. Rev. B: Condens. Matter Mater. Phys.* **2008**, *78*(18), 180504. 88

[119] S. Suzuki, K. Ohgushi, Y. Kiuchi, Y. Ueda, *Phys. Rev. B: Condens. Matter Mater. Phys.* **2010**, *82*(18), 184510. 89, 95, 101, 102, 103, 106, 107, 127, 147

[120] R. Cortes-Gil, D. R. Parker, M. J. Pitcher, J. Hadermann, S. J. Clarke, *Chem. Mater.* **2010**, *22*, 4304. 92

[121] N. Ni, M. E. Tillman, J. Q. Yan, A. Kracher, S. T. Hannahs, S. L. Bud'ko, P. C. Canfield, *Phys. Rev. B: Condens. Matter Mater. Phys.* **2008**, *78*(21), 214515. 103, 115, 117, 147

[122] C. R. Rotundu, R. J. Birgeneau, *Phys. Rev. B: Condens. Matter Mater. Phys.* **2011**, *84*(9), 092501. 103, 113

162

[123] F. Rullier-Albenque, D. Colson, A. Forget, P. Thuery, S. Poissonnet, *Phys. Rev. B: Condens. Matter Mater. Phys.* **2010**, *81*(22), 224503. 104, 105, 147

[124] R. S. Dhaka, C. Liu, R. M. Fernandes, R. Jiang, C. P. Strehlow, T. Kondo, A. Thaler, J. Schmalian, S. L. Bud'ko, P. C. Canfield, A. Kaminski, *arXiv:1108.0711v2* **2011**. 104, 105

[125] K. Park, D. Louca, A. Llobet, J. Q. Yan, *Phys. Rev. B: Condens. Matter Mater. Phys.* **2011**, *84*(2), 024512. 106, 107, 126, 127

[126] M. G. Vavilov, A. V. Chubukov, *arXiv:1110.0972v2* **2011**. 106, 107, 127

[127] F. Ning, K. Ahilan, T. Imai, A. S. Sefat, R. Jin, M. A. McGuire, B. C. Sales, D. Mandrus, *J. Phys. Soc. Jpn.* **2008**, *77*(10), 103705. 106

[128] Y. Zhang, Z. R. Ye, Q. Q. Ge, F. Chen, J. Jiang, M. Xu, B. P. Xie, D. L. Feng, *arXiv:1109.0229v1* **2011**. 110

[129] Y. Nakai, T. Iye, S. Kitagawa, K. Ishida, S. Kasahara, T. Shibauchi, Y. Matsuda, T. Terashima, *Phys. Rev. B: Condens. Matter Mater. Phys.* **2010**, *81*(2), 020503. 110

[130] M. Martin, Dissertation, Ludwig-Maximilians-Universität, **2010**. 111, 112, 118, 147

[131] K. Ahilan, J. Balasubramaniam, F. L. Ning, T. Imai, A. S. Sefat, R. Jin, M. A. McGguire, B. C. Sales, D. Mandrus, *J. Phys.: Condens. Matter* **2008**, *20*(47), 472201. 113, 114, 117

[132] Z. R. Ye, Y. Zhang, M. Ge, Q. Q. Xu, F. Chen, J. Juan, B. P. Xie, J. P. Hu, D. L. Feng, *arXiv:1105.5242v1* **2011**. 116

[133] V. Zinth, T. Dellmann, H. H. Klauss, D. Johrendt, *Angew. Chem. Int. Ed.* **2011**, *50*(34), 7919–7923. 116

[134] E. Colombier, M. S. Torikachvili, N. Ni, A. Thaler, S. L. Bud'ko, P. C. Canfield, *Supercond. Sci. Technol.* **2010**, *23*(5), 054003. 117, 119, 148

[135] Y. Nakashima, H. Yui, T. Sasagawa, *Physica C* **2010**, *470*(20), 1063–1065. 117

[136] L. E. Klintberg, S. K. Goh, S. Kasahara, Y. Nakai, K. Ishida, M. Sutherland, T. Shibauchi, Y. Matsuda, T. Terashima, *J. Phys. Soc. Jpn.* **2010**, *79*(12), 123706. 117

[137] J. E. Jørgensen, T. C. Hansen, *Eur. Phys. J. B* **2010**, *78*(4), 411–415. 118, 120, 148

[138] E. Colombier, S. L. Bud'ko, N. Ni, P. C. Canfield, *Phys. Rev. B: Condens. Matter Mater. Phys.* **2009**, *79*(22), 224518. 119, 148

[139] R. Mittal, S. K. Mishra, S. L. Chaplot, S. V. Ovsyannikov, E. Greenberg, D. M. Trots, L. Dubrovinsky, Y. Su, T. Brueckel, S. Matsuishi, H. Hosono, G. Garbarino, *Phys. Rev. B: Condens. Matter Mater. Phys.* **2011**, *83*(5), 054503. 118, 120, 148

[140] M. D. Johannes, I. Mazin, D. S. Parker, *Physical Review B* **2010**, *82*(2), 024527. 118, 129

[141] H. Göbel, L. Klein, G. Müller-Vogt, R. Orlich, *Physics Letters A* **1972**, *A 41*(5), 409–&. 132, 133, 148

[142] K. C. Rule, M. J. Lewis, H. A. Dabkowska, D. R. Taylor, B. D. Gaulin, *Phys. Rev. B: Condens. Matter Mater. Phys.* **2008**, *77*(13), 134116.

[143] W. Schäfer, G. Will, G. Müller-Vogt, *Acta Crystallographica Section B-Structural Science* **1979**, *35*(MAR), 588–592. 132

[144] F. Hulliger, O. Vogt, *Solid State Commun.* **1970**, *8*(10), 771–&. 136

[145] C. Hadenfeldt, *Z. Anorg. Allg. Chem.* **1977**, *436* (DEC), 113–121.

[146] B. Li, A. V. Mudring, J. D. Corbett, *Inorg. Chem.* **2003**, *42* (21), 6940–6945.   136

[147] N. Wiberg, *Holleman Wiberg, Lehrbuch der Anorganischen Chemie*, de Gruyter, **2007**.   136

[148] Y. Wang, L. D. Calvert, E. J. Gabe, J. B. Taylor, *Acta Crystallogr., Sect. B: Struct. Sci.* **1978**, *34* (JUN), 1962–1965.   137

[149] M. Somer, W. Carrillocabrera, K. Peters, H. G. von Schnering, *Z. Kristallogr.* **1995**, *210* (11), 876–876.   138

[150] J. Getzschmann, P. Böttcher, *Z. Kristallogr.* **1996**, *211* (2), 90–95.   138

[151] W. Hönle, J. H. Lin, M. Hartweg, H. G. von Schnering, *J. Solid State Chem.* **1992**, *97* (1), 1–9.   138

Publications and conference contributions

Major results of this thesis were published or are going to be published in scientific journals. These publications were included in this thesis with some changes and additional information to place them into context. A list of publications, talks and poster presentations is given below. Publications beyond this work are marked with an asterisk.

Publications

Structural phase transitions in SrRh$_2$As$_2$

V. Zinth, V. Petricek, M. Dusek, D. Johrendt

Phys. Rev. B: Cond. Matter Mater. **2012**, *85* (1), 014109. (chapter 3)

Recovery of a Parentlike State in Ba$_{1-x}$K$_x$Fe$_{1.86}$Co$_{0.14}$As$_2$

V. Zinth, T. Dellmann, H.-H. Klauss, D. Johrendt

Angew. Chem. Int. Ed. **2011**, *50* (34), 7919-7923. (chapter 8)

Local structural studies of Ba$_{1-x}$K$_x$Fe$_2$As$_2$ using atomic pair distribution function analysis

B. Joseph, V. Zinth, M. Brunelli, B. Maroni, D. Johrendt, L. Malavasi

J. Phys.: Cond. Matter Mater. **2011**, *23* (11), 112202. (chapter 6)

The interplay of electron doping and chemical pressure in Ba(Fe$_{1-y}$Co$_y$)$_2$(As$_{1-x}$P$_x$)$_2$

V. Zinth, D. Johrendt

EPL **2012**, *98*, 57010. (chapter 10)

CaRh$_2$As$_2$ and Sr$_{1-x}$Ca$_x$Rh$_2$As$_2$

V. Zinth, A. Müller, D. Johrendt

in preparation (chapter 4)

K(Fe$_{1-y}$Co$_y$)$_2$As$_2$

V. Zinth, C. Wilfer, A. Müller, D. Johrendt

in preparation (chapter 7)

Magnetism and structure of charge compensated Ba$_{1-x}$K$_x$(Fe$_{1-y}$Co$_y$)$_2$As$_2$

V. Zinth, T. Goltz, H.-H. Klauss, G. Pascua, H. Luetkens, D. Johrendt

in preparation (chapter 9)

* Structural and magnetic phase transitions of the V$_4$-cluster compound GeV$_4$S$_8$

D. Bichler, V. Zinth, D. Johrendt, O. Heyer, M. K. Forthaus, T. Lorenz, M. M. Abd-Elmeguid

Phys. Rev. B: Cond. Matter Mater. **2008**, *77* (21), 212102.

Conference contributions

V. Zinth, D. Johrendt

Phasenumwandlungen von SrRh$_2$As$_2$ (talk)

Hirschegg Festkörper-Seminar, Hirschegg (Austria), June 2009.

V. Zinth, D. Johrendt

α-SrRh$_2$As$_2$ (talk)

Hirschegg Festkörper-Seminar, Hirschegg (Austria), June 2010.

V. Zinth, D. Johrendt

SrRh$_2$As$_2$ (poster)

Workshop "Properties of high temperature superconductors", München, 13/04 - 16/04/10.

V. Zinth, D. Johrendt

Von Elektronen und Löchern (talk)

Hemdsärmelkolloquium, Dresden, March 2011.